A STUDY OF THE EFFECT OF PHASE SEGREGATION BY SHEAR ON THE RHEOLOGY OF SUSPENSIONS

Lauren Schlatter Fernandes

Dissertação de Mestrado apresentada ao Programa de Pós-graduação em Engenharia Química, COPPE, da Universidade Federal do Rio de Janeiro, como parte dos requisitos necessários à obtenção do título de Mestre em Engenharia Química.

Orientadores: Paulo Laranjeira da Cunha Lage
Gabriel Gonçalves da Silva Ferreira

Rio de Janeiro
Março de 2023

A STUDY OF THE EFFECT OF PHASE SEGREGATION BY SHEAR ON THE RHEOLOGY OF SUSPENSIONS

Lauren Schlatter Fernandes

DISSERTAÇÃO SUBMETIDA AO CORPO DOCENTE DO INSTITUTO ALBERTO LUIZ COIMBRA DE PÓS-GRADUAÇÃO E PESQUISA DE ENGENHARIA DA UNIVERSIDADE FEDERAL DO RIO DE JANEIRO COMO PARTE DOS REQUISITOS NECESSÁRIOS PARA A OBTENÇÃO DO GRAU DE MESTRE EM CIÊNCIAS EM ENGENHARIA QUÍMICA.

Orientadores: Paulo Laranjeira da Cunha Lage
Gabriel Gonçalves da Silva Ferreira

Aprovada por: Prof. Paulo Laranjeira da Cunha Lage
Prof. Gabriel Gonçalves da Silva Ferreira
Prof. Claudia Miriam Scheid Pereira
Prof. Luiz Fernando Lopes Rodrigues Silva

RIO DE JANEIRO, RJ – BRASIL
MARÇO DE 2023

Schlatter Fernandes, Lauren

A study of the effect of phase segregation by shear on the rheology of suspensions/Lauren Schlatter Fernandes. – Rio de Janeiro: UFRJ/COPPE, 2023.

XVIII, 98 p.: il.; 29, 7cm.

Orientadores: Paulo Laranjeira da Cunha Lage
Gabriel Gonçalves da Silva Ferreira

Dissertação (mestrado) – UFRJ/COPPE/Programa de Engenharia Química, 2023.

Referências Bibliográficas: p. 77 – 83.

1. Suspension Rheology. 2. Shear-Induced Migration. 3. OpenFOAM. I. Laranjeira da Cunha Lage, Paulo et al. II. Universidade Federal do Rio de Janeiro, COPPE, Programa de Engenharia Química. III. Título.

Resumo da Dissertação apresentada à COPPE/UFRJ como parte dos requisitos necessários para a obtenção do grau de Mestre em Ciências (M.Sc.)

ESTUDO DO EFEITO DA SEGREGAÇÃO DE FASES POR CISALHAMENTO NA REOLOGIA DE SUSPENSÕES

Lauren Schlatter Fernandes

Março/2023

Orientadores: Paulo Laranjeira da Cunha Lage
Gabriel Gonçalves da Silva Ferreira

Programa: Engenharia Química

Suspensões estão presentes nas mais diversas aplicações industriais, como em processos de extração de óleo e gás, produção de cosméticos, e nas indústrias alimentícia e farmacêutica. Tais misturas podem apresentar comportamentos característicos complexos durante o seu escoamento, e quando sujeitas à aplicação de uma taxa de cisalhamento não uniforme, as partículas migram em direção às zonas de menor taxa de cisalhamento devido à anisotropia da tensão normal das partículas. Esse comportamento, que ocorre tipicamente no regime de Stokes, leva à segregação das fases e dificulta a interpretação de dados experimentais nos processos de caracterização reológica dessas suspensões. O presente trabalho tem o objetivo de estudar e comparar duas das principais formas de modelagem do escoamento de suspensões sob tais condições através da sua implementação e realização de simulações fluidodinâmicas utilizando o *software* OpenFOAM-v7®. Uma versão aperfeiçoada da implementação do conhecido Modelo de Balanço na Suspensão é apresentada, trazendo uma formulação independente do referencial para a anisotropia da tensão normal e uma nova forma de interpolação de *momentum* para prevenir oscilações numéricas. O efeito da segregação de fases na caracterização reológica das suspensões é avaliado utilizando os dados das simulações de forma análoga à realização do procedimento experimental. Dessa forma, mostra-se que a caracterização de suspensões como fluidos não-Newtonianos simples não é capaz de capturar o real comportamento não-Newtoniano da suspensão, com resultados que dependem da geometria utilizada no processo de caracterização, e não conseguem prever de forma acurada o comportamento da mesma suspensão em diferentes condições e geometrias.

Abstract of Dissertation presented to COPPE/UFRJ as a partial fulfillment of the requirements for the degree of Master of Science (M.Sc.)

A STUDY OF THE EFFECT OF PHASE SEGREGATION BY SHEAR ON THE RHEOLOGY OF SUSPENSIONS

Lauren Schlatter Fernandes

March/2023

Advisors: Paulo Laranjeira da Cunha Lage
Gabriel Gonçalves da Silva Ferreira

Department: Chemical Engineering

Suspensions are present in many industrial applications, such as in the oil and gas extraction, cosmetic, pharmaceutical, and food industries. These mixtures may exhibit characteristic and complex flowing behaviors. When subject to non-homogeneous shear, particles tend to migrate towards the regions of lower shear rate of the flow due to the anisotropy on the particles' normal stress. This phenomenon, which is typically observed in the Stokes regime, leads to the segregation of the phases, which complicates the interpretation of experimental data on the rheological characterization of those suspensions. The present work aimed to study and compare two of the main available models for suspension flow accounting for shear-induced migration through their implementation and flow simulation using OpenFOAM-v7®. An improved implementation of the well-known Suspension Balance Model is presented, featuring a frame-independent formulation of the anisotropic particle stress and an improved momentum interpolation scheme that prevents numerical oscillations. The effects of phase segregation on the rheological characterization of suspensions were evaluated using the simulated data as the rheometer experimental data. It was shown that the suspension's characterization as a simple non-Newtonian fluid cannot capture the non-Newtonian behavior observed for the suspension, whose rheometric results depend on the geometry of the rheometer, being unable to predict the suspension behavior on different conditions and geometries.

Contents

List of Figures

List of Tables

List of Symbols

$\mathbf{A}$	Area
$\mathcal{A}$	Diagonal part of the coefficient matrix
a	Particle radius
B	Integration constant
$\mathcal{B}$	Vector of source terms of the semi-discrete momentum conservation equation
b	Mean particle distance
$\mathbf{b}$	Body forces
Ba	Dimensionless ratio between the particle's kinetic energy and the energy dissipated by the fluid squeezing
C	Integration constant
Co	Courant number
d	Particle's diameter
$d(\phi_b)$	Dependence of the shear-induced diffusion on the bulk solid-phase fraction
E	Error estimator
$\mathbf{E}$	Rate of strain tensor
e	Surface roughness
$\hat{\mathbf{e}}$	Coordinate system unit vectors
$\mathbf{f}$	Inter-phase forces

$f(\phi)$	Hindrance function
$\hat{f}(\phi)$	Modified hindrance function
$\mathbf{g}$	Gravitational acceleration
$g(\hat{p})$	Auxiliary function on the estimate of the observed order of accuracy
H	Channel half-width
h	Grid spacing
$\mathbf{I}$	Identity matrix
$\mathbf{J}$	Migration flux
k	Boltzmann constant
K_n	Coefficient of the particles' normal viscosity model
K_s	Coefficient of the particles' shear viscosity model
L	Length
l	Couette gap size
Le	Dimensionless ratio between the repulsive force and the sum of other forces in the opposite direction
M	Auxiliary variable on the dimensional analysis
$\mathcal{M}$	Coefficient matrix of the semi-discrete momentum conservation equation
m	Apparent viscosity of the power-law model
N	Total number of cells on a given computational grid
n	Power coefficient of the power-law model
$\hat{\mathbf{n}}$	Normal unit vector
N_r	Ratio between colloidal and Brownian effects
p	Pressure
$\hat{p}$	Observed order of accuracy
p^*	Pressure to density ratio

Pe	Péclet number
Q	Volumetric flow rate
$\mathbf{Q}$	Anisotropic normal tensor
$\mathbf{r}$	Position vector
$r_{12},\ r_{23}$	Grid refinement ratio
Re	Reynolds number
R_i	Inner Couette cylinder radius
R_o	Outer Couette cylinder radius
S	Surface
$\mathbf{S}$	Effective stress tensor
$s(\varepsilon)$	Auxiliary function on the estimate of the observed order of accuracy
T	Thermodynamic temperature
$\mathbf{T}$	Torque
T_s	Suspension temperature
t	Time
U	Uncertainty estimator
$\mathbf{u}$	Velocity
v	Velocity scale
w	Width

Greek Letters

α	Hindrance function coefficient
β	Drag coefficient of the two-fluid model
Γ	Ratio between the hydrodynamic energy dissipation and the energy barrier
$\dot{\gamma}$	Shear rate
ϵ	Non-local correction coefficient

ε	Generic variable field
ζ	Dimensionless radial coordinate
η	Relative viscosity
Θ	Granular Temperature
κ	Bulk viscosity
λ	Anisotropic tensor coefficients
μ	Dynamic viscosity
ν	Kinematic viscosity
ρ	Density
$\boldsymbol{\sigma}$	Stress tensor
τ	Dimensionless time
$\boldsymbol{\tau}$	Deviatoric stress tensor
Φ	Mean energy barrier
ϕ	Dispersed-phase volumetric fraction
φ	Volumetric flux
$\boldsymbol{\chi}$	Particle-phase anisotropic normal stress
ω	Inner Couette cylinder angular velocity

Mathematical Operations

$\mathbf{A}^T$	Transpose of matrix $\mathbf{A}$
$tr(\mathbf{A})$	Trace of matrix $\mathbf{A}$
$\check{\varepsilon}$	Dimensionless ε
$\overline{\varepsilon}$	Mean value of ε

Subscripts

0	Reference value
1, 2, 3	Directions of the local coordinate system

b	Bulk value
c	Critical value
cf	Property evaluated at the cell faces
ch	Characteristic property
eff	Effective property
f	Continuous phase property
$formal$	Formal order of accuracy
m	Maximum packing value
$m1,\ m2,\ m3$	Property evaluated on the coarsest, intermediate or finest mesh, respectively
max	Maximum property value
min	Minimum property value
n	Normal
nl	Non-local correction
OR	Limited observed order of accuracy
p	Particle property
$r,\ \theta,\ z$	Directions of the cylindrical coordinate system
s	Suspension property
w	Property evaluated on the wall
$x,\ y,\ z$	Directions of the Cartesian coordinate system

Superscript

(n)	Property evaluated at the current iteration
(o)	Property evaluated at the previous iteration
$+$	Value being approached from greater values
-	Value being approached from smaller values
b	Buoyancy

d	Drag

Abbreviations

CFD	Computational fluid dynamics
cte	Constant
DFM	Diffusive Flux Model
DIC	Diagonal Incomplete Cholesky factorization
DILU	Diagonal ILU factorization
DNS	Direct Numerical Simulation
NMR	Nuclear magnetic resonance
ODR	Orthogonal distance regression
PBiCG	Preconditioned Biconjugate Gradient
PCG	Preconditioned Conjugate Gradient
res	Residual
SBM	Suspension Balance Model
SD	Stokesian Dynamics
TFM	Two-Fluid Model

Chapter 1

Introduction

Suspensions consist of small solid particles suspended on a carrier fluid, which are present in natural processes and industrial systems. The blood flowing in our veins is a suspension, as also are the lava flowing from a volcano and the mud on landslides. Suspensions are widely used in the pharmaceutical (delivery of drugs and DNA molecules to specific cells or tissues using micro-devices, such as micro-needles), cosmetic (toothpaste and cosmetic pastes in general), and civil engineering industries (fresh concrete), and in processes such as ceramic injection molding, bio-refining, water treatment, and many others [4–9]. In food processing, suspensions are created when mixing water and flour, in fermentation processes and in juice (with pulp) processing [7, 10].

Specifically, in the oil and gas industry, suspensions take part in the hydraulic fracturing process when solid proppants are mixed with the fracking fluid in order to prevent the fracture from closing after depressurization of the well [11]. They also appear on oil-dominated flows due to the spontaneous formation of gas hydrates, which becomes especially critical as the solid material can deposit and end up blocking the pipeline [12].

For proper designing and optimization of industrial processes involving suspension flows, it is of extreme importance to be able to accurately describe its behavior. That is not an easy task, since many complex phenomena may take place and the suspension flow can be dominated by different types of inter-particle and inter-phase interactions, depending on the characteristics of the suspension and the flow conditions. Characterization of the suspension itself depends on several factors: the size, roughness, and shape of the particles, their concentration and polydispersity, the presence of colloidal inter-particle forces, and the overall characterization of the carrier fluid, especially its rheological properties and the relative density between phases. The flow conditions may favor one or another mechanism of interaction, with transition limits that depend on the suspension description.

To illustrate the different regimes and phenomena that may take place on suspen-

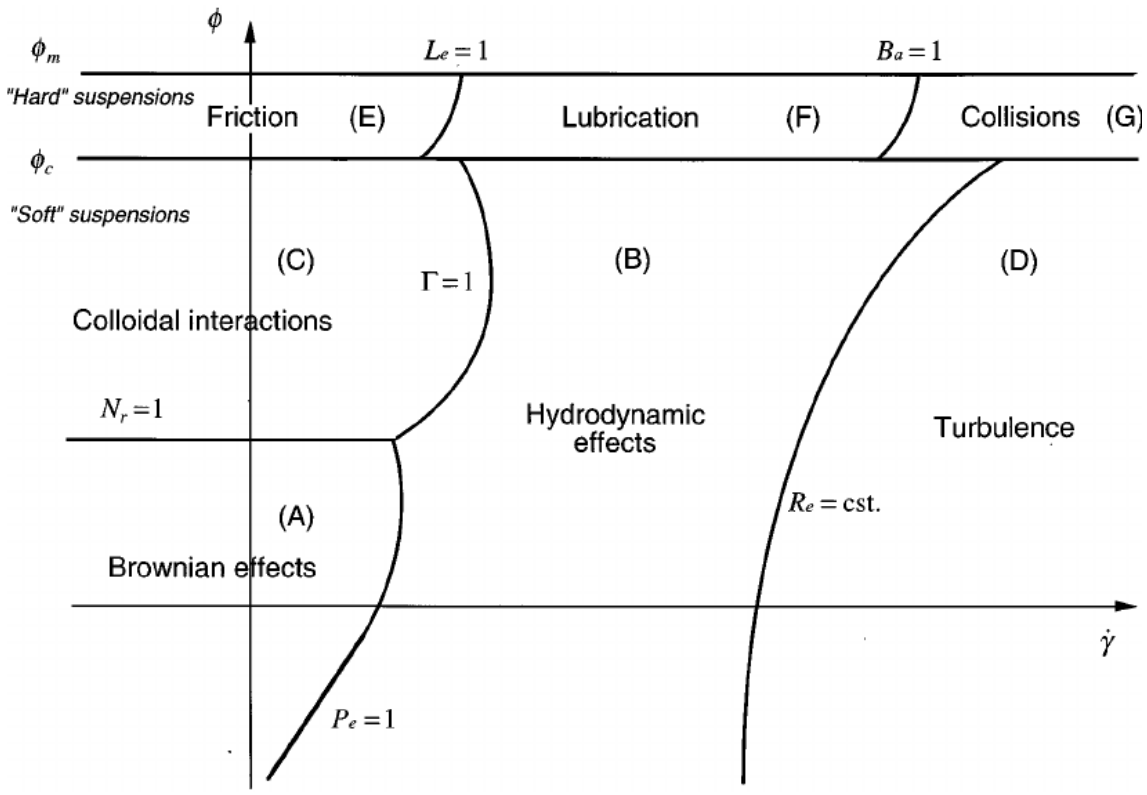

Figure 1.1: Conceptual diagram for classification of the different suspension flow regimes (on a logarithmic scale). Reproduced from COUSSOT and ANCEY [1] with permission.

sion flow, consider the diagram of COUSSOT and ANCEY [1] in Figure 1.1, which relates the main types of dominant interactions in a suspension to the particle concentration (represented by the volumetric phase fraction ϕ) and to the applied shear rate ($\dot{\gamma}$). It is important to emphasize that the lines on this conceptual diagram do not represent exact limits of transition between regimes, but approximate regions. The exact positions of the transition lines depend on a more detailed description of each system under study.

In regime (A), the suspension flow is dominated by Brownian effects. Brownian motion is the random movement of the suspended particles, which is typically most relevant for particles with characteristic sizes smaller than 1 μm [8]. Its predominance in the flow can be inferred by the value of the Péclet number ($Pe = 6\pi\mu_f\dot{\gamma}a^3/kT$, where a is the particle radius, μ_f is the carrier fluid's dynamic viscosity, k is the Boltzmann constant and T the thermodynamic temperature), which represents the ratio between the viscous and Brownian effects [1]. If it is smaller than unity, then, the suspension flow is on the left side of the $Pe = 1$ line of the diagram shown in Figure 1.1. Other colloidal effects can also be taken into account if there are inter-particle and/or surface forces acting on the system, such as the van der Waals and electrostatic forces. As a consequence of these colloidal

forces, each particle has an equilibrium relative position that minimizes its potential energy, associated with an energy barrier that has to be overcome in order to displace the particles from this position. Representing the average energy barrier associated with a mean (in time and space) potential minimum as Φ and the mean particle's thermal energy as kT, the dimensionless number $N_r = \Phi/kT$ is defined to evaluate which effect should prevail. With the increase in the particle concentration, it becomes harder to displace the particles away from their equilibrium position, and as N_r reaches values above 1, the suspension flow migrates from the regime (A) to regime (C), dominated by the colloidal interactions in which, macroscopically, suspensions show apparent yield stresses [1].

As the shear rate increases, so does the viscous force acting on the particles. For suspension flows in regime (A), if the increase in the shear rate leads to $Pe > 1$, they transition to the regime (B), dominated by hydrodynamic effects. Similarly, for suspensions of spherical particles flowing in regime (C) with a mean particle distance of b, the dimensionless number $\Gamma = 3\pi a\mu_s\dot{\gamma}b^2/\Phi$ is introduced to measure the relation between the hydrodynamic energy dissipation and the energy barrier needed to move a particle from its equilibrium position, where μ_s is the suspension's viscosity. As the viscous force increases, the system transitions from the regime (C) to regime (B) at $\Gamma = 1$. With further increase in the suspension velocity (and consequently in the shear rate), the flow may achieve the turbulent regime (D), in which inertial effects are dominant. Even though this transition limit is represented in Figure 1.1 by the main flow's Reynolds number ($Re = \rho_s\dot{\gamma}L_{ch}^2/\mu_s$, where ρ_s is the suspension's density and L_{ch} is a characteristic length of the flow), it is more common to describe it using the particle's Reynolds number $Re_p = \rho_f\dot{\gamma}a^2/\mu_f$ (defined using the fluid's density and viscosity). If $Re_p \ll 1$, the inertial effects can be neglected and the suspension flow in regime (B) is said to be in the Stokes regime [13–16]. Hereinafter, suspension flows are denominated as Brownian if they are in regime (A), and as colloidal if they are in regime (C). For the lower shear rate values in regime (B), for which Re_p is still much smaller than unity, they are taken to be in the Stokes regime.

For highly concentrated suspensions, with concentrations between a critical value and the maximum packing fraction (represented in Figure 1.1 by ϕ_c and ϕ_m, respectively), inter-particle contact interactions play the dominant role in the suspension flow. In the diagram, shown in Figure 1.1, these are referred to as *hard suspensions*, in contrast to those with concentration below ϕ_c, which are called *soft suspensions*. For $\phi > \phi_c$, there are the frictional (E), lubricated (F), and collisional (G) regimes. As the particles in a suspension flowing in regime (B) approach one another, a repulsive force arises due to the thin film of fluid that separates them, in a direction normal to the particles' center. For the particles to collide, the force needed to

drain the fluid between the particles has to be overcome. If no external force is acting on the system, the viscous force in a simple shear flow is not sufficient to overcome this threshold. Hence, particle contact is indirect and called *lubricated*. If concentration increases above the critical value, the flow is controlled by the effects of the lubricated contact, transitioning from the regime (B) to regime (F). For lower values of the shear rate the repulsive force between particles is smaller, which favors direct contact, especially if an additional external force such as gravity is acting on the system. The suspension, then, flows in the frictional regime (E). The transition between the frictional and lubricated regimes is represented by the dimensionless number $Le = \mu_f \dot{\gamma} b / F_n e$ (where e is the particle's surface roughness). It represents the ratio between the repulsive force, which prevents direct contact, and F_n, which is the sum of the viscous and external forces acting in the opposite direction of the aforementioned repulsive force. The $Le = 1$ line in Figure 1.1 marks the transition between regimes (E) and (F): if $Le < 1$, the suspension flows in the frictional regime, and if $Le > 1$, in the lubricated regime. On the other hand, for rapid flows with higher shear rates, the kinetic energy of the particles increases and may be sufficient to cause direct contact. This takes the suspension's flow to the collisional regime (G), with a transition represented in Figure 1.1 by the dimensionless number $Ba = \rho_p \dot{\gamma} a e / \mu_f$ - the ratio between the particle's kinetic energy and the energy dissipated when particles approach one another (ρ_p is the particle's density).

In regime (B), in which inertial effects are negligible, if the suspension is flowing subject to non-homogeneous shear, *shear-induced migration* occurs. This phenomenon causes the particles to migrate towards the region of lower shear rate, leading to segregation of the phases, and so, to non-homogeneous concentration and local change of the apparent viscosity. It is described in detail in the following chapters of this work. The shear-induced migration has been extensively studied, aiming to find a complete model that accurately describes the rheological behavior of the suspensions, because many of the aforementioned industrial applications of suspension flows may occur in this specific regime. This particular phenomenon is, therefore, the focus of this work.

1.1 Objectives

The main objective of this work is to evaluate the effects of phase segregation due to non-homogeneous shear on the rheological characterization of suspensions. Specifically, discussions are restricted to non-Brownian and non-colloidal Stokesian suspensions of monodispersed spherical particles on a Newtonian fluid of matching density (i.e., a neutrally buoyant suspension). The available mathematical models that represent particle migration and their implementations were studied and compared

by performing computational fluid dynamics (CFD) simulations using OpenFOAM-v7® [17] - an open source CFD software written in `C++`. This work shows that simple non-Newtonian models cannot provide an accurate rheological description of these suspensions, leading to difficulties in their experimental characterization.

1.2 Document Structure

A literature review is given in Chapter 2, outlining some of the most historically relevant experimental observations of shear-induced particle migration, as also the main modeling strategies found in the literature and their applications. The methodology is presented in Chapter 3, giving a detailed description of the models used in this work, as well as a conceptual description of the studied cases. The numerical procedure is presented in Chapter 4, with the implementation details, solution algorithm, mesh generation procedure, and the description of the numerical setup used for all performed simulations. Results and conclusions are given, respectively, in Chapters 5 and 6.

Chapter 2

Literature review

2.1 Earlier Experimental Studies

The study of suspension rheology dates back to EINSTEIN [18], who showed that the mixture's viscosity coefficient increases proportionally to the particles' volumetric phase fraction for a dilute suspension of rigid particles. A few years later, in a correction to the previously mentioned work, he presented his famous equation for the suspension's viscosity as a function of the dispersed-phase volumetric fraction [19], which is widely known as Einstein's correction, yielding good results for dilute suspensions of rigid spheres. It is still a reference for the analysis and proposition of new rheological models that must retrieve Einstein's equation when the particles' concentration tends to zero.

As pointed out by GADALA-MARIA and ACRIVOS [20], the earlier attempts to measure the suspension's viscosity showed significant scatter and low reproducibility. By performing experiments of long duration in a Couette cell with neutrally buoyant suspensions of monodispersed, rigid, non-Brownian particles, with a Newtonian carrier fluid, the authors linked the scattered and inconclusive results to an inadequate experimental technique. It was shown that, for systems where non-hydrodynamic contributions can be neglected, the measured torque took long periods of time to achieve the steady state. Thus, most of the results reported so far in the literature considered data from the transient regime to predict the suspension's viscosity. Moreover, the time needed to stabilize the torque was inversely proportional to the applied shear rate.

Another important observation by GADALA-MARIA and ACRIVOS [20] came from the results of shear reversal and oscillatory shear experiments performed in the Couette rheometer. They observed a transient response of the torque signal upon shear reversal, in contrast to what is expected of a Newtonian fluid under the same circumstances. They also obtained non-Newtonian responses to oscillatory

shear, with the deviation from the expected Newtonian behavior increasing as the solid-phase fraction increases. These observations were ascribed to a shear-induced anisotropy in the suspension's particle structure, which had been formerly shown to take place only for suspensions in which non-hydrodynamic effects were present [21].

2.2 Modeling of the Migration

Stokesian Dynamics

A general method for the dynamic simulation of suspension flows was introduced by BOSSIS and BRADY [22], used to predict the anisotropic local particles' structure formed due to their shear-induced migration. Known as Stokesian Dynamics (SD), the proposed method consists of solving Newton's equations of motion for all particles in the system, which interact through hydrodynamic and non-hydrodynamic forces, along with the conservation equations for the continuous phase flow. This strategy provides a highly detailed description of the suspension's local properties, making it possible to study not only the dynamics of particle migration but also a number of other phenomena. Many studies use Stokesian Dynamics to investigate the microstructure formation, the transition between Newtonian and non-Newtonian behavior, and the normal stress anisotropy [23–25]. However, this modeling strategy features a significant limitation: since it solves Newton's equations for every single particle on the system, SD simulations of large-scale complex flows are impracticable.

Diffusive Flux Model

Reproducing the experimental study of GADALA-MARIA and ACRIVOS [20], LEIGHTON and ACRIVOS [2] showed that the slow decrease in the torque signal reported in the former study was due to a shear-induced particle diffusion from regions of high shear rate towards regions of low shear rate. To illustrate the diffusion mechanism as proposed by these authors, consider two particles in adjacent streamlines of the suspension flow. When they move past one another, the particle's collision irreversibly displaces them away from their original streamlines. If there is a variation in the collision frequency across the stream surfaces, particles will migrate in the direction of the lower collision frequency region. Consequently, a net migration flux is established in a direction that is normal to the shearing surface. Additionally, a gradient of the suspension's viscosity across the stream surfaces results in a gradient of resistance to motion, which displaces the particles' post-collisional equilibrium positions towards the direction of lower viscosity when compared to interaction in the absence of a viscosity gradient, as shown in Figure 2.1. Therefore, a diffusion

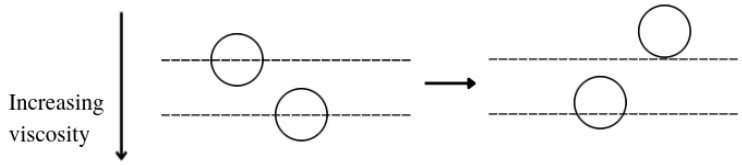

Figure 2.1: Illustration of the collision mechanism proposed by LEIGHTON and ACRIVOS [2].

flux due to the spatial variation of concentration, and consequently, viscosity, also arises. Each diffusive term is described by an expression proportional to a diffusion coefficient (to be determined experimentally) and the proper scaling factors.

A diffusion equation to model the solid-phase fraction profile for the Stokes flow of concentrated suspensions was proposed by LEIGHTON and ACRIVOS [2] and was subsequently improved by PHILLIPS *et al.* [3], who developed a diffusion equation which, solved together with the suspension's equations of motion, provides the evolution of the solid-phase fraction field. On the formulation of PHILLIPS *et al.* [3], the suspension is modeled as an effective Newtonian fluid with properties depending on the local particle-phase fraction, which comes from the solution of the particles' diffusion equation. These authors studied the Couette flow of neutrally buoyant suspensions of non-colloidal and non-Brownian particles with bulk solid-phase fractions of 45%, 50%, and 55%, and for a wide range of applied shear rates (with the angular velocity of the rotating cylinder varying from 17 to 117 rotations per minute). The diffusion coefficients were determined to best fit the experimental data for the most concentrated suspension, and used to predict the concentration profiles for the suspension flows with lower bulk solid-phase fractions, comparing the obtained results with the experimental observations. It was noticed that, as the bulk solid-phase fraction decreases, the predicted profiles close to the rotating cylinder significantly differed from the experimental values, indicating that the diffusion coefficients, formerly considered constants, actually depend on the local solid-phase fraction. According to PHILLIPS *et al.* [3], these discrepancies may be more pronounced in the lower solid-phase fraction regions since the long-range hydrodynamic interactions that have been neglected in the development of the model can also take place and may overcome the considered short-range contributions. In fact, LEIGHTON and ACRIVOS [2] had already stated that the diffusion coefficients for the proposed mechanism are strongly dependent on the solid-phase fraction profile and should only be considered as constants for flows with small variations of the particles' concentration.

The model proposed by PHILLIPS *et al.* [3] is known as the Diffusive Flux Model (DFM) and its main advantage is its simplicity and ease of numerical implementation. It can be easily adapted to account for other sources of particle migration, e.g.,

the effects of Brownian motion and gravity forces. Nevertheless, it is grounded on the assumption that migration occurs in the direction normal to the shearing surface. That is true for the viscosimetric flow on a Couette rheometer and for the flow in a straight channel, but not for the flows in cone-and-plate and torsional parallel-plate rheometers. Therefore, this model cannot be directly extended for general geometries. It is important to emphasize that, as mentioned herein, the suspension is modeled as an effective fluid with properties depending on the solid-phase fraction - an approach called *mixture model*. This is an approximation that holds only for systems with rapid relaxation and small slip velocity between the phases, i.e., when particles reach local equilibrium in a time scale far shorter than the characteristic time scale of the flow [5].

Some recent studies use the Diffusive Flux Model to predict particle migration for viscosimetric flows in simple geometries. KANG and MIRBOD [4] applied the DFM in Direct Numerical Simulation (DNS) of both Couette and channel flows to study the effect of Brownian forces in suspension flows of neutrally buoyant colloidal particles and the resulting shear-thinning behavior. These authors observed that, as the contribution of Brownian forces increases, shear-induced migration from high to low shear rate regions weakens, flattening the solid-phase fraction profiles compared to those obtained for non-Brownian suspensions.

HERNÁNDEZ [26] developed an unsteady continuum model with an adapted constitutive equation based on PHILLIPS *et al.* [3] model to account for shear-induced particle migration and buoyancy effects. The implemented model was used to solve the channel flow of suspensions with both Newtonian and Bingham carrier fluids. Previously, SIQUEIRA and DE SOUZA MENDES [27] also applied the Diffusive Flux Model to simulate the pressure-driven flow of a suspension with an apparent yield-stress carrier fluid. However, their model was restricted to steady-state conditions.

Suspension Balance Model

Shortly after the presentation of the Diffusive Flux Model, a novel modeling approach was introduced by NOTT and BRADY [13], called the Suspension Balance Model (SBM). The key idea of the new model is that, since the particles evolve according to Newton's equations of motion just as molecules, they can be macroscopically described as a continuum phase, in the same way as molecular systems. The main difference relies on the complexity of the interaction forces between the particles that are strongly dependent on their spatial configuration. Then, instead of writing a diffusion equation, transport equations are written for the dispersed phase and they are coupled to the transport equations for the suspension. These equations for the dispersed phase are obtained by averaging the instantaneous local transport

equations, similar to the equating of molecular systems. The detailed step-by-step of the ensemble-averaging procedure used by NOTT and BRADY [13] to formulate their model can be found in the works of DREW and LAHEY [28] and MAZZEI [29].

NOTT and BRADY [13] then proposed a new model for the flow of non-Brownian suspensions of rigid particles dispersed in a Newtonian fluid. They defined the dispersed-phase effective stress tensor that accounts for the presence of non-Newtonian normal stresses and viscously generated (i.e., linear in the shear rate) shear stress with a dependence on the solid-phase fraction through a particle viscosity coefficient. The existence of normal stress anisotropy is acknowledged, as observed experimentally by GADALA-MARIA and ACRIVOS [20] and HOFFMAN [21], but it is neglected under the assumption that it doesn't play a role in the rectilinear flow chosen as the validation case. Thus, their normal stresses are isotropic. They also considered that the normal stresses scale linearly with the shear rate, as does the shear stress, but with a dependence on the solid-phase fraction of unknown functional form. Finally, the suspension's stress tensor needed to close its momentum balance was taken as the sum of the individual phases' stress tensors and so, it is non-Newtonian.

NOTT and BRADY [13] made an important observation concerning the breakdown of the models presented so far when the shear rate vanishes. The diffusion coefficient is taken to be linearly proportional to the shear rate and should vanish in regions where the shear rate is zero. However, the Stokesian Dynamics simulations performed by NOTT and BRADY [13] showed that there is a nonzero particle diffusivity at these regions due to small fluctuations of the particle's velocity on the scale of the particle size. A more tangible consequence of this issue is the observation that, as the shear rate approaches zero at the center line of channel flows, the SBM predicts that the solid-phase fraction should approach maximum packing, which causes a nonphysical cusp in the solid-phase fraction profile [6], which is also in disagreement with experimental observations and SD simulations' results. Thus, a non-local description of the flow is necessary. NOTT and BRADY [13] proposed a non-local formulation based on the introduction of a new field variable, the *suspension temperature*, which represents a scalar measurement of the fluctuations of the particle's mean velocity, similar to the granular temperature from the kinetic theory of granular flows (not to be mistaken with the suspension's thermodynamic temperature). This strategy, however, requires solving an additional transport equation for the suspension temperature. In following works dedicated to improving the suspension balance model, simpler non-local descriptions have been introduced using algebraic expressions instead of adding a new field variable, while still effectively eliminating the model failing at vanishing shear rate regions [6, 14, 30].

Studying the suspension balance model for curvilinear flows of neutrally buoyant non-colloidal particles dispersed in a Newtonian fluid, MORRIS and BOULAY [14] significantly advanced towards a more generic form of the model. Based on previous predictions of normal stress differences by Stokesian Dynamics simulations, MORRIS and BOULAY [14] wrote the normal stresses to be compressive and scale linearly with the shear rate, with a functional dependence on the solid-phase fraction (as described by NOTT and BRADY [13]). Constant parameters were introduced in the normal stress terms, whose values ensure both anisotropy and qualitative agreement with experimental observations. A full description of the functional forms for the dependency of the suspension's shear and normal stresses on the solid-phase fraction was also given by MORRIS and BOULAY [14], considering the previous observations of BRADY and MORRIS [31] on the behavior of normal stresses at the dilution limit. The resulting suspension's viscosity was also shown to respect Einstein's correction [19] at these conditions. Coefficients of the model were fitted to match the experimental data of PHILLIPS *et al.* [3] for the Couette flow with intermediate bulk solid-phase fraction. Then, the model was used to predict the solid-phase fraction distributions for the flow of the more dilute and more concentrated suspensions, providing a good representation of the experimental data. At this point, the reader is reminded of the fact that the DFM predictions of PHILLIPS *et al.* [3] did not show such good agreement with their own experimental data in regions of lower concentration.

In the resulting suspension balance model, shear-induced migration appears naturally, arising from the presence of the non-Newtonian normal stresses. Therefore, it can be predicted by analyzing the model equations, while it had been imposed in the form of an extra phenomenological equation in the diffusive flux model. Here lies the main conceptual contrast between the two modeling approaches: the diffusive flux model treats the suspension as a Newtonian fluid and imposes shear-induced migration by introducing the diffusion equation, while the suspension balance model considers the presence of non-Newtonian normal stresses, which can be mathematically shown to be responsible for the shear-induced migration. Using the formulation of MORRIS and BOULAY [14], the SBM now accurately represents the behavior of several viscosimetric suspension flows. It predicts migration towards the center line for channel flows and towards the stationary cylinder in a Couette rheometer, both in the direction normal to the shearing surface, as does the DFM. For parallel-plate torsional flow, no migration is predicted, as observed experimentally, and for the cone-and-plate flow, particles are correctly predicted to migrate radially outward, away from the cone [14]. Analysis of the SBM equations for viscosimetric flows and how the normal stresses cause the shear-induced migration can be found in the literature [13, 14, 32], and will be partially reproduced in Chapter 3.

Despite the advances in accurately predicting several viscosimetric flows, the formulation of MORRIS and BOULAY [14] still features one significant limitation. Since normal stresses are incorporated in the particles' stress through a diagonal tensor defined in terms of the main directions of the flow, it is a frame-dependent model and cannot be directly applied for flows where the directions of the suspension velocity, its gradient, and vorticity do not coincide with the chosen coordinate system. If one wishes to solve the Couette flow equations on a Cartesian coordinate system, or the flow over a contraction/expansion, e.g., the given formulation of the normal stress is not suitable.

The frame-dependency issue was addressed by MILLER *et al.* [33], who formulated a two-dimensional frame-invariant form of the particles' normal stress tensor based on the local kinematics of the flow. A tension-compression local coordinate system was defined in terms of the eigenvectors of the strain rate tensor and used to map the anisotropic tensor of MORRIS and BOULAY [14] from the original coordinate system to the local one. The magnitudes of the resulting tensor components were weighted by interpolation functions that account for the local kinematic behaviors from pure extensional flow to solid-body rotation. MILLER *et al.* [33] validated this formulation for the channel flow with a sudden contraction and for the flow over a cavity. Despite achieving the goal of developing a frame-invariant model for 2-D flows, their formulation is quite complex and strongly dependent on the local kinematic state [15]. A much more direct way to deal with the frame-dependency of the anisotropic normal stresses was presented by MUNICCHI *et al.* [16], who replaced the unit vectors originally used to define the anisotropic tensor with unit vectors defined using the calculated velocity field.

After MILLER and MORRIS [6], DBOUK *et al.* [34] performed a series of experimental measurements of the normal stress differences on the flow of a non-colloidal and neutrally buoyant suspension. Good agreement was found among their results and several other experimental studies in a variety of viscosimetric flows [35–40]. Comparison with the SBM formulation of MORRIS and BOULAY [14] yielded a good fit for the particles' normal viscosity, which introduces the normal stress dependency on the solid-phase fraction, but the coefficient of the suspension's shear viscosity had to be re-evaluated in order to match the data. All coefficients of the anisotropic tensor, previously considered constants, were found to be slightly dependent on the solid-phase fraction. This experimental work was followed by a computational study [15], in which a formulation of the suspension balance model for monodispersed suspensions of non-Brownian particles on a Newtonian fluid, accounting for buoyancy effects and the frame-invariant formulation of MILLER *et al.* [33], was implemented using OpenFOAM®. The resulting solver was used to predict the suspension flow in three different situations: initially homogeneous suspension

flowing in a straight channel, flow in a Couettte rheometer, and particles' resuspension in a Couette cell starting from a settled suspension. The results present good agreement with the experimental data and model predictions from previous studies.

Additionally, other effects have already been successfully incorporated into the suspension balance model. MORRIS and BRADY [32] specifically studied the effects of buoyancy by adapting the formulation of NOTT and BRADY [13] and validated their modified model against the results of Stokesian Dynamics simulations. The influence of Brownian motion in micro-channel flows of suspensions was studied by GAO *et al.* [41] and FRANK *et al.* [42]. VON PFEIL *et al.* [43] applied the SBM for studying the behavior of electro- and magneto-rheological suspension flows.

Frictional Model

An alternative modeling strategy was introduced by BOYER *et al.* [44] based on a frictional approach derived from the theory of dry granular flows, which describes the behavior of granular materials in the dense regime, neglecting the particles' interaction with interstitial fluid [45, 46]. These authors adapted and extended the existing models for dry granular systems to model the stresses in a suspension of monodispersed particles in a Newtonian fluid with isotropic particles' normal stress. Their model predictions agreed well with the experimental data. The Frictional Rheology Model of BOYER *et al.* [44] was reviewed by LECAMPION and GARAGASH [47] and extended to suspension flows in the jammed state. In this particular case, the confined suspension achieves maximum packing and the particles group into a non-flowing plug inside the channel, with zero velocity, through which the fluid percolates as a porous media.

Multiphase Modeling

The Diffusive, Suspension Balance, and Frictional modeling strategies presented so far are built around the concept of treating the mixture as an effective fluid. They are very useful to study the overall rheological behavior of the suspension. However, as mentioned before, the effective fluid approximation only holds for systems with small slip velocities [5]. The study of shear-induced migration is also of interest in the field of multiphase fluid dynamics, where fluid and particles are treated as two interpenetrating phases, and transport equations are solved for each phase. Consequently, there is no need to limit the model's application to systems of rapid relaxation, and the effects of the migration are more or less relevant for the flow under study depending on the magnitude of other phenomena occurring simultaneously.

Using a rather similar approach to the diffusive flux model in the multiphase framework, TIWARI *et al.* [48] and DRIJER *et al.* [7] introduced the effects of

shear-induced particle migration in the momentum conservation equations of both phases as a driving force. Both studies focused on the application of the proposed models to the simulation of suspension flow in membrane tubes used for nano- and micro-filtration processes. DRIJER *et al.* [7] took a large step further by proposing a new separation technology, in which the shear-induced migration towards the center line of the tube is used to decrease the particle concentration near the membrane walls, and, consequently, reducing cake formation and membrane fouling. Also adapting a formerly presented concept to the two-fluid model framework, the frictional model of BOYER *et al.* [44] was used by DONTSOV and PEIRCE [11] to predict the steady flow of a slurry in a rock fracture, considering sedimentation due to gravitational effects. The particle-phase stress was modified to include the terms from the equations of MORRIS and BOULAY [14] that account for the normal stress anisotropy.

A strategy similar to that from DONTSOV and PEIRCE [11] was given by MUNICCHI *et al.* [16]. Instead of adapting the frictional model of BOYER *et al.* [44] to the two-fluid framework, as done by DONTSOV and PEIRCE [11], MUNICCHI *et al.* [16] proceeded to merge the general model for a two-phase flow with the suspension balance model of MORRIS and BOULAY [14]. The starting point of their formulation is the OpenFOAM® solver `twoPhaseEulerFoam`, used for simulating two-phase dispersed flows. The original model was modified to introduce the equation of MORRIS and BOULAY [14] in the dispersed-phase stress tensor, which predicts the shear-induced particle migration for Stokes flow. In doing so, the model retains its original features allowing for compressibility of the phases, gravitational effects, several inter-phase momentum exchange terms (lift, drag, virtual mass, etc.), and granular pressure as part of the closure of the solid-phase stress tensor. This two-fluid model (TFM) is, therefore, the most complete model presented so far, being able to accurately predict a wide range of phenomena, and being easily accessible to the scientific community.

There is still an open discussion regarding the direct introduction of the particle stress tensor from the SBM into the dispersed-phase equations of the two-fluid models. Years after the introduction of the suspension balance model, NOTT *et al.* [49] reviewed the averaging procedure used to obtain the suspension and individual phases mass and momentum balance equations, showing that the particles' contribution to the suspension stress tensor in the SBM does not coincide with the stress tensor of the dispersed phase on a two-fluid model. In fact, the particle-phase momentum balance should reduce to a summation of forces of both hydrodynamic and non-hydrodynamic origins. This observation poses a dilemma: if there is no effective stress tensor for the particle phase, shear-induced migration could not have been successfully explained in terms of the particle stress. Both NOTT *et al.* [49]

and JAMSHIDI *et al.* [50] dived into this problem and proposed a formulation that writes the inter-phase forces as the divergence of tensors, forcing the appearance of a particle-phase stress tensor. JAMSHIDI *et al.* [50] derived the remaining term that should lead to the agreement with the particle stress of MORRIS and BOULAY [14]. However, the interpretation of the resulting model seems to return to the same form of the equations as proposed by MUNICCHI *et al.* [16]

Chapter 3

Methodology

This chapter is divided into two sections: first, both models used in this work are derived. Then, the procedure for the rheological parameters estimation using the simulated data is presented.

3.1 Description of the Models

3.1.1 Suspension Balance Model

In this section, the suspension balance model is derived for the Stokes flow of a suspension of neutrally buoyant, monodispersed, non-Brownian, and non-colloidal particles. These are the conditions that apply to the flows considered in this work, which are detailed in Section 4.3.

As mentioned earlier in this work, the condition of negligible Brownian motion is achieved if the Péclet number is sufficiently large. This number is defined as:

$$Pe = \frac{6\pi\mu_f\dot{\gamma}a^3}{kT} \tag{3.1}$$

where a is the particle radius, μ_f is the dynamic viscosity of the continuous phase, $\dot{\gamma}$ is the shear rate and kT is the thermal energy [8, 15, 23, 42]. Therefore, if $Pe \gg 1$, the effects of Brownian diffusivity can be neglected when compared to the magnitude of viscous effects. Moreover, the particle's Reynolds number that represents the ratio between the inertial and viscous forces should be infinitesimally small:

$$Re_p = \frac{\rho_f a^2\dot{\gamma}}{\mu_f} \tag{3.2}$$

where ρ_f is the suspending fluid density. So, if $Re_p \ll 1$, the flow is considered to be in the Stokes regime and the inertial terms in the transport equations can be neglected [13].

Following NOTT and BRADY [13], the conservation equations for the particle phase and for the suspension can be obtained by averaging the local and instantaneous mass and momentum conservation equations, which have the following general forms:

$$\frac{\partial \rho}{\partial t} + \nabla \cdot (\rho \mathbf{u}) = 0 \tag{3.3}$$

$$\rho \frac{D\mathbf{u}}{Dt} = \nabla \cdot \boldsymbol{\sigma} + \mathbf{b} \tag{3.4}$$

where ρ is the density, $\mathbf{u}$ is the velocity, $\mathbf{b}$ represents the body forces, and $\boldsymbol{\sigma}$ is the stress tensor. The equations above are valid for any material point in the flow domain at any time. The averaging process is omitted here, but it can be found in detail in the works of DREW and LAHEY [28] and MAZZEI [29].

Particle Phase Equations

By averaging Equation 3.3 over the particles, the resulting continuity equation reads:

$$\frac{\partial (\rho_p \phi)}{\partial t} + \nabla \cdot (\rho_p \phi \mathbf{u}_p) = 0 \tag{3.5}$$

where ϕ is the dispersed-phase fraction, and the subscript p denotes a particle-averaged property. Since the particle density ρ_p is constant, Equation 3.5 simplifies to:

$$\frac{\partial \phi}{\partial t} + \nabla \cdot (\phi \mathbf{u}_p) = 0. \tag{3.6}$$

The particle flux $\mathbf{J}_p = \phi \mathbf{u}_p$ is unknown and needs to be determined. However, it is more convenient to rewrite the continuity equation in terms of the relative motion between the suspension and the particle phase. Defining the relative migration flux $\mathbf{J}$ as:

$$\mathbf{J} = \phi \left(\mathbf{u}_p - \mathbf{u}_s \right) \tag{3.7}$$

where the subscript s indicates a suspension averaged property, and using the fact that $\nabla \cdot \mathbf{u}_s = 0$, Equation 3.6 can be rewritten as:

$$\frac{\partial \phi}{\partial t} + \mathbf{u}_s \cdot \nabla \phi = -\nabla \cdot \mathbf{J}. \tag{3.8}$$

To find an expression for $\mathbf{J}$, we write the averaged momentum equation for the particle phase:

$$\frac{\partial \left(\rho_p \phi \mathbf{u}_p \right)}{\partial t} + \nabla \cdot (\rho_p \phi \mathbf{u}_p \mathbf{u}_p) = \nabla \cdot \mathbf{S}_p + \mathbf{f}_p + \mathbf{b}_p \tag{3.9}$$

where $\mathbf{S}_p$ is the effective stress tensor of the particle phase, and $\mathbf{f}_p$ and $\mathbf{b}_p$ are, respectively, the inter-phase and body forces acting on the particles. Considering the gravitational force to be the only body force acting on the system, for a suspension of neutrally buoyant particles, $\mathbf{b}_p = 0$. Also, all of the inertial terms on the left-hand side of this equation can be neglected for Stokes flow, and Equation 3.9 reduces to:

$$0 = \nabla \cdot \mathbf{S}_p + \mathbf{f}_p. \tag{3.10}$$

Considering the only inter-phase force to be the drag force ($\mathbf{f}_p^d$), the expression for $\mathbf{f}_p$ was written by NOTT and BRADY [13] in terms of the slip velocity between the particle phase and the suspension:

$$\mathbf{f}_p = \mathbf{f}_p^d = -\frac{9\mu_f \phi}{2a^2 f(\phi)} (\mathbf{u}_p - \mathbf{u}_s). \tag{3.11}$$

The hindrance function $f(\phi)$ is the ratio between the settling velocity of the particles in a suspension of local concentration ϕ and the Stokes settling velocity of an isolated particle. It represents the mobility of the particles and is typically used to correct the Stokes drag force coefficient for suspensions even in the case of neutrally buoyant particles [14]. NOTT and BRADY [13] and MORRIS and BRADY [32] used the expression given by PHILLIPS *et al.* [51] for the hindrance function, determined from the results of several particles' settling simulations performed using Stokesian Dynamics. Writing the drag force in Equation 3.11 in terms of $\mathbf{u}_p - \mathbf{u}_s$ is in agreement with the usual form of the equations solved using SD, which are also written in terms of the slip velocity between the particle phase and the suspension. In this work, $f(\phi)$ is modeled according to MILLER and MORRIS [6], who also wrote the drag force in terms of the slip velocity $\mathbf{u}_p - \mathbf{u}_s$, and adapted the hindrance function of RICHARDSON and ZAKI [52] to ensure that migration ceases when ϕ approaches maximum packing, which reads:

$$f(\phi) = \left(1 - \frac{\phi}{\phi_m}\right)(1 - \phi)^{\alpha - 1} \tag{3.12}$$

with $\alpha = 4$ and the maximum packing fraction set to $\phi_m = 0.68$.

Introducing the drag force definition from Equation 3.11 into Equation 3.10, an expression is found for the migration flux $\mathbf{J}$:

$$0 = \nabla \cdot \mathbf{S}_p - \frac{9\mu_f}{2a^2 f(\phi)} \phi (\mathbf{u}_p - \mathbf{u}_s) \tag{3.13}$$

$$\mathbf{J} = \frac{2a^2 f(\phi)}{9\mu_f} \nabla \cdot \mathbf{S}_p. \tag{3.14}$$

Notice that, if $\nabla \cdot \mathbf{S}_p$ is zero, the last equation dictates that migration ceases. According to Equation 3.14, it is the divergence of the particle-phase stress tensor that causes the particle migration, which can be predicted by properly modeling $\mathbf{S}_p$.

The mass and momentum conservation equations for the particle phase are now coupled by introducing the definition of $\mathbf{J}$ from Equation 3.14 into Equation 3.8, yielding the final form of the particle-phase continuity equation:

$$\frac{\partial \phi}{\partial t} + \mathbf{u}_s \cdot \nabla \phi = -\frac{2a^2}{9\mu_f} \nabla \cdot \left[f(\phi) \nabla \cdot \mathbf{S}_p \right]. \tag{3.15}$$

It is still necessary to provide a closure model for the particle-phase stress tensor $\mathbf{S}_p$. The first model proposed by NOTT and BRADY [13] assumes a viscous response:

$$\mathbf{S}_p = p_p \mathbf{I} + 2\mu_p \mathbf{E}_s + \boldsymbol{\chi} \tag{3.16}$$

where p_p is the particle pressure, $\mathbf{I}$ is the identity matrix and μ_p is called the particle-phase shear viscosity, introducing a dependence of the shear stress on the particle-phase fraction. Normal stress anisotropy is accounted for by the term $\boldsymbol{\chi}$, but it is neglected by the authors under the assumption that it does not play a role in the rectilinear flows under analysis in their work. $\mathbf{E}_s$ is the rate of strain tensor, defined generally as:

$$\mathbf{E}_i = \frac{1}{2} \left[\nabla \mathbf{u}_i + (\nabla \mathbf{u}_i)^T \right], \qquad i = s, f, p \tag{3.17}$$

where the subscript f indicates a continuous-phase (hereinafter referred to as *fluid*) averaged property, and the shear rate is defined by $\dot{\gamma} = \sqrt{2\mathbf{E}_s : \mathbf{E}_s}$.

MORRIS and BOULAY [14] proposed a formulation of the normal stress tensor which accounts for the effects of anisotropy:

$$\mathbf{S}_p = 2\mu_p \mathbf{E}_s - \mu_n \dot{\gamma} \mathbf{Q} \tag{3.18}$$

where μ_n is a function of ϕ called the particle-phase normal stress viscosity, introducing the dependence of the normal stress on the particle-phase fraction. Tensor $\mathbf{Q}$ is the normal stress tensor that introduces the anisotropy in $\mathbf{S}_p$, being diagonal with respect to the directions 1, 2, and 3 of a viscosimetric flow, where 1 stands for the direction of the flow, 2 for the direction of the velocity gradient and 3 for the vorticity vector direction. It is defined by a 3×3 matrix:

$$\mathbf{Q} = \begin{bmatrix} \lambda_1 & 0 & 0 \\ 0 & \lambda_2 & 0 \\ 0 & 0 & \lambda_3 \end{bmatrix}. \tag{3.19}$$

The constant coefficients $\lambda_1 = 1.0$, $\lambda_2 = 0.8$ and $\lambda_3 = 0.5$ were defined by MORRIS and BOULAY [14] in a way that ensures both anisotropy and agreement with experimental and Stokesian Dynamics simulations data. The resulting suspension normal stresses are taken to be compressive, i.e., $S_{s,11},\ S_{s,22},\ S_{s,33} < 0$, and respect the relation $|S_{s,11}| > |S_{s,22}| > |S_{s,33}|$, as observed by YURKOVETSKY [25].

In terms of unit vectors, represented by $\hat{\mathbf{e}}$, the anisotropic tensor can also be written as:

$$\mathbf{Q} = \lambda_1 \hat{\mathbf{e}}_1 \hat{\mathbf{e}}_1 + \lambda_2 \hat{\mathbf{e}}_2 \hat{\mathbf{e}}_2 + \lambda_3 \hat{\mathbf{e}}_3 \hat{\mathbf{e}}_3. \tag{3.20}$$

From the definition of $\mathbf{Q}$, it is clear that the directions of the coordinate system chosen to write the model equations should coincide with the directions of $\hat{\mathbf{e}}_1$, $\hat{\mathbf{e}}_2$ and $\hat{\mathbf{e}}_3$. For Couette flow, in a cylindrical coordinate system, directions $(1, 2, 3)$ are (θ, r, z). Therefore, in this case, $|S_{s,\theta\theta}| > |S_{s,rr}| > |S_{s,zz}|$ can be achieved by simply shifting the position of the coefficients in the diagonal of tensor $\mathbf{Q}$, as done by MORRIS and BOULAY [14] when analyzing the model predictions for this geometry. If one wishes to solve the Couette flow equations using a Cartesian coordinate system or the flow over a contraction/expansion, e.g., the current formulation of the normal stress is not suitable. It is, therefore, a frame-dependent model that cannot be directly applied to a generic flow.

To deal with the frame-dependency of the anisotropic tensor, MILLER *et al.* [33] formulated a two-dimensional frame-invariant form of the suspension normal stress based on the local kinematics of the flow. Since it is not the strategy adopted in this work, it won't be described here and detailed information can be found in their original work [33]. A more direct formulation was presented by MUNICCHI *et al.* [16] for the two-fluid model, which replaces the unit vectors from the original definition of $\mathbf{Q}$ in Equation 3.20 with unit vectors defined using the velocity field of the particle phase,

$$\hat{\mathbf{e}}_1 = \frac{\mathbf{u}_p}{||\mathbf{u}_p||}\ , \qquad \hat{\mathbf{e}}_3 = \frac{\nabla \times \mathbf{u}_p}{||\nabla \times \mathbf{u}_p||}\ , \qquad \hat{\mathbf{e}}_2 = \hat{\mathbf{e}}_1 \times \hat{\mathbf{e}}_3. \tag{3.21}$$

Notice that the local coordinate system as defined by Equation 3.21 is left-handed. For a Couette flow with positive (anti-clockwise) rotation of the inner cylinder, this equation yields $\hat{\mathbf{e}}_1 = \hat{\mathbf{e}}_\theta$, $\hat{\mathbf{e}}_3 = \hat{\mathbf{e}}_z$ and $\hat{\mathbf{e}}_2 = \hat{\mathbf{e}}_\theta \times \hat{\mathbf{e}}_z = \hat{\mathbf{e}}_r$. Adapting the idea presented in Equation 3.21, the unit vectors can be defined in terms of the suspension velocity:

$$\hat{\mathbf{e}}_1 = \frac{\mathbf{u}_s}{||\mathbf{u}_s||}\ , \qquad \hat{\mathbf{e}}_3 = \frac{\nabla \times \mathbf{u}_s}{||\nabla \times \mathbf{u}_s||}\ , \qquad \hat{\mathbf{e}}_2 = \hat{\mathbf{e}}_1 \times \hat{\mathbf{e}}_3. \tag{3.22}$$

For viscosimetric flows where directions $(1, 2, 3)$ are constant with respect to the

cylindrical or spherical coordinate system, the anisotropic tensor $\mathbf{Q}$ can be written in Cartesian coordinates using a geometric coordinate system transformation. Consider the Couette flow with positive rotation of the inner cylinder. In the steady state, $\mathbf{u}_s = u_{s,\theta}(r)\hat{\mathbf{e}}_\theta$, and the anisotropic tensor $\mathbf{Q}$ written in cylindrical coordinates is:

$$\mathbf{Q} = \lambda_1 \hat{\mathbf{e}}_\theta \hat{\mathbf{e}}_\theta + \lambda_2 \hat{\mathbf{e}}_r \hat{\mathbf{e}}_r + \lambda_3 \hat{\mathbf{e}}_z \hat{\mathbf{e}}_z. \tag{3.23}$$

Using the relations between Cartesian and cylindrical unit vectors:

$$\hat{\mathbf{e}}_r = \cos\theta \hat{\mathbf{e}}_x + \sin\theta \hat{\mathbf{e}}_y, \qquad \hat{\mathbf{e}}_\theta = -\sin\theta \hat{\mathbf{e}}_x + \cos\theta \hat{\mathbf{e}}_y \tag{3.24}$$

where $\theta = \arctan(y/x)$, tensor $\mathbf{Q}$ in Cartesian coordinates for the Couette flow is:

$$\begin{aligned}\mathbf{Q} = &\left(\lambda_1 \sin^2\theta + \lambda_2 \cos^2\theta\right) \hat{\mathbf{e}}_x \hat{\mathbf{e}}_x + \left(\lambda_2 \sin^2\theta + \lambda_1 \cos^2\theta\right) \hat{\mathbf{e}}_y \hat{\mathbf{e}}_y \\ &+ \cos\theta \sin\theta \left(\lambda_2 - \lambda_1\right) \hat{\mathbf{e}}_x \hat{\mathbf{e}}_y + \cos\theta \sin\theta \left(\lambda_2 - \lambda_1\right) \hat{\mathbf{e}}_y \hat{\mathbf{e}}_x + \lambda_3 \hat{\mathbf{e}}_z \hat{\mathbf{e}}_z.\end{aligned} \tag{3.25}$$

A full description of the functional forms for the solid-phase fraction dependency of the suspension stress is given by MORRIS and BOULAY [14]:

$$\frac{\mu_p}{\mu_f} = 2.5\phi \left(1 - \frac{\phi}{\phi_m}\right)^{-1} + K_s \left(1 - \frac{\phi_m}{\phi}\right)^{-2} \tag{3.26}$$

$$\frac{\mu_n}{\mu_f} = K_n \left(1 - \frac{\phi_m}{\phi}\right)^{-2} \tag{3.27}$$

with constant coefficients $K_s = 0.1$ and $K_n = 0.75$. It should be noticed that both MORRIS and BOULAY [14] and DBOUK *et al.* [15] gave the μ_p expression with typographical errors. Equation 3.26 is the same used by INKSON *et al.* [53] and MILLER and MORRIS [6], and it is the correct form as it retrieves the simplified Einstein's relation for dilute suspensions when $\phi \to 0$ [19].

Suspension Equations

The application of the averaging procedure to Equations 3.3 and 3.4 over all the suspension volume yields:

$$\frac{\partial \rho_s}{\partial t} + \nabla \cdot (\rho_s \mathbf{u}_s) = 0 \tag{3.28}$$

$$\frac{\partial (\rho_s \mathbf{u}_s)}{\partial t} + \nabla \cdot (\rho_s \mathbf{u}_s \mathbf{u}_s) = \nabla \cdot \mathbf{S}_s. \tag{3.29}$$

For a constant ρ_s, and considering Stokes flow, they simplify to:

$$\nabla \cdot \mathbf{u}_s = 0 \tag{3.30}$$

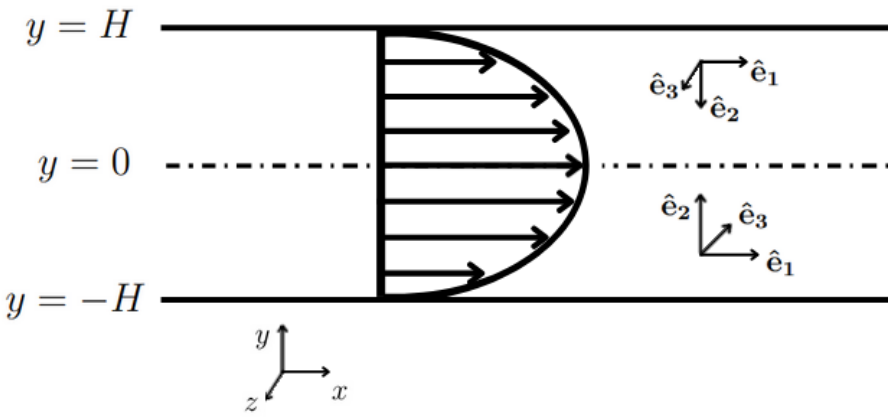

Figure 3.1: Fully-developed flow on a linear channel.

$$\nabla \cdot \mathbf{S}_s = 0. \tag{3.31}$$

The stress tensor of the suspension is given by the sum of the stress tensors for the solid and fluid phases, i.e., $\mathbf{S}_s = \mathbf{S}_p + \mathbf{S}_f$. For a Newtonian continuous phase:

$$\mathbf{S}_f = -p\mathbf{I} + 2\mu_f \mathbf{E}_s. \tag{3.32}$$

Combining with the particle-phase stress tensor of MORRIS and BOULAY [14] (Equation 3.18) the resulting suspension stress is:

$$\mathbf{S}_s = -p\mathbf{I} + 2\mu_s \mathbf{E}_s - \mu_n \dot{\gamma} \mathbf{Q} \tag{3.33}$$

with the suspension's viscosity defined as $\mu_s = \mu_p + \mu_f$. Therefore, Equation 3.31 can be rewritten as:

$$\nabla \cdot (-p\mathbf{I} + 2\mu_s \mathbf{E}_s - \mu_n \dot{\gamma} \mathbf{Q}) = 0. \tag{3.34}$$

The role of the normal stresses in particle migration can be easily illustrated for the channel flow. Consider the fully-developed steady-state Stokes flow of a suspension in a 2-D channel, according to Figure 3.1, and the Cartesian and local coordinate systems (the latter defined by Equation 3.22). The suspension's velocity profile is described as $\mathbf{u}_s = u_{s,x}(y)\hat{\mathbf{e}}_x$ in Cartesian coordinates and, using x_i to represent the coordinate in the direction of $\hat{\mathbf{e}}_i$, as $\mathbf{u}_s = u_{s,x_1}(x_2)\hat{\mathbf{e}}_1$ in the local coordinate system.

The suspension's momentum conservation, (Eq. 3.31) on the x_2-direction is:

$$(\nabla \cdot \mathbf{S}_s)_{x_2} = \frac{\partial S_{s,12}}{\partial x_1} + \frac{\partial S_{s,22}}{\partial x_2} = 0. \tag{3.35}$$

For the fully-developed flow, there is no dependence on the x-coordinate, and since $x_1 = x$, $\forall x$, the first term on the right-hand side of the last equation vanishes.

Therefore:

$$\left(\nabla \cdot \mathbf{S}_s\right)_{x_2} = \frac{\partial S_{s,22}}{\partial x_2} = 0. \tag{3.36}$$

Using the definition of the suspension stress from Equation 3.33:

$$S_{s,22} = -\mu_n(\phi)\dot{\gamma}Q_{22} = -\mu_n(\phi)\dot{\gamma}\lambda_2 \tag{3.37}$$

and replacing it into Equation 3.36, the suspension's momentum equation in the x_2-direction is:

$$\left(\nabla \cdot \mathbf{S}_s\right)_{x_2} = -\frac{\partial}{\partial x_2}\left[\mu_n(\phi)\dot{\gamma}\lambda_2\right] = 0 \tag{3.38}$$

which leads to:

$$\mu_n(\phi)\dot{\gamma}\lambda_2 = cte, \ \forall x_2. \tag{3.39}$$

With $x_2 = y$ for $y < 0$ and $x_2 = -y$ for $y > 0$, Equation 3.39 dictates that $\mu_n(\phi)\dot{\gamma}\lambda_2$ should be constant with respect to the y-coordinate. If $\dot{\gamma}$ varies with y with a maximum value at the walls and a minimum value at the center line of the channel, there should be a non-uniform solid-phase fraction profile that provides a variation of $\mu_n(\phi)$ contrary to the changes of the shear rate in order to respect the condition given by Equation 3.39. Since $\mu_n(\phi)$ is a monotonically increasing function of ϕ, that is achieved if ϕ presents its maximum value at the center line of the channel and its minimum value at the walls. It is clear, then, that the shear-induced particle migration is closely related to the normal stress.

Non-local Formulation

To account for the non-local effects described in the previous chapter, NOTT and BRADY [13] remodeled the particle's normal stresses as a function of the suspension temperature T_s, which represents the fluctuations on the mean velocity of the particles. The addition of this new field variable requires solving an additional transport equation. Since this concept does not take part in the final model used in this work, modeling of the suspension temperature is omitted here and the reader is referred to the original work of NOTT and BRADY [13] for more information.

The formulation followed in this work is the one proposed by MILLER and MORRIS [6], based on the introduction of an effective shear rate ($\dot{\gamma}_{eff}$), that consists of adding a non-local correction to the currently calculated shear rate:

$$\dot{\gamma}_{eff} = \dot{\gamma} + \dot{\gamma}_{nl}, \qquad \dot{\gamma}_{nl} = \epsilon u_{s,max} \tag{3.40}$$

where $\dot{\gamma}_{nl}$ is the non-local correction, ϵ is the parameter that carries the relation between the particle size and the flow length scale, and $u_{s,max}$ is the maximum value

of the suspension velocity. For Couette flow $\epsilon = 0$ and for channel flow $\epsilon = a/L_{ch}^2$, where L_{ch} is the characteristic length of the flow. Hence, a small constant value is added to the shear rate, which does not distort the shape of the shear rate profile and still guarantees that the shear rate is non-zero everywhere. The local shear rate is replaced with its effective value in Equation 3.34, so, for simplicity, the subscript eff is dropped hereinafter.

3.1.2 Two-Fluid Model

The equations for the two-fluid model can be obtained in a very similar way to those for the mixture model. In contrast to the procedure adopted in the previous section, equations for the TFM will not be restricted to the particular conditions of the studied cases, except for the assumption of a negligible contribution of Brownian motion. The main goal was to obtain the model given by MUNICCHI *et al.* [16], with a full description of the multiphase flow, which is then compared to the simplified suspension balance model.

Continuity Equations

Averaging of the continuity equation for the particle phase yields essentially the same equation obtained for the SBM. Hence, it is repeated here, keeping its general form:

$$\frac{\partial \left(\rho_p \phi\right)}{\partial t} + \nabla \cdot \left(\rho_p \phi \mathbf{u}_p\right) = 0. \tag{3.5}$$

Since the two-fluid model solves for $\mathbf{u}_p$, there is no need to write the flux $\phi \mathbf{u}_p$ in terms of the relative velocity.

Averaging Equation 3.3 over the volume of the continuous phase yields the fluid continuity equation:

$$\frac{\partial \left[\left(1-\phi\right)\rho_f\right]}{\partial t} + \nabla \cdot \left[\left(1-\phi\right)\rho_f \mathbf{u}_f\right] = 0. \tag{3.41}$$

Momentum Equations

An equation identical to 3.9 is obtained for the particle-phase momentum conservation. It is repeated here, without neglecting any contribution from inertial terms or compressibility effects:

$$\frac{\partial \left(\rho_p \phi \mathbf{u}_p\right)}{\partial t} + \nabla \cdot \left(\rho_p \phi \mathbf{u}_p \mathbf{u}_p\right) = \nabla \cdot \mathbf{S}_p + \mathbf{f}_p + \mathbf{b}_p. \tag{3.9}$$

Averaging of Equation 3.4 over the continuous phase volume yields the fluid

momentum equation:

$$\frac{\partial\left[\left(1-\phi\right)\rho_f\mathbf{u}_f\right]}{\partial t}+\nabla\cdot\left[\left(1-\phi\right)\rho_f\mathbf{u}_f\mathbf{u}_f\right]=\nabla\cdot\mathbf{S}_f-\mathbf{f}_p+\mathbf{b}_f. \tag{3.42}$$

Notice that the term $\mathbf{f}_p$, representing the interaction force between the phases, appears in the momentum equations for both phases with opposite signs. This interphase force is now the combination of every possible source of momentum transfer between the phases, such as the drag, lift, and virtual mass forces. Since the only interaction considered in this work is the drag force, the formulation of the other types of interactions is not addressed here. The numerical solver allows for the inclusion of other interaction terms, but they were not used in any of the performed simulations.

For the two-fluid models, the drag force is typically written in terms of the slip velocity between the phases, i.e., $\mathbf{u}_p-\mathbf{u}_f$. As also pointed out by DONTSOV and PEIRCE [11], in order to use an expression for the drag force with the TFM that is compatible with the hindrance function and drag force definitions in the SBM, Equation 3.11 needs to be rewritten using the relation $\mathbf{u}_p-\mathbf{u}_s=\left(1-\phi\right)\left(\mathbf{u}_p-\mathbf{u}_f\right)$:

$$\mathbf{f}_p^d=-\frac{9\mu_f}{2a^2f(\phi)}\phi\left(1-\phi\right)\left(\mathbf{u}_p-\mathbf{u}_f\right) \tag{3.43}$$

$$\mathbf{f}_p^d=-\beta\left(\mathbf{u}_p-\mathbf{u}_f\right),\qquad\beta=\frac{9\mu_f}{2a^2f(\phi)}\phi\left(1-\phi\right). \tag{3.44}$$

Equations 3.11 and 3.44 are compatible due to the $(1-\phi)$ factor that appears in the drag coefficient β. However, MUNICCHI *et al.* [16] wrote the drag force expression as:

$$\mathbf{f}_p^d=\frac{9\mu_f\phi}{2d^2f(\phi)}\left(\mathbf{u}_p-\mathbf{u}_f\right) \tag{3.45}$$

with the hindrance function given by Equation 3.12 and using $\alpha=4$. The authors did not address the change in the definition of the slip velocity used in the drag force equation. Therefore, the expression used by MUNICCHI *et al.* [16] corresponds to a value of $\alpha=5$ in the suspension balance model used by MILLER and MORRIS [6], and not $\alpha=4$ as recommended by the authors. Thus, to use the same expression with both models, the value of $\alpha=4$ is considered in this work along with Equations 3.12 and 3.44, corresponding to a value of $\alpha=3$ for the hindrance function coefficient in Equation 3.45 as defined by MUNICCHI *et al.* [16]. Moreover, the expression given in Equation 3.45 is wrong, since it is written in terms of the particles *diameter* d instead of the particle radius, without applying any conversion factor. In the present work, the numerical code provided by MUNICCHI *et al.* [16] (available on `https://github.com/fmuni/twoFluidsNBSuspensionFoam`) was used to assess the two-fluid model, and this error was also identified in the numerical code, which

was fixed before performing any of the reported simulations.

MUNICCHI *et al.* [16] also included another source of interaction between phases called *generalized buoyancy*, here represented by $\mathbf{f}_p^b$, and given by:

$$\mathbf{f}_p^b = \phi\nabla\cdot(\boldsymbol{\tau}_f - p\mathbf{I}) - (1-\phi)\,\nabla p_p \tag{3.46}$$

where p is the shared pressure that satisfies the pressure equation, defined by $p = p_f + p_p$, and the deviatoric stress tensor $\boldsymbol{\tau}_f$ defined generally by:

$$\boldsymbol{\tau}_i = 2\mu_i\mathbf{E}_i - \frac{2}{3}\mu_i\,(\nabla\cdot\mathbf{u}_i)\,\mathbf{I}, \qquad i = f, p. \tag{3.47}$$

Then, the inter-phase force is the sum of two contributions, $\mathbf{f}_p = \mathbf{f}_p^d + \mathbf{f}_p^b$. To better understand the role of this buoyancy force, the right-hand side of the fluid's momentum conservation equation is written here exactly as it is defined in the original paper of MUNICCHI *et al.* [16]:

$$RHS = -\nabla\cdot(p\mathbf{I} - \boldsymbol{\tau}_f) - \phi\nabla\cdot(\boldsymbol{\tau}_f - p\mathbf{I}) + (1-\phi)\,\nabla p_p - \mathbf{f}_p^d - \mathbf{b}_f \tag{3.48}$$

which can also be written as:

$$RHS = (1-\phi)\,\nabla\cdot\boldsymbol{\tau}_f - (1-\phi)\,\nabla p + (1-\phi)\,\nabla p_p - \mathbf{f}_p^d - \mathbf{b}_f. \tag{3.49}$$

Looking at the right-hand side of the particle-phase momentum conservation equation:

$$\begin{aligned} RHS &= \nabla\cdot\mathbf{S}_p + \phi\nabla\cdot(\boldsymbol{\tau}_f - p\mathbf{I}) - (1-\phi)\,\nabla p_p + \mathbf{f}_p^d + \mathbf{b}_p \\ &= \nabla\cdot\mathbf{S}_p - \phi\nabla p + \phi\nabla\cdot\boldsymbol{\tau}_f - (1-\phi)\,\nabla p_p + \mathbf{f}_p^d + \mathbf{b}_p. \end{aligned} \tag{3.50}$$

The momentum conservation equations for both phases (Equations 3.49 and 3.50) share a term related to the particle pressure, $(1-\phi)\,\nabla p_p$, which appears with opposite signs and is modeled as a function of the granular temperature. This particle pressure contribution was disregarded for all performed simulations. The interaction term $\phi\nabla\cdot\boldsymbol{\tau}_f$ also appears in Equations 3.49 and 3.50 with opposite signs. Equations 30 and 31 of MUNICCHI *et al.* [16], which show the semi-discrete momentum conservation equations for both phases, do not agree with the implementation of the corresponding semi-discrete equations in the numerical solver (`https://github.com/fmuni/twoFluidsNBSuspensionFoam`). Hence, both $(1-\phi)\,\nabla p_p$ and $\phi\nabla\cdot\boldsymbol{\tau}_f$ terms were disregarded from this point forward, and the only part of the buoyancy force $\mathbf{f}_p^b$ considered was $-\phi\nabla p$.

Considering the above remarks, the employed expressions for the momentum conservation equations for the particle's and fluid phases are, respectively:

$$\frac{\partial\left(\rho_p\phi\mathbf{u}_p\right)}{\partial t}+\nabla\cdot\left(\rho_p\phi\mathbf{u}_p\mathbf{u}_p\right)=\nabla\cdot\mathbf{S}_p-\phi\nabla p+\mathbf{f}_p^d+\mathbf{b}_p \tag{3.51}$$

$$\frac{\partial\left[\left(1-\phi\right)\rho_f\mathbf{u}_f\right]}{\partial t}+\nabla\cdot\left[\left(1-\phi\right)\rho_f\mathbf{u}_f\mathbf{u}_f\right]=\nabla\cdot\mathbf{S}_f-\left(1-\phi\right)\nabla p-\mathbf{f}_p^d+\mathbf{b}_f. \tag{3.52}$$

The only body forces accounted for are the gravitational forces:

$$\mathbf{b}_f=\left(1-\phi\right)\rho_f\mathbf{g},\qquad\mathbf{b}_p=\phi\rho_p\mathbf{g}. \tag{3.53}$$

The particle-phase stress tensor $\mathbf{S}_p$ is:

$$\mathbf{S}_p=2\mu_p\mathbf{E}_p+\left(\kappa_p-\frac{2}{3}\mu_p\right)\left(\nabla\cdot\mathbf{u}_p\right)\mathbf{I}-\mu_n\dot{\gamma}\mathbf{Q} \tag{3.54}$$

where κ_p is the bulk viscosity from Newton's law of viscosity [54]. For the first two terms on the right-hand side of Equation 3.54, the original model of MUNICCHI *et al.* [16] also includes contributions that depend on the granular temperature. Since these contributions can be neglected for the applications studied in this work, the corresponding terms were not included for all performed simulations and are not addressed here. The value of the bulk viscosity, which is proportional to $\phi^2 d\sqrt{\Theta}$ (with Θ being the granular temperature), can be neglected in comparison to μ_p. Thus, the particle-phase stress tensor becomes:

$$\mathbf{S}_p=2\mu_p\mathbf{E}_p-\frac{2}{3}\mu_p\left(\nabla\cdot\mathbf{u}_p\right)\mathbf{I}-\mu_n\dot{\gamma}\mathbf{Q}. \tag{3.55}$$

Writing the frame-invariant formulation of the anisotropic tensor $\mathbf{Q}$ according to MUNICCHI *et al.* [16]:

$$\hat{\mathbf{e}}_1=\frac{\mathbf{u}_p}{||\mathbf{u}_p||}\ ,\qquad\hat{\mathbf{e}}_3=\frac{\nabla\times\mathbf{u}_p}{||\nabla\times\mathbf{u}_p||}\ ,\qquad\hat{\mathbf{e}}_2=\hat{\mathbf{e}}_1\times\hat{\mathbf{e}}_3. \tag{3.56}$$

For a Newtonian fluid phase, the stress tensor is written as:

$$\mathbf{S}_f=\boldsymbol{\tau}_f=2\mu_f\mathbf{E}_f-\frac{2}{3}\mu_f\left(\nabla\cdot\mathbf{u}_f\right)\mathbf{I}. \tag{3.57}$$

3.2 Rheological Parameters Estimation

In this section, it is shown how the simulations using the suspension balance model and the two-fluid model are used as a computational experiment.

Several simulations of the suspension flow on a Couette cell were performed using both models, with the rotating speed of the inner cylinder varying from 0.5 to 48 *rps*. The wide range of rotation velocities was chosen to cover the typical range of applied shear rates in Couette rheometers with suspensions and emulsions [55–58]. The highest velocities considered in this work extrapolate the shear rate range observed in the mentioned studies.

The simulations' results provide the full description of the suspension behavior inside the gap as predicted by the models. These results are compared to the ones that would be obtained in a classic rheometric experiment. Typically, to measure the rheological properties of a suspension, it is assumed to be homogeneous and to follow a chosen rheological model (Newtonian or non-Newtonian). The parameters of this rheological model are then estimated from the torque measurements at the rotating cylinder, by fitting the data to an analytical solution for the flow. If the fit is inadequate, another model can be selected and this procedure repeated. The goal is to verify if the rheological model that explains the experimental data obtained by typical rheometry experiments actually provides an accurate rheological description of the suspension. The procedure is as follows:

1. Analytical solutions for the homogeneous flow of a power-law fluid are developed for both Couette and straight channel flows;

2. A batch of CFD simulations is performed for the Couette flow using both the SBM and TFM at several shear rates and for different gap sizes using OpenFOAM®;

3. The resulting torque at the rotating cylinder, calculated from the simulated velocity fields, is used to estimate the parameters of the power-law model using the analytical solution for the Couette flow found in Step 1;

4. A second batch of simulations is performed for the flow of the same suspension in straight channels with different channel widths and mean velocities;

5. The model parameters obtained in Step 3 are used to estimate the pressure drops for the fully-developed section of the channel flows;

6. The pressure drops estimated in Step 5 are compared to the simulated values obtained using the TFM for the same channel flow conditions;

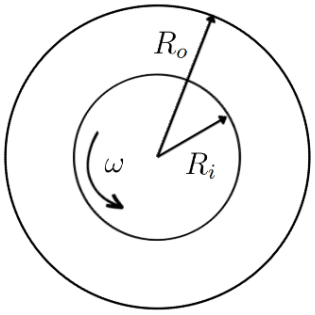

Figure 3.2: Couette rheometer geometry used to obtain the analytical solution for a power-law fluid.

7. The simulated pressure drops are also used to estimate the power-law model parameters, which are compared to their values estimated in Step 3.

3.2.1 Analytical Solutions

Consider the incompressible two-dimensional Stokes flow of a homogeneous power-law fluid on a cylindrical Couette cell, as shown in Figure 3.2. The inner cylinder of radius R_i rotates at an angular velocity ω, while the outer cylinder of radius R_o is stationary. The total length L of the cylinder is considered to be sufficient to neglect end effects. The effects of gravity are disregarded as the particles are neutrally buoyant.

The deviatoric stress tensor of a power-law fluid is given by [54]:

$$\boldsymbol{\tau} = 2m\dot{\gamma}^{n-1}\mathbf{E} \tag{3.58}$$

where m and n are the two model parameters to be determined from the simulations. If $n = 1$, Equation 3.58 reduces to the Newtonian model. Hence, $m = \mu$.

The detailed procedure to obtain the analytical solution is given in Appendix A. The final equation for the z-component of the torque at the inner cylinder is:

$$\left.\frac{T_z}{L}\right|_{r=R_i} = -2\pi m \left(\frac{2\omega}{n}\right)^n \left(R_o^{-2/n} - R_i^{-2/n}\right)^{-n}. \tag{3.59}$$

For the channel flow, consider again the incompressible two-dimensional Stokes flow of the same homogeneous power-law fluid at the steady state, flowing in a channel with half-width H, as represented in Figure 3.3. Fluid enters the channel with a mean velocity $\overline{u}$ and, neglecting the effects of gravity, the developed flow will be symmetric with respect to the center line at $y = 0$. The goal of this analysis is to determine an expression for the pressure drop between the x-normal surfaces of the control volume represented in Figure 3.3.

Again, the detailed procedure is detailed in Appendix A. The final expression

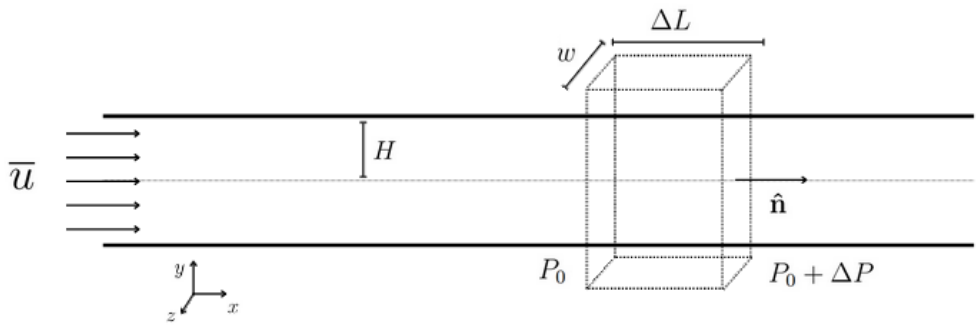

Figure 3.3: Straight 2-D channel geometry used to obtain the analytical solution for a power-law fluid.

for the fluid velocity is:

$$u_x(y) = \frac{n}{n+1}\left[\frac{1}{m}\left(-\frac{\Delta P}{\Delta L}\right)\right]^{1/n}\left[H^{1+1/n} - y^{1+1/n}\right]. \tag{3.60}$$

Using the volumetric flow rate (Q) to find a relation between the pressure drop and the mean velocity of the flow:

$$\overline{u} = \frac{Q}{2Hw} = \frac{n}{2n+1}\left[\frac{1}{m}\left(-\frac{\Delta P}{\Delta L}\right)\right]^{1/n} H^{1+1/n}. \tag{3.61}$$

Chapter 4

Numerical Procedure

The set of coupled non-linear partial differential equations of the models presented in the previous chapter are solved using OpenFOAM-v7®, an open-source CFD package written in `C++` that uses the finite volume method to solve field equations. This chapter is organized as follows: Section 4.1 presents the discretization of the models and the solution algorithms implemented in OpenFOAM®; the methodology for the grid convergence analysis is presented in Section 4.2; the studied cases and generated meshes are described in Section 4.3; the description of the simulations' setup used for all models and cases is given in Section 4.4

4.1 Implementation of the Models

4.1.1 Original Suspension Balance Model Implementation

The starting point of this work is the OpenFOAM® solver available at `https://openfoamwiki.net/index.php/Contrib/SbmFoam`. It is a partial implementation of the model described in the work of DBOUK *et al.* [15], since it features the frame-dependent formulation of the anisotropic tensor $\mathbf{Q}$ according to Equation 3.20, with the unit vectors being those of the Cartesian coordinate system. The user can define if directions 1, 2, and 3 will coincide with x, y, or z by changing the order of the parameters when setting up the simulation, but they must always coincide with the Cartesian directions. It is, therefore, a frame-dependent solver that needs adaptation in order to be applied to generic flows.

The SBM solver includes the transport equations 3.15, 3.30 and 3.31, and the closure models described in Equations 3.18 and 3.33 for the particle-phase and suspension stress tensors, respectively. The particles' normal viscosity is given by Equation 3.27 with $K_n = 0.75$. However, the particles' shear viscosity is not modeled as

Equation 3.26. Instead, it employs:

$$\frac{\mu_p}{\mu_f} = \left(\frac{1}{1-\phi/\phi_m}\right)^2 - 1. \tag{4.1}$$

Since the SBM solver is for incompressible flows, from now on, the pressure is referred to as $p^* = p/\rho$ and the viscosities as $\nu = \mu/\rho$.

Velocity Equation

The suspension's momentum conservation given by Equation 3.31 is written as:

$$-\nabla^2\left(\nu_s \mathbf{u}_s\right) - \nabla\cdot\left[\nu_s\left(\nabla\mathbf{u}_s\right)^T\right] + \nabla\cdot\left(\nu_n\dot{\gamma}\mathbf{Q}\right) = -\nabla p^*. \tag{4.2}$$

Following the finite volume discretization procedure as described in JASAK [59], let $\mathcal{M}$ be the coefficient matrix of the linear system $\mathcal{M}\mathbf{u}_s = \mathcal{B}$ obtained by the partial discretization of Equation 4.2 where $\mathcal{B}$ is the vector of source terms. With an implicit treatment of the Laplacian term in Equation 4.2, discretization of its left-hand side leads to the semi-discrete momentum equation:

$$\mathcal{A}\mathbf{u}_s - \mathcal{H} = -\nabla p^* \tag{4.3}$$

where $\mathcal{A}$ is the diagonal part of $\mathcal{M}$. Matrix $\mathcal{H}$ is defined by:

$$\mathcal{H} = (\mathcal{A} - \mathcal{M})\mathbf{u}_s + \mathcal{B} \tag{4.4}$$

Then, rewriting Equation 4.3, the suspension velocity reads:

$$\mathbf{u}_s = \frac{\mathcal{H}}{\mathcal{A}} - \frac{\nabla p^*}{\mathcal{A}}. \tag{4.5}$$

Volumetric Flux

The volumetric flux at a given cell face is defined by:

$$\varphi_i = \mathbf{u}_{i,cf}\cdot\mathbf{A}_{cf}, \qquad i = s, f, p \tag{4.6}$$

where $\mathbf{A}_{cf} = A\hat{\mathbf{n}}$ is a vector with magnitude equal to the cell's surface area A in the direction of its normal unit vector $\hat{\mathbf{n}}$. From now on, the subscript cf will always refer to the value of a property at the cell face, obtained from linear interpolation of the known values at the neighboring cell centers. Combining Equations 4.5 and 4.6,

the suspension's volumetric flux φ_s is written as:

$$\varphi_s = \left[\left(\frac{\mathcal{H}}{\mathcal{A}} \right)_{cf} - \frac{\nabla_{cf} p^*}{\mathcal{A}_{cf}} \right] \cdot \mathbf{A}_{cf} \tag{4.7}$$

where ∇_{cf} represents the evaluation of the gradient at the cell faces using the values of the variable at the neighboring cell centers.

Pressure Equation

Discretization of the suspension's continuity equation (Eq. 3.30) using the finite volume method requires that:

$$\nabla \cdot \varphi_s = 0 \tag{4.8}$$

so, replacing the resulting expression for φ_s from Equation 4.7:

$$\nabla \cdot \left[\left(\frac{\mathcal{H}}{\mathcal{A}} \right)_{cf} \cdot \mathbf{A}_{cf} \right] = \nabla \cdot \left[\left(\frac{\nabla_{cf} p^*}{\mathcal{A}_{cf}} \right) \cdot \mathbf{A}_{cf} \right] \tag{4.9}$$

where the Laplacian of the pressure on the right-hand side is discretized implicitly and the remaining terms are evaluated explicitly.

Phase Fraction Equation

The resulting continuity equation for the particles is repeated here for clarity:

$$\frac{\partial \phi}{\partial t} + \nabla \cdot (\phi \mathbf{u}_s) = -\frac{2a^2}{9\mu_f} \nabla \cdot \left[f(\phi) \nabla \cdot \mathbf{S}_p \right]. \tag{4.10}$$

The above equation is solved by evaluating ϕ on the left-hand side implicitly, and the remaining terms explicitly.

Solution Algorithm

Equations 4.3, 4.9 and 4.10 are solved following the algorithm described in Figure 4.1. The quantities `nNonOrthogonalCorrectors` and `nCorrectors` are, respectively, the number of iterations for the non-orthogonal correction loop and for the pressure-velocity coupling loop, which are chosen by the user in the simulation setup. For a generic property ε, the superscripts (n) and (o) indicate its value taken on the current or the previous time step, respectively. Notice that the time derivative does not appear on the velocity equation, consequently, both velocity and pressure are stationary. The time derivative appears only in the phase-fraction equation, hence, it is a pseudo-transient solver. This allows us to increase the time step according to

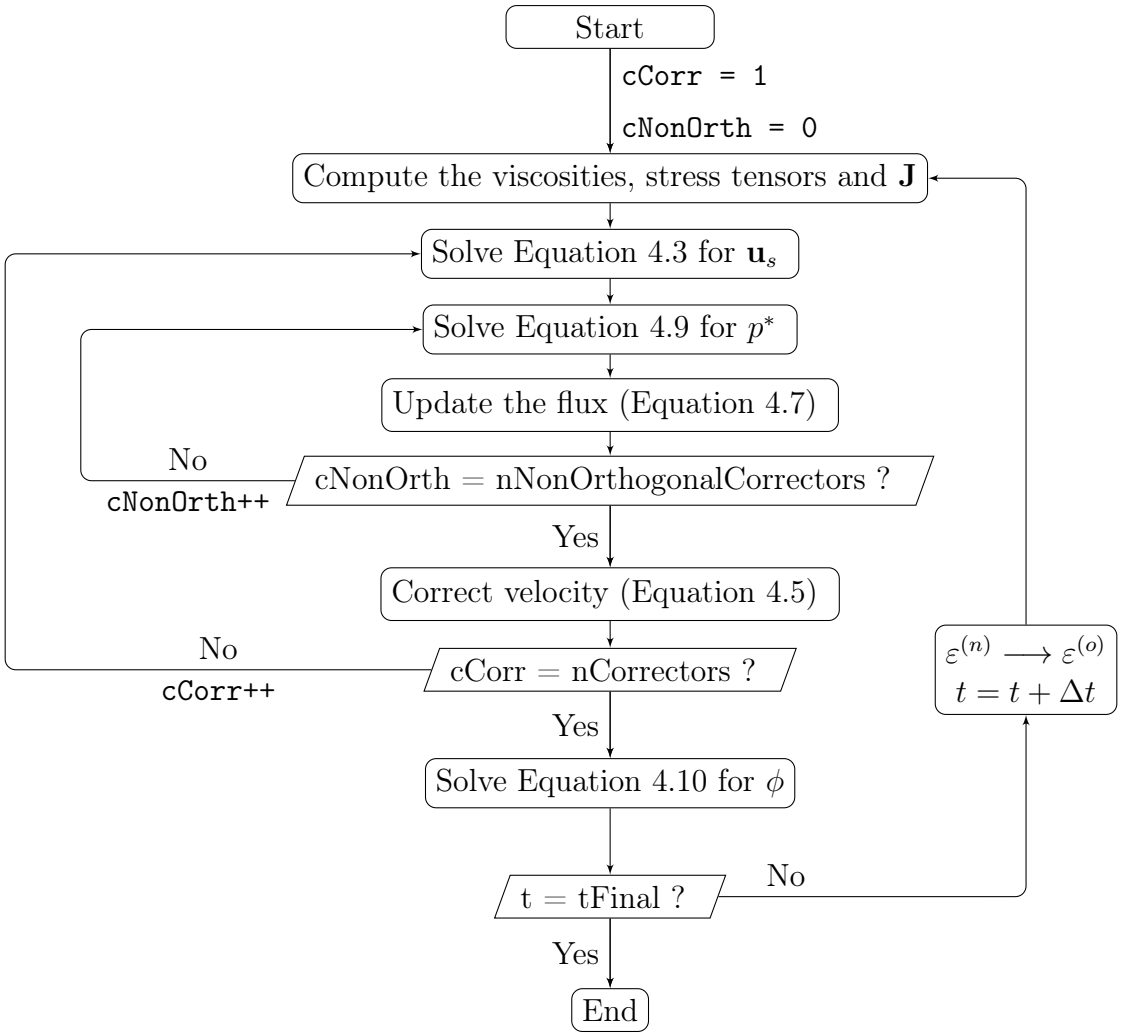

Figure 4.1: Solution algorithm for the original SBM solver (`sbm1Foam`).

the variations of ϕ between consecutive time steps to accelerate the run and reach the steady state solution faster.

4.1.2 Improvement of the Suspension Balance Model

Starting from the original solver described in Section 4.1.1, three main improvements were implemented: (i) the particles' shear viscosity model is altered from Equation 4.1 to Equation 3.26; (ii) the frame-invariant formulation of the anisotropic tensor $\mathbf{Q}$ is implemented by redefining the unit vectors of Equation 3.20 as described in Equation 3.22; and (iii) since the formulation from the item (ii) generates numerical oscillations in the solid-phase fraction field, an improved momentum interpolation scheme was implemented.

To separate the effects of each improvement on the solver and further compare their results, four different solvers were created. From now on, the original SBM solver is referred to as `sbm1Foam`, with the frame-dependent tensor $\mathbf{Q}$ and parti-

cles' shear viscosity modeled according to Equation 4.1. Solver `sbm2Foam` is Solver `sbm1Foam` but replacing Equation 4.1 with Equation 3.26. Solver `sbm3Foam` implements the frame-independent $\mathbf{Q}$ calculation using Equation 3.22 and solver `sbm4Foam` is similar to Solver `sbm3Foam` but uses the improved momentum interpolation scheme described next.

Velocity Equation

Following MUNICCHI *et al.* [16], the term $\nabla \cdot (\nu_n \dot{\gamma} \mathbf{Q})$ in Equation 4.2 is split into two contributions:

$$\nabla \cdot (\nu_n \dot{\gamma} \mathbf{Q}) = \dot{\gamma} \left(\frac{d\nu_n}{d\phi} \right) (\nabla \phi) \cdot \mathbf{Q} + \nu_n \nabla \cdot (\dot{\gamma} \mathbf{Q}) \,. \tag{4.11}$$

Then, Equation 4.2 can be written as:

$$-\nabla^2 (\nu_s \mathbf{u}_s) - \nabla \cdot \left[\nu_s \left(\nabla \mathbf{u}_s \right)^T \right] + \nu_n \nabla \cdot (\dot{\gamma} \mathbf{Q}) = -\nabla p^* - \dot{\gamma} \left(\frac{d\nu_n}{d\phi} \right) (\nabla \phi) \cdot \mathbf{Q}. \tag{4.12}$$

With the Laplacian term in Equation 4.12 being treated implicitly, discretization of its left-hand size provides the semi-discrete momentum equation:

$$\mathcal{A} \mathbf{u}_s - \mathcal{H} = -\nabla p^* - \dot{\gamma} \left(\frac{d\nu_n}{d\phi} \right) (\nabla \phi) \cdot \mathbf{Q} \tag{4.13}$$

and the suspension's velocity is:

$$\mathbf{u}_s = \left(\frac{\mathcal{H}}{\mathcal{A}} \right) - \frac{\nabla p^*}{\mathcal{A}} - \frac{1}{\mathcal{A}} \dot{\gamma} \left(\frac{d\nu_n}{d\phi} \right) (\nabla \phi) \cdot \mathbf{Q}. \tag{4.14}$$

Volumetric Flux

The suspension's volumetric flux evaluated at the cell faces, defined by Equation 4.6, is now calculated by:

$$\varphi_s = \left[\left(\frac{\mathcal{H}}{\mathcal{A}} \right)_{cf} - \frac{\nabla_{cf} p^*}{\mathcal{A}_{cf}} - \frac{1}{\mathcal{A}_{cf}} \left(\dot{\gamma} \frac{d\nu_n}{d\phi} \right)_{cf} (\nabla_{cf} \phi) \cdot (\mathbf{Q})_{cf} \right] \cdot \mathbf{A}_{cf}. \tag{4.15}$$

Pressure Equation

Again, discretization of the suspension's continuity equation using the finite volume method requires that the divergence of the volumetric flux is zero (Equation 4.8).

So, from Equation 4.15:

$$\begin{aligned} &\nabla \cdot \left[\left(\frac{\mathcal{H}}{\mathcal{A}} \right)_{cf} \cdot \mathbf{A}_{cf} - \frac{1}{\mathcal{A}_{cf}} \left(\dot{\gamma} \frac{d\nu_n}{d\phi} \right)_{cf} (\nabla_{cf}\phi) \cdot (\mathbf{Q})_{cf} \cdot \mathbf{A}_{cf} \right] \\ &= \nabla \cdot \left[\left(\frac{\nabla_{cf} p^*}{\mathcal{A}_{cf}} \right) \cdot \mathbf{A}_{cf} \right] \end{aligned} \tag{4.16}$$

where the Laplacian of the pressure on the right-hand side is treated implicitly and the remaining terms are treated explicitly.

Phase Fraction Equation

The equation for the solid-phase fraction is repeated here to complete the model:

$$\frac{\partial \phi}{\partial t} + \nabla \cdot (\phi \mathbf{u}_s) = -\frac{2a^2}{9\nu_f} \nabla \cdot [f(\phi) \nabla \cdot \mathbf{S}_p] \tag{4.10}$$

where ϕ on the left-hand side is treated implicitly and the remaining terms on the right-hand side, explicitly.

Solution Algorithm

The solution algorithm for the improved SBM implementation is shown in Figure 4.2. The solution of the equation for the solid-phase fraction (Equation 4.10) was brought to the beginning of the time step so the current value of the phase fraction is used to solve the velocity and pressure equations, as is also done in the solver for the two-fluid model, described in the next section.

4.1.3 Implementation of the Multiphase Model

The starting point of the implementation of the two-fluid model is the `twoFluidsNBSuspensionFoam` OpenFOAM® solver available at `https://github.com/fmuni/twoFluidsNBSuspensionFoam`, related to the work of MUNICCHI *et al.* [16]. To develop the `twoFluidsNBSuspensionFoam` solver, these authors extended the `twoPhaseEulerFoam` solver available on OpenFOAM's® library to include the effects of the anisotropic stress tensor into the dispersed-phase equations. The implementation also features the face-based formulation of the momentum equations which is used in this work. Even though there is little documentation available on the face-based formulation, the main steps of the implementation are illustrated in the remainder of this section. The resulting solver is referred to as `tfmFoam` hereinafter. Its difference to the `twoFluidsNBSuspensionFoam` code provided by [16] is just the correction of the drag force coefficient, as mentioned in Chapter 3.

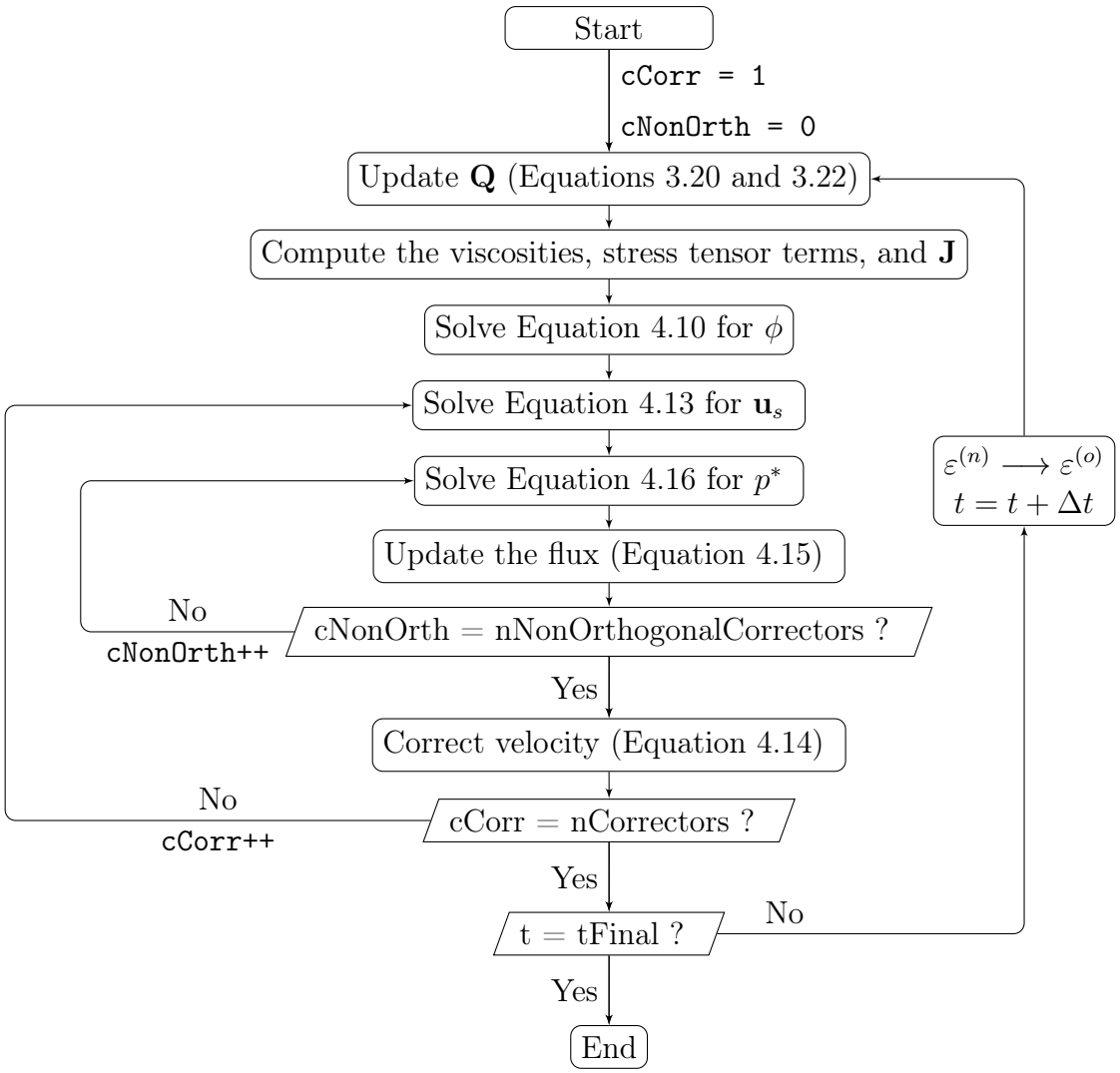

Figure 4.2: Solution algorithm for the improved SBM solver (`sbm4Foam`).

Momentum Equations

Consider both phases' momentum conservation equations (Eqs. 3.51 and 3.52), which are rewritten without the gravitational force terms, since these have been disregarded in all simulations, and in a form more suitable for the semi-discretization procedure. For the fluid phase:

$$LHS = -\left(1-\phi\right)\nabla p + \beta\left(\mathbf{u}_p - \mathbf{u}_f\right) \tag{4.17}$$

with the left-hand side given by:

$$\begin{aligned} LHS = &\frac{\partial\left[\left(1-\phi\right)\rho_f\mathbf{u}_f\right]}{\partial t} + \nabla\cdot\left[\left(1-\phi\right)\rho_f\mathbf{u}_f\mathbf{u}_f\right] - \nabla^2\left(\mu_f\mathbf{u}_f\right) \\ &- \nabla\cdot\left[\mu_f\left(\nabla\mathbf{u}_f\right)^T - \frac{2}{3}\mu_f\left(\nabla\cdot\mathbf{u}_f\right)\mathbf{I}\right] \end{aligned} \tag{4.18}$$

and for the particle phase:

$$\frac{\partial\left(\rho_p\phi\mathbf{u}_p\right)}{\partial t} + \nabla\cdot\left(\rho_p\phi\mathbf{u}_p\mathbf{u}_p\right) - \nabla\cdot\mathbf{S}_p = -\phi\nabla p - \beta\left(\mathbf{u}_p - \mathbf{u}_f\right). \tag{4.19}$$

Using the definition of the particle-phase stress tensor from Equation 3.55 and splitting the term $\nabla\cdot\left(\mu_n\dot{\gamma}\mathbf{Q}\right)$ into the two contributions proposed by MUNICCHI *et al.* [16]:

$$\nabla\cdot\left(\mu_n\dot{\gamma}\mathbf{Q}\right) = \dot{\gamma}\left(\frac{d\mu_n}{d\phi}\right)\left(\nabla\phi\right)\cdot\mathbf{Q} + \mu_n\nabla\cdot\left(\dot{\gamma}\mathbf{Q}\right) \tag{4.20}$$

the particle's momentum conservation from Equation 4.19 is written as:

$$LHS = -\phi\nabla p - \beta\left(\mathbf{u}_p - \mathbf{u}_f\right) - \dot{\gamma}\left(\frac{d\mu_n}{d\phi}\right)\left(\nabla\phi\right)\cdot\mathbf{Q} \tag{4.21}$$

where the left-hand side is given by:

$$\begin{aligned} LHS = &\frac{\partial\left(\rho_p\phi\mathbf{u}_p\right)}{\partial t} + \nabla\cdot\left(\rho_p\phi\mathbf{u}_p\mathbf{u}_p\right) - \nabla^2\left(\mu_p\mathbf{u}_p\right) \\ &- \nabla\cdot\left[\mu_p\left(\nabla\mathbf{u}_p\right)^T - \frac{2}{3}\mu_p\left(\nabla\cdot\mathbf{u}_p\right)\mathbf{I}\right] + \mu_n\nabla\cdot\left(\dot{\gamma}\mathbf{Q}\right). \end{aligned} \tag{4.22}$$

The linear systems arising from the discretization of the left-hand side of Equations 4.17 and 4.21 (which are given by Equations 4.18 and 4.22, respectively) are:

$$\mathcal{M}_i\mathbf{u}_i = \mathcal{B}_i, \qquad i = f, p \tag{4.23}$$

where $\mathcal{M}_i$ is the coefficient matrix and $\mathcal{B}_i$ is the vector of source terms. With the implicit treatment of the terms in the first lines of Equations 4.18 and 4.22, the

semi-discrete momentum conservation equations for the fluid and particle phases are, respectively:

$$\mathcal{A}_f \mathbf{u}_f = \mathcal{H}_f - (1-\phi)\nabla p + \beta(\mathbf{u}_p - \mathbf{u}_f) \tag{4.24}$$

$$\mathcal{A}_p \mathbf{u}_p = \mathcal{H}_p - \phi\nabla p - \dot{\gamma}\left(\frac{d\mu_n}{d\phi}\right)(\nabla\phi)\cdot\mathbf{Q} - \beta(\mathbf{u}_p - \mathbf{u}_f). \tag{4.25}$$

Matrices $\mathcal{A}_f$ and $\mathcal{A}_p$ are defined as the diagonal parts of $\mathcal{M}_f$ and $\mathcal{M}_p$, respectively. $\mathcal{H}_f$ and $\mathcal{H}_p$ are defined by:

$$\mathcal{H}_i = (\mathcal{A}_i - \mathcal{M}_i)\mathbf{u}_i + \mathcal{B}_i, \qquad i = f, p. \tag{4.26}$$

Then, the phase velocities read:

$$\mathbf{u}_f = \frac{\mathcal{H}_f}{\mathcal{A}_f} - \frac{1}{\mathcal{A}_f}\left[(1-\phi)\nabla p + \beta(\mathbf{u}_p - \mathbf{u}_f)\right] \tag{4.27}$$

$$\mathbf{u}_p = \frac{\mathcal{H}_p}{\mathcal{A}_p} - \frac{1}{\mathcal{A}_p}\left[\phi\nabla p - \dot{\gamma}\left(\frac{d\mu_n}{d\phi}\right)(\nabla\phi)\cdot\mathbf{Q} - \beta(\mathbf{u}_p - \mathbf{u}_f)\right]. \tag{4.28}$$

Notice that both phase momentum equations are coupled by the term that corresponds to the drag force. Using the partial elimination algorithm to deal with the momentum equations coupling [60], and rearranging the semi-discrete Equations 4.27 and 4.28 to isolate each phase velocity:

$$\mathbf{u}_f = \frac{\mathcal{H}_f}{\mathcal{A}_f + \beta} - \frac{(1-\phi)}{\mathcal{A}_f + \beta}\nabla p + \frac{\beta}{\mathcal{A}_f + \beta}\mathbf{u}_p \tag{4.29}$$

$$\mathbf{u}_p = \frac{\mathcal{H}_p}{\mathcal{A}_p + \beta} - \frac{\phi}{\mathcal{A}_p + \beta}\nabla p - \frac{\dot{\gamma}}{\mathcal{A}_p + \beta}\left(\frac{d\mu_n}{d\phi}\right)(\nabla\phi)\cdot\mathbf{Q} + \frac{\beta}{\mathcal{A}_p + \beta}\mathbf{u}_f. \tag{4.30}$$

By defining the coefficients:

$$\Lambda_f = \frac{1}{\mathcal{A}_f + \beta}, \qquad \Lambda_p = \frac{1}{\mathcal{A}_p + \beta} \tag{4.31}$$

the equations can be written as:

$$\mathbf{u}_f = \Lambda_f \mathcal{H}_f - \Lambda_f(1-\phi)\nabla p + \Lambda_f \beta \mathbf{u}_p \tag{4.32}$$

$$\mathbf{u}_p = \Lambda_p \mathcal{H}_p - \Lambda_p \phi\nabla p - \Lambda_p \dot{\gamma}\left(\frac{d\mu_n}{d\phi}\right)(\nabla\phi)\cdot\mathbf{Q} + \Lambda_p \beta \mathbf{u}_f. \tag{4.33}$$

Now, introducing the expression from Equation 4.33 into Equation 4.24, we have:

$$\begin{aligned}\mathcal{A}_f \mathbf{u}_f = {} & \mathcal{H}_f - (1-\phi)\nabla p - \beta\mathbf{u}_f \\ & + \beta\Lambda_p\left[\mathcal{H}_p - \phi\nabla p - \dot{\gamma}\left(\frac{d\mu_n}{d\phi}\right)(\nabla\phi)\cdot\mathbf{Q} + \beta\mathbf{u}_f\right].\end{aligned} \tag{4.34}$$

Introducing $\mathbf{u}_f$ from Equation 4.32 into Equation 4.25, we get:

$$\begin{aligned}\mathcal{A}_p\mathbf{u}_p = \mathcal{H}_p - \phi\nabla p - \dot{\gamma}\left(\frac{d\mu_n}{d\phi}\right)(\nabla\phi)\cdot\mathbf{Q} - \beta\mathbf{u}_p \\ + \beta\Lambda_f\left[\mathcal{H}_f - (1-\phi)\nabla p + \beta\mathbf{u}_p\right].\end{aligned} \tag{4.35}$$

To rearrange the last two equations and isolate $\mathbf{u}_f$ and $\mathbf{u}_p$, new coefficients are defined:

$$\xi_f = \frac{1}{\mathcal{A}_f + \beta - \beta^2\Lambda_p}, \qquad \xi_p = \frac{1}{\mathcal{A}_p + \beta - \beta^2\Lambda_f}. \tag{4.36}$$

Thus, using these coefficients, Equations 4.34 and 4.35 reduce to:

$$\mathbf{u}_f = \xi_f\left\{\mathcal{H}_f + \Lambda_p\beta\mathcal{H}_p - \left[(1-\phi) + \Lambda_p\beta\phi\right]\nabla p - \Lambda_p\dot{\gamma}\left(\frac{d\mu_n}{d\phi}\right)(\nabla\phi)\cdot\mathbf{Q}\right\} \tag{4.37}$$

$$\mathbf{u}_p = \xi_p\left\{\mathcal{H}_p + \beta\Lambda_f\mathcal{H}_f - \left[\phi + (1-\phi)\,\beta\Lambda_f\right]\nabla p - \dot{\gamma}\left(\frac{d\mu_n}{d\phi}\right)(\nabla\phi)\cdot\mathbf{Q}\right\}. \tag{4.38}$$

Volumetric Fluxes

Applying the definition given by Equation 4.6, the volumetric fluxes of both phases are determined by:

$$\begin{aligned}\varphi_f = \xi_f\Bigg\{\left(\mathcal{H}_f + \Lambda_p\beta\mathcal{H}_p\right)_{cf} - \left[\Lambda_p\dot{\gamma}\left(\frac{d\mu_n}{d\phi}\right)(\nabla\phi)\cdot\mathbf{Q}\right]_{cf} \\ - \left[(1-\phi) + \Lambda_p\beta\phi\right]_{cf}(\nabla p)_{cf}\Bigg\}\cdot\mathbf{A}_{cf}\end{aligned} \tag{4.39}$$

$$\begin{aligned}\varphi_p = \xi_p\Bigg\{\left(\mathcal{H}_p + \beta\Lambda_f\mathcal{H}_f\right)_{cf} - \left[\dot{\gamma}\left(\frac{d\mu_n}{d\phi}\right)(\nabla\phi)\cdot\mathbf{Q}\right]_{cf} \\ - \left[\phi + (1-\phi)\,\beta\Lambda_f\right]_{cf}(\nabla p)_{cf}\Bigg\}\cdot\mathbf{A}_{cf}.\end{aligned} \tag{4.40}$$

Pressure Equation

For an incompressible suspension, the finite volume method requires the divergence of the total volumetric flux in each cell to be zero (Equation 4.8). In terms of the individual phases' fluxes, Equation 4.8 can be written as:

$$\nabla\cdot\varphi_s = \nabla\cdot\left[\phi\varphi_p + (1-\phi)\,\varphi_f\right] = 0. \tag{4.41}$$

To simplify Equations 4.39 and 4.40, the terms on the right-hand side of their

first lines are grouped into φ_f^0 and φ_p^0:

$$\varphi_f^0 = \xi_f \left\{ \left(\mathcal{H}_f + \Lambda_p \beta \mathcal{H}_p\right)_{cf} - \left[\Lambda_p \dot{\gamma} \left(\frac{d\mu_n}{d\phi}\right) (\nabla\phi) \cdot \mathbf{Q}\right]_{cf} \right\} \cdot \mathbf{A}_{cf} \tag{4.42}$$

$$\varphi_p^0 = \xi_p \left\{ \left(\mathcal{H}_p + \beta \Lambda_f \mathcal{H}_f\right)_{cf} - \left[\dot{\gamma} \left(\frac{d\mu_n}{d\phi}\right) (\nabla\phi) \cdot \mathbf{Q}\right]_{cf} \right\} \cdot \mathbf{A}_{cf}. \tag{4.43}$$

Then, Equations 4.39 and 4.40 are rewritten as:

$$\varphi_f = \varphi_f^0 - \xi_f \left[(1-\phi) + \Lambda_p \beta \phi\right]_{cf} (\nabla p)_{cf} \cdot \mathbf{A}_{cf} \tag{4.44}$$

$$\varphi_p = \varphi_p^0 - \xi_p \left[\phi + (1-\phi)\,\beta\Lambda_f\right]_{cf} (\nabla p)_{cf} \cdot \mathbf{A}_{cf}. \tag{4.45}$$

Introducing the phases' fluxes expressions from Equations 4.44 and 4.45 into Equation 4.41, we obtain:

$$\begin{aligned} \nabla \cdot \left[\phi\varphi_p^0 + (1-\phi)\,\varphi_f^0\right] = \nabla \cdot \Big\{ & \phi\xi_p \left[\phi + (1-\phi)\,\beta\Lambda_f\right]_{cf} (\nabla p)_{cf} \cdot \mathbf{A}_{cf} \\ & + (1-\phi)\,\xi_f \left[(1-\phi) + \Lambda_p\beta\phi\right]_{cf} (\nabla p)_{cf} \cdot \mathbf{A}_{cf} \Big\}. \end{aligned} \tag{4.46}$$

Rearranging the last expression, the Poisson equation for the pressure is obtained:

$$\begin{aligned} \nabla \cdot \left[\phi\varphi_p^0 + (1-\phi)\,\varphi_f^0\right] = \nabla \cdot \Big\{ & \Big[\phi\xi_p \left(\phi + \beta\Lambda_f - \phi\beta\Lambda_f\right)_{cf} \\ & + \xi_f (1-\phi)\left(1 - \phi + \Lambda_p\beta\phi\right)_{cf}\Big] (\nabla p)_{cf} \cdot \mathbf{A}_{cf} \Big\}. \end{aligned} \tag{4.47}$$

Phase Fraction Equation

As seen before, the particle-phase continuity equation is given by:

$$\frac{\partial\left(\rho_p\phi\right)}{\partial t} + \nabla \cdot \left(\rho_p \phi \mathbf{u}_p\right) = 0 \tag{3.5}$$

which can be written in terms of the volumetric flux at the cell faces as:

$$\frac{\partial\left(\rho_p\phi\right)}{\partial t} + \nabla \cdot \Big[\left(\rho_p\phi\right)_{cf} \varphi_p\Big] = 0. \tag{4.48}$$

Equation 4.40 can be rewritten as:

$$\varphi_p = \varphi_p^* - \xi_p \left[\dot{\gamma} \left(\frac{d\mu_n}{d\phi}\right) (\nabla\phi) \cdot \mathbf{Q}\right]_{cf} \cdot \mathbf{A}_{cf} \tag{4.49}$$

where

$$\varphi_p^* = \xi_p \left\{ \left(\mathcal{H}_p + \beta\Lambda_f\mathcal{H}_f\right)_{cf} - \left[\phi + (1-\phi)\,\beta\Lambda_f\right]_{cf} (\nabla p)_{cf} \right\} \cdot \mathbf{A}_{cf}. \tag{4.50}$$

Using Equation 4.49, we can write Equation 4.48 in the following form:

$$\frac{\partial\left(\rho_p\phi\right)}{\partial t} + \nabla\cdot\left[\left(\rho_p\phi\right)_{cf}\varphi_p^*\right] = \nabla\cdot\left\{\left(\rho_p\phi\right)_{cf}\xi_p\left[\dot{\gamma}\left(\frac{d\mu_n}{d\phi}\right)\left(\nabla\phi\right)\cdot\mathbf{Q}\right]_{cf}\cdot\mathbf{A}_{cf}\right\}. \quad (4.51)$$

Evaluating the term on the right-hand side of the last equation explicitly can cause instabilities, especially when the solid-phase fraction approaches maximum packing and $d\mu_n/d\phi$ increases. MUNICCHI *et al.* [16] proposed a splitting of the anisotropic tensor into two contributions:

$$\mathbf{Q} = tr\left(\mathbf{Q}\right)\mathbf{I} + \mathbf{Q}_{dev} \quad (4.52)$$

where

$$\mathbf{Q}_{dev} = \mathbf{Q} - tr\left(\mathbf{Q}\right)\mathbf{I}. \quad (4.53)$$

Replacing the expression from Equation 4.52 into Equation 4.51, its right-hand side becomes:

$$\begin{aligned} RHS = \nabla\cdot\Bigg\{&\left(\rho_p\phi\right)_{cf}\xi_p\left[\dot{\gamma}\left(\frac{d\mu_n}{d\phi}\right)\left(\nabla\phi\right)tr\left(\mathbf{Q}\right)\right]_{cf}\cdot\mathbf{A}_{cf} \\ &+\left(\rho_p\phi\right)_{cf}\xi_p\left[\dot{\gamma}\left(\frac{d\mu_n}{d\phi}\right)\left(\nabla\phi\right)\cdot\mathbf{Q}_{dev}\right]_{cf}\cdot\mathbf{A}_{cf}\Bigg\}. \end{aligned} \quad (4.54)$$

in which ϕ from the first term on the right-hand side of Equation 4.54 is evaluated implicitly, and the last term explicitly. Both formulations, with this implicit treatment of the term in Equation 4.54 or the explicit treatment of the right-hand side of Equation 4.51 are implemented in the `tfmFoam` solver and the user can choose at the beginning of the simulation which one will be used. MUNICCHI *et al.* [16] recommended the usage of the explicit formulation to preserve the hyperbolicity of the equation unless severe stability issues are being faced. Notice that the value of $\nabla\phi$ is always needed to solve this equation, for both formulations. Therefore, its value shall be specified as a boundary condition for ϕ. When using the implicit formulation, the values of $\nabla\phi$ contribute to the diagonal coefficients of the discretization matrix, posing a stronger dependence of the solution on its value and on its respective boundary condition.

Solution Algorithm

The model is solved using the PIMPLE algorithm for pressure-velocity coupling. Equations are solved sequentially according to the algorithm described in Figure 4.3.

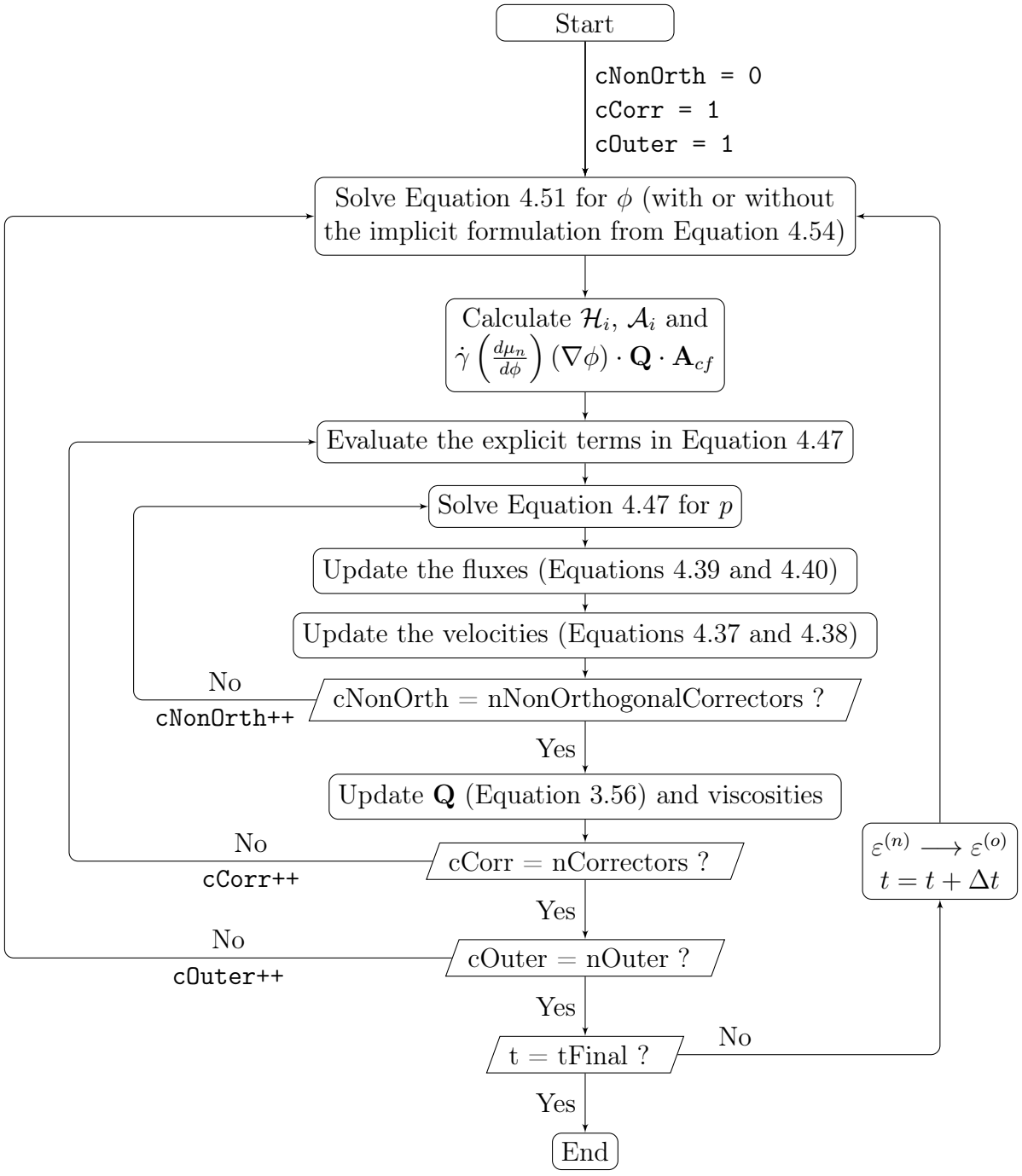

Figure 4.3: Solution algorithm for the two-fluid solver (`tfmFoam`).

4.1.4 Calculation of the Torque

To calculate the torque applied to the inner cylinder for the Couette flow throughout the simulations, applications compatible with each model were implemented, which compute the torque components. For a given surface S with area A, the application calculates the relative distance to the center of rotation (represented by the position vector $\mathbf{r}$) and applies the torque definition:

$$\mathbf{T} = \int_S \mathbf{r} \times (\hat{\mathbf{n}} \cdot \mathbf{S}_s)\, dA. \tag{4.55}$$

4.2 Grid Convergence Analysis

For each studied geometry, hexahedral structured meshes were generated using OpenFOAM's® `blockMesh` utility. To ensure that mesh-independent results were obtained, simulations using both models are performed for three meshes with different refinements: the coarsest mesh is identified with subscript $m1$, the intermediate with $m2$, and the finest with $m3$. The method described in CELIK *et al.* [61] was used to estimate the observed order of accuracy, which is used to determine the error and uncertainty due to spatial discretization following PHILLIPS and ROY [62].

A representative grid spacing h is defined for a generic two-dimensional mesh by:

$$h_i = \left[\frac{1}{N} \sum_{j=1}^{N} A_j \right]^{\frac{1}{2}}, \qquad i = m1, m2, m3 \tag{4.56}$$

where N is the total number of cells of the given mesh and A_j is the area of the jth cell. Hence, $h_{m1} > h_{m2} > h_{m3}$. The refinement ratio between two consecutive meshes is defined as a function of the grid spacing:

$$r_{12} = \frac{h_{m1}}{h_{m2}}, \qquad r_{23} = \frac{h_{m2}}{h_{m3}}. \tag{4.57}$$

For a generic variable field ε, the observed order of accuracy $\hat{p}$ can be calculated by:

$$\hat{p} = \frac{1}{ln(r_{23})} \left| ln \left| \frac{\varepsilon_{m1} - \varepsilon_{m2}}{\varepsilon_{m2} - \varepsilon_{m3}} \right| + g(\hat{p}) \right| \tag{4.58}$$

where

$$g(\hat{p}) = ln \left[\frac{r_{23}^{\hat{p}} - s(\varepsilon)}{r_{12}^{\hat{p}} - s(\varepsilon)} \right] \tag{4.59}$$

and

$$s(\varepsilon) = sign\left(\frac{\varepsilon_{m1} - \varepsilon_{m2}}{\varepsilon_{m2} - \varepsilon_{m3}}\right). \tag{4.60}$$

The order of accuracy is calculated pointwise along a radial line for the Couette flow and along a vertical line for the channel flow. Equations 4.58 to 4.60 are solved iteratively according to the following algorithm:

$\hat{p}^{(o)} = 2$
$res = 1$
while $res < 10^{-8}$ **do**
    Calculate s (Equation 4.60)
    Calculate $g(\hat{p}^{(o)})$ (Equation 4.59)
    Calculate $\hat{p}^{(n)}$ using $g(\hat{p}^{(o)})$ (Equation 4.58)
    res $= \hat{p}^{(n)} - \hat{p}^{(o)}$
    $\hat{p}^{(n)} = \frac{\hat{p}^{(n)} + \hat{p}^{(o)}}{2}$
end

To determine the global order of accuracy on a given mesh following PHILLIPS and ROY [62], each value of the observed order of accuracy is limited between 0.05 and the formal order of the numerical scheme used. The chosen discretization methods are further described in Section 4.4 and are formally of second order. Hence:

$$\hat{p}_{OR} = \min\left(\max\left(0.05, \hat{p}\right), \hat{p}_{formal}\right), \qquad \hat{p}_{formal} = 2. \tag{4.61}$$

Then, the global order of accuracy $\hat{p}_{glb}$ is taken as the average of $\hat{p}_{OR}$ along the line. After determining the global order of accuracy, the relative error (E) and uncertainty (U) on the determination of ε on meshes $m2$ and $m3$ are estimated by, respectively:

$$E_{m3}(\hat{p}_{glb}) = \left|\frac{\varepsilon_{m3} - \varepsilon_{m2}}{\varepsilon_{m3}\left(r_{23}^{\hat{p}_{glb}} - 1\right)}\right|, \qquad E_{m2}(\hat{p}_{glb}) = \left|\frac{\varepsilon_{m2} - \varepsilon_{m1}}{\varepsilon_{m2}\left(r_{12}^{\hat{p}_{glb}} - 1\right)}\right| \tag{4.62}$$

$$U_i = 1.25E_i, \qquad i = m2, m3. \tag{4.63}$$

Table 4.1: Description of the Couette geometries.

Geometry	R_i (cm)	R_o (cm)	l (cm)	R_i/l
A	0.64	2.38	1.74	0.368
B	1.28	3.02	1.74	0.736
C	1.28	4.76	3.48	0.368

4.3 Studied Cases

4.3.1 Couette Rheometer

The described solvers are used to simulate the suspension flow in a wide-gap Couette cell, as shown in Figure 3.2 (repeated below). The experimental study of PHILLIPS *et al.* [3] is reproduced, with a suspension of polymethyl methacrylate (PMMA) particles with radius $a = 337.5\ \mu m$ and density $\rho_p = 1182\ kg/m^3$ dispersed in a Newtonian oil. The oil viscosity is $\mu_f = 9.45\ Pa.s$ and the density is adjusted to match those of the particles. The suspension fills the gap between the two concentric cylinders of radii $R_i = 0.64\ cm$ and $R_o = 2.38\ cm$, the outer cylinder being stationary and the inner cylinder rotating with an angular velocity varying from 0.5 to 48 rps. The simulations start from a homogeneous suspension with a bulk solid-phase fraction of $\phi_b = 0.55$, and particles migrate as the inner cylinder starts spinning. Once the solid-phase fraction and torque at the inner cylinder reach the steady state, the simulation is stopped.

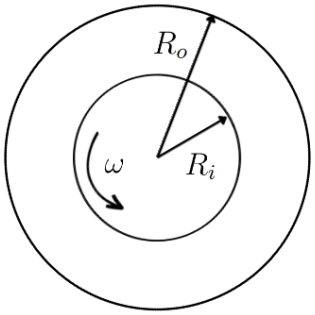

Figure 3.2: Couette rheometer geometry used to obtain the analytical solution for a power-law fluid.

Additionally, the flow of the same suspension was also simulated in other Couette geometries with different values of cylinder radii and gap size (l), as shown in Table 4.1, with A corresponding to the same geometry of the experimental study of PHILLIPS *et al.* [3]. The inner cylinder radius of geometry B is twice the one from geometry A, and the outer cylinder radius was adjusted so they present the same gap size. In geometry C, both cylinder radii and the gap size are twice the ones of geometry A.

Figure 4.4: Intermediate one-dimensional mesh ($m2$) created to test the frame-dependent solvers.

Table 4.2: Description of the one-dimensional created meshes for the Couette case.

Mesh ID	N
CT-A-m1-w	20
CT-A-m2-w	28
CT-A-m3-w	40

Mesh Generation

Since solvers `sbm1Foam` and `sbm2Foam` are frame-dependent, a set of one-dimensional meshes was generated, as exemplified in Figure 4.4. Then, the unit vectors $\hat{\mathbf{e}}_1$ and $\hat{\mathbf{e}}_2$ coincide with $\hat{\mathbf{e}}_y$ and $\hat{\mathbf{e}}_x$, respectively. All the one-dimensional meshes were created with a cell opening of 1^o and are listed in Table 4.2. The grid convergence analysis was performed with the results obtained using solver `sbm1Foam` and a rotating velocity of the inner cylinder of 1 rps.

For the Couette flow in geometry A in two dimensions, two sets of grids were created: the first set of three meshes with uniform refinement in both radial and angular directions, and a second set of three meshes with non-uniform refinement in the radial direction, with increased grading in the regions close to the boundaries. Figure 4.5 shows a 90-degree section of the intermediate meshes of both sets, being the grids symmetric with respect to the angular direction. Since increasing the refinement close to the outer cylinder also increases the mesh skewness, a higher number of divisions in the angular direction had to be used for the non-uniform mesh when compared to the respective uniform grid. For the non-uniform grids, the grid convergence analysis was carried out using the results from simulations with both `sbm4Foam` and `tfmFoam`, with a rotating velocity of the inner cylinder of 4 rps. For the uniform grid, the procedure was applied only using solver `sbm4Foam` and the same cylinder rotation. For geometries B and C, one set of uniformly refined meshes was created and the grid convergence analysis performed only using the `sbm4Foam` solver with inner cylinder rotation of 16 rps. All of the two-dimensional generated grids for the Couette flow study are identified in Table 4.3, with n_r and n_θ representing the number of divisions in the radial and angular directions, respectively, resulting in a total of N cells for each grid. The maximum observed values for the non-orthogonality and skewness in each mesh are also reported in Table 4.3

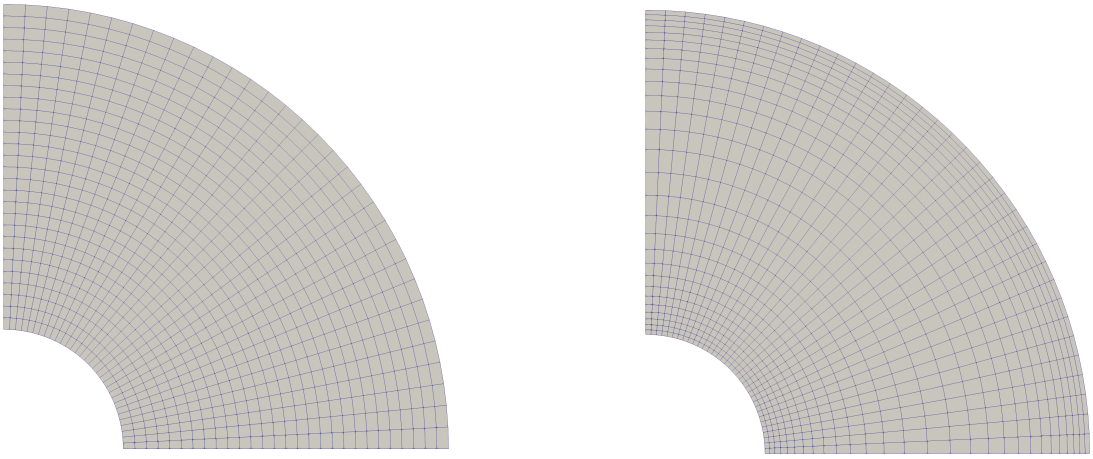

(a) (b)

Figure 4.5: Intermediate $m2$ meshes of the Couette geometry A used for the grid convergence analysis with (a) constant refinement on the radial direction and (b) grading close to the cylinder boundaries.

Table 4.3: Description of the two-dimensional meshes created for the Couette flows.

Mesh ID[1]	Geometry	n_r	n_θ	N	Maximum non-orthogonality	Maximum skewness
CT-A-m1-u	A	20	92	1840	6.81×10^{-5}	0.056
CT-A-m2-u	A	28	128	3584	6.89×10^{-5}	0.041
CT-A-m3-u	A	40	180	7200	6.93×10^{-5}	0.030
CT-A-m1-nu	A	20	100	2000	6.84×10^{-5}	0.077
CT-A-m2-nu	A	28	140	3290	6.90×10^{-5}	0.055
CT-A-m3-nu	A	40	200	8000	7.09×10^{-5}	0.039
CT-B-m1-u	B	28	128	3584	1.55×10^{-4}	0.054
CT-B-m2-u	B	40	180	7200	1.57×10^{-4}	0.040
CT-B-m3-u	B	56	256	14336	1.58×10^{-4}	0.027
CT-C-m1-u	C	40	180	7200	6.90×10^{-5}	0.030
CT-C-m2-u	C	56	256	14336	6.95×10^{-5}	0.021
CT-C-m3-u	C	80	360	28800	6.99×10^{-5}	0.015

[1] The identifiers *-u* and *-nu* at the end of the mesh ID indicate a uniformly or non-uniformly refined mesh, respectively.

Table 4.4: Description of the linear channel geometries.

Geometry	$H\ (m)$	d/H	$L\ (m)$	L_{min}
A	0.004	0.169	12	0.13
B	0.008	0.084	24	1.03
C	0.01	0.068	36	2.00
D	0.02	0.034	36	16.02

4.3.2 Linear Channel

The flow of the same suspension considered for the Couette rheometer simulations (described in Section 4.3.1) is simulated in four different straight channel geometries, outlined in Table 4.4, with mean velocities $\overline{u} = 0.02,\ 0.2$ and $2\ m/s$. Combinations of the mean velocity and channel width are chosen to achieve values of shear rate in the same range obtained in the Couette flow simulations. The minimum length of the channel necessary to achieve a fully-developed flow is estimated following NOTT and BRADY [13]:

$$L_{min} \approx \frac{H}{24d(\phi_b)} \left(\frac{H}{a}\right)^2 \tag{4.64}$$

where $d(\phi_b)$ represents the dependence of the shear-induced diffusion on the bulk solid-phase fraction, given by [15]:

$$d(\phi_b) = \frac{1}{3}\phi_b^2 \left(1 + \frac{1}{2}e^{8.8\phi_b}\right). \tag{4.65}$$

Since it is an estimate and it may take several transition lengths to achieve the fully-developed flow [13], the calculated values of L_{min} were used only as a guideline. The actual lengths of the channels were chosen to be over one order of magnitude greater than the minimum length to ensure that the developed state is achieved, with an exception for geometry D, in which $L \approx 2L_{min}$, due to a large number of cells necessary for the computational grid.

Mesh Generation

For the 2-D channel, only one set of three grids was created for each geometry. Since the meshes are orthogonal and with no skewness, no refinement was applied to the regions close to the boundaries. All generated meshes for the 2-D channel simulations are described in Table 4.5, in which n_x and n_y stand for the number of divisions in the flow and transversal directions, respectively, and N the total number of grid cells. The grid convergence analysis was performed for each geometry using the results of simulations with the mean suspension velocity of $\overline{u} = 2\ m/s$.

Table 4.5: Description of all meshes generated for the 2-D channel flows.

Mesh ID	L (m)	H (m)	n_x	n_y	N
LC-m1-A	12	0.004	240	8	1920
LC-m2-A	12	0.004	360	12	4320
LC-m3-A	12	0.004	480	16	7680
LC-m1-B	24	0.008	480	16	7680
LC-m2-B	24	0.008	720	24	17280
LC-m3-B	24	0.008	960	32	30720
LC-m1-C	36	0.01	720	20	14400
LC-m2-C	36	0.01	1080	30	32400
LC-m3-C	36	0.01	1440	40	57600
LC-m1-D	36	0.02	720	40	28800
LC-m2-D	36	0.02	1080	60	64800
LC-m3-D	36	0.02	1440	80	115200

Table 4.6: Discretization schemes used with both models (entries of the `fvSchemes` dictionary).

	Setup I	Setup II
Gradient	Linear	Skew Corrected Linear
Surface Normal Gradient	Corrected	Corrected
Laplacian	Linear Corrected	Linear Corrected
Divergent (default)	Linear	Skew Corrected Linear
$\nabla \cdot (\varphi \mathbf{u})$	Limited Linear 1	Skew Corrected Limited Linear 1
$\nabla \cdot (\varphi \phi)$	Limited Linear 1	Skew Corrected Limited Linear 1
Interpolation	Linear	Skew Corrected Linear
d/dt	Euler	Euler

4.4 Numerical Setup

The equations presented in Section 4.1 are discretized following the schemes presented in Table 4.6, given in the `fvSchemes` dictionary. The *limited linear 1* scheme includes a limiter between the upwind scheme (in regions with high gradient variations) and the linear scheme, for which the coefficient value equal to 1 imposes the strongest limiting. For both models, two sets of numerical schemes were tested: setup I, without any correction for skewness, and setup II, which applies the skewness correction for the non-orthogonal mesh of the Couette flow in the cylindrical geometry. Since there is no skewness on the 2-D channel grids, setup I was used for all simulations of this flow. Detailed information on each of the discretization methods listed in Table 4.6 can be found in the literature [59, 63].

In OpenFOAM®, the description of the numerical methods used to solve the linear systems that arise from the discretization of the transport equations is given in the `fvSolution` dictionary. At the beginning of the solution of a given linear system, the initial residual is calculated as the normalized absolute difference between the left

Table 4.7: Numerical methods used to solve the linear systems (entries of the `fvSolutions` dictionary), their absolute and relative tolerances.

	ϕ	$p\ (Pa),\ p^*\ (m^2/s^2)$	$\mathbf{u}_s\ (m/s)$
Linear solver	PBiCG	PCG	PCG
Pre-conditioner	DILU	DIC	DIC
Absolute tolerance	10^{-9}	10^{-10}	10^{-9}
Relative tolerance	0	0.01	0.01
Final relative tolerance[1]	-	0	0

[1] Relative tolerance for the final non-orthogonal correction

and right-hand sides of the equation. Then, the linear system is solved iteratively until either the absolute residual falls below the specified tolerance or until the ratio between the current and the initial residuals falls below the specified relative tolerance [64]. The Preconditioned Bi-Conjugate Gradient method (PBiCG) was chosen to solve the system for the solid-phase fraction, and the Preconditioned Conjugate Gradient method (PCG) for the pressure and the suspension velocity when using the SBM. Since the `tfmFoam` solver does not solve linear systems for $\mathbf{u}_f$ and $\mathbf{u}_p$, it does not require the specification of a linear solver for these variables. The key idea of the PBiCG and PCG methods is to transform the solution of the linear system into a minimization problem, which is solved iteratively until the given convergence criteria are satisfied. To increase the convergence rate, the coefficient matrix is approximated by a new matrix that shall be easily invertible and with a smaller condition number (ratio between its maximum and minimum eigenvalues) in a process called pre-conditioning [65]. For the solid-phase fraction, the Diagonal ILU factorization (DILU) was used in the pre-conditioning, and for the pressure and suspension velocity, the Diagonal Incomplete Cholesky factorization (DIC). More details about those numerical methods and the aforementioned pre-conditioners can be found in the literature [63, 65]. Once the initial residuals for the solution of all linear systems already satisfy the convergence criteria, the steady state has been achieved. Then, simulations are stopped and their results are analyzed. A summary of the methods used for all simulations and their convergence criteria are listed in Table 4.7.

To evaluate the methods proposed by MUNICCHI *et al.* [16] for solving the solid-phase fraction equation, as presented in Section 4.1, both implicit and explicit treatments of the terms associated with the particle-phase normal stress divergence were tested. From now on, setups using the implicit formulation of Equation 4.54 will be referred to as setup A, and those using the explicit formulation given by Equation 4.51 as setup B. For instance, simulations with the two-fluid model using skewness correction in the discretization schemes and the implicit formulation for the solid-phase fraction equation are identified as setup II-A. The implicit formulation is

Table 4.8: Initial and boundary conditions used for the 2-D channel flow simulations.

	ϕ	$\mathbf{u}_i$ (m/s)	p (Pa)
Initial Condition	0.55	$\overline{u}$	0
Inlet	0.55	$\overline{u}$	Zero gradient
Outlet	Zero gradient	Zero gradient	0
Walls	Zero gradient	No slip	Zero gradient

Table 4.9: Initial and boundary conditions used for the Couette flow simulations.

	ϕ	$\mathbf{u}_i$ (m/s)	p (Pa), p^* (m^2/s^2)
Initial Condition	0.55	0	0
Outer Cylinder	Zero gradient	No slip	Zero gradient
Inner Cylinder	Zero gradient	ωR_i	Zero gradient

only available for the two-fluid model: the suspension balance model always treats the normal stress divergence explicitly and, therefore, its simulations always used the setup B.

The initial and boundary conditions for each variable the model solves for are given in the dictionaries stored in directory `0`. They are listed in Tables 4.8 and 4.9 for the Couette flows and 2-D channel flows, respectively. Additionally, for the Couette flow simulations using the one-dimensional meshes, the OpenFOAM's® `wedge` boundary condition for axy-symmetric problems was applied at the θ-normal surfaces.

Chapter 5

Results and Discussion

5.1 Grid Convergence Analysis

The procedure for the grid convergence analysis (described in Section 4.2) was applied for all created geometries. The estimated uncertainty in the calculation of the solid-phase fraction for the intermediate grids for each study is presented in Table 5.1, along with the observed order of accuracy. Convergence results on the intermediate grids were considered satisfactory. Thus, the other studies were performed using the intermediate meshes.

Table 5.1: Results of the grid convergence analysis in the determination of the solid-phase fraction field on the intermediate grids.

Geometry	Solver	Uncertainty	Order of accuracy
Couette A (1-D)	`sbm1Foam`	0.46%	1.87
Couette A (2-D, uniform refinement)	`sbm4Foam`	0.43%	1.68
Couette A (2-D, non-uniform refinement)	`sbm4Foam`	0.54%	1.85
Couette A (2-D, non-uniform refinement)	`tfmFoam`	0.73%	1.69
Couette B	`sbm4Foam`	0.15%	1.72
Couette C	`sbm4Foam`	0.23%	1.68
Linear Channel A	`tfmFoam`	0.96%	2.00
Linear Channel B	`tfmFoam`	0.34%	1.54
Linear Channel C	`tfmFoam`	0.17%	1.56
Linear Channel D	`tfmFoam`	0.11%	1.94

Additionally, the grid convergence analysis was also applied to estimate the uncertainty in the calculation of the torque at the inner cylinder for the Couette flows. The uncertainties estimated for the intermediate grids and the observed order of accuracy are shown in Table 5.2. The determined values for the uncertainty are further used in the estimation of the rheological parameters.

Table 5.2: Result of the grid convergence analysis in the determination of the torque on the inner cylinder for the Couette flows.

Geometry	Solver	Uncertainty	Order of accuracy
Couette A (2-D, uniform refinement)	`sbm4Foam`	2.43%	2.00
Couette A (2-D, non-uniform refinement)	`tfmFoam`	2.15%	2.00
Couette B	`sbm4Foam`	2.34%	2.00
Couette C	`sbm4Foam`	2.56%	2.00

5.2 SBM Implementation Improvement

Figure 5.1 shows the predicted dispersed-phase fraction radial profiles after 200 and 12000 revolutions of the inner cylinder for the simulations with the different SBM solvers - the radial coordinate is made dimensionless using $\zeta = (r - R_i)/(R_o - R_i)$. The experimental data of PHILLIPS *et al.* [3], acquired using the non-invasive nuclear magnetic resonance (NMR) method, are plotted for comparison. Both data sets at 200 revolutions and 12000 revolutions were obtained by averaging the results of eighth cycles of image acquisition, yielding a signal-to-noise ratio of 20 dB. Considering the signal-to-noise ratio as the minimum standard deviation in the NMR imaging process, the estimated minimum experimental error, without accounting for other sources of experimental error, was of 2%. In agreement with the information provided in the literature [3], the results presented in this work were confirmed to be at the steady state after 12000 revolutions of the inner cylinder.

As can be observed in Figure 5.1, the particles migrate towards the stationary cylinder, where the shear rate is minimum, achieving values close to the maximum packing fraction and resulting in a high viscosity region. The suspension's viscosity radial profiles calculated with the different models implemented in solvers `sbm1Foam` and `sbm2Foam` are shown in Figure 5.2 for the same instants than the dispersed-phase fraction. After 200 revolutions of the inner cylinder (Figure 5.2a) the viscosity calculated by the original solver is significantly greater than the one calculated with the MORRIS and BOULAY [14] model. At the steady state (Figure 5.2b), the viscosity calculated by the `sbm1Foam` solver diverges, as the phase fraction is close to the maximum packing fraction - the suspension viscosity equation used in this solver, $\mu_s = (1 - \phi/\phi_m)^{-2}$, is expected to present this problem since μ_s increases quadratically with the phase fraction and exhibits a singularity at $\phi = \phi_m$. The expression implemented in solver `sbm2Foam` prevents this quadratic divergence, which in turn prevents the overestimation of the solid-phase fraction at the vicinity of the outer cylinder, leading to a steady-state phase-fraction profile with better agreement with the experimental data. The particles in this specific region are close to achieving what is known as a *jammed state*, creating a non-flowing plug inside

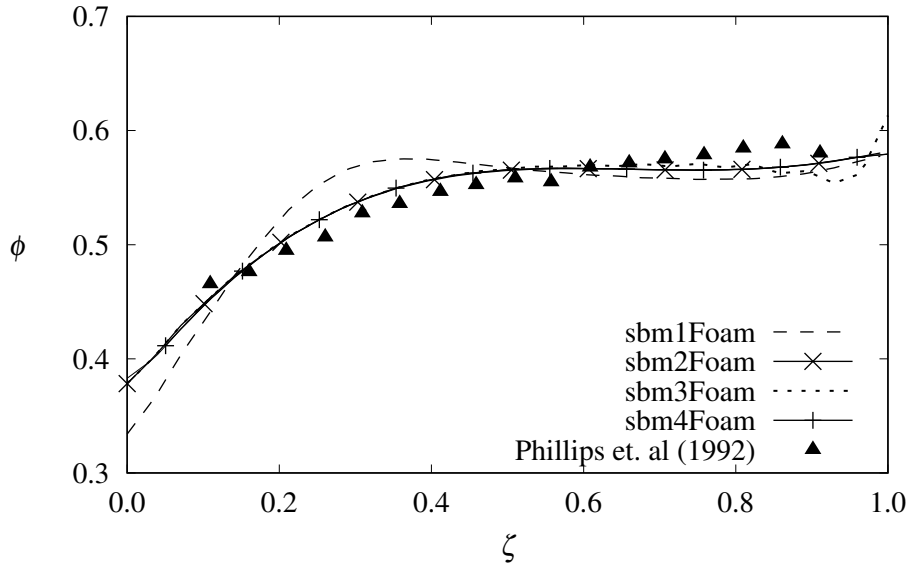

(a)

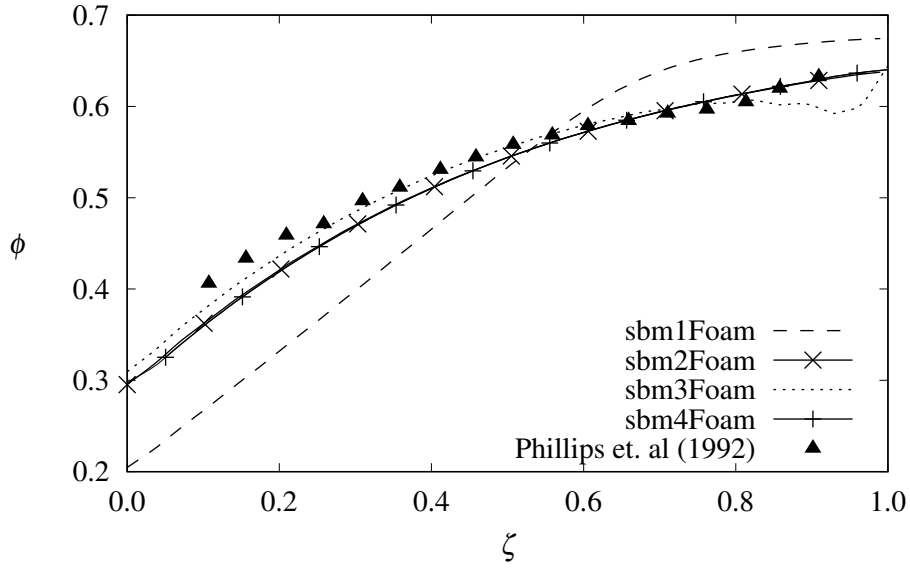

(b)

Figure 5.1: Dispersed-phase fraction radial profiles obtained with the different versions of the suspension balance model solver (`sbm1Foam`, `sbm2Foam`, `sbm3Foam`, `sbm4Foam`) and experimental data of PHILLIPS *et al.* [3] after (a) 200 revolutions and (b) 12000 revolutions of the inner cylinder.

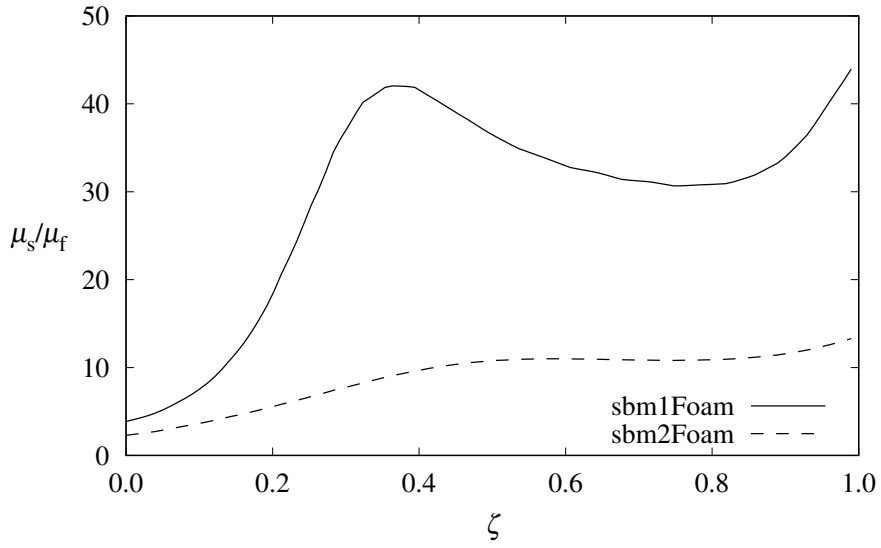

(a)

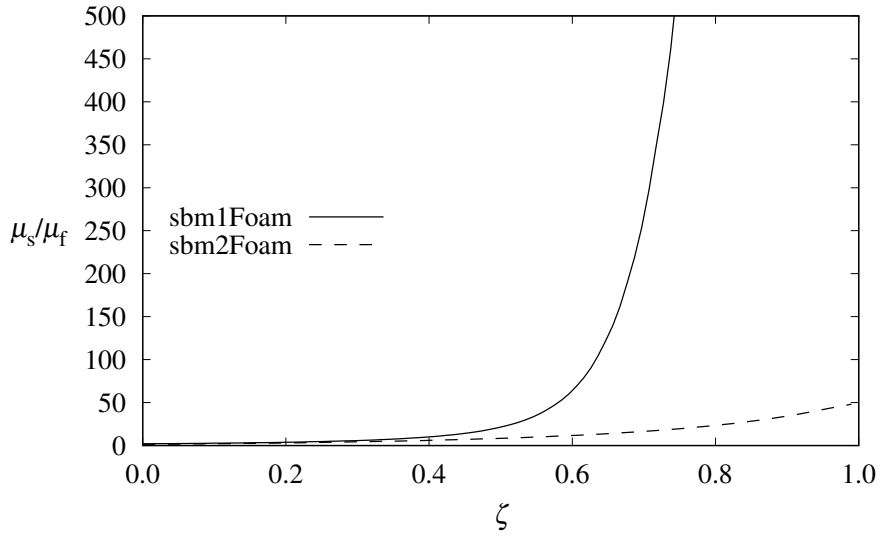

(b)

Figure 5.2: Radial profile of the suspension's shear viscosity obtained using solvers `sbm1Foam` and `sbm2Foam` after (a) 200 revolutions of the inner cylinder and (b) 12000 revolutions (steady state).

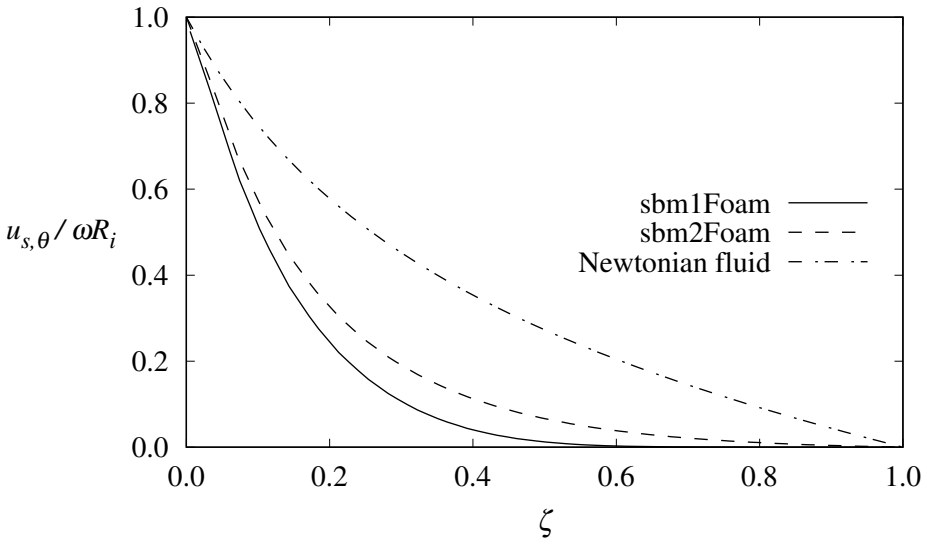

Figure 5.3: Comparison of the angular component of the suspension velocity obtained with solvers `sbm1Foam` and `sbm2Foam` at the steady state (12000 revolutions).

the rheometer [37]. Consequently, as the suspension's viscosity increases, its velocity drops to near zero, as shown in Figure 5.3. The analytical solution of the steady-state angular velocity profile for a Newtonian fluid is also plotted in Figure 5.3 for comparison. Notice that the presence of the particles and the consequent increase in viscosity poses a resistance to the suspension's motion, diminishing the velocity when compared to a pure Newtonian fluid.

Figure 5.1 also shows that the implementation of the frame-invariant formulation of the anisotropic stress in `sbm3Foam` introduces numerical oscillations in the solid-phase fraction field, especially close to the external boundary. Using the improved momentum interpolation from solver `sbm4Foam` eliminates these oscillations, providing exactly the same dispersed-phase fraction profile obtained by using solver `sbm2Foam`. This result was expected, since all the model equations are the same except for the definition of the unit vectors from the anisotropic tensor. The fact that solvers `sbm2Foam` and `sbm4Foam` predict the same solid-phase fraction profile verified the generalization of the anisotropic stress computation using the local coordinate system defined in Equation 3.21. In order to interpret the Cartesian components of tensor $\mathbf{Q}$, Table 5.3 shows their expected values based on Equation 3.25 for some limiting values of θ and their maximum and minimum values (all remaining components that are not listed in this table are null at these conditions). With $\lambda_1 = 1$ and$\lambda_2 = 0.8$, the component Q_{xx} varies between 0.8 at $y = 0$ ($\theta = 0, \pi$) and 1.0 at $x = 0$ ($\theta = \pm\pi/2$); the Q_{yy} varies between 0.8 at $x = 0$ ($\theta = \pm\pi/2$) and 1.0

Table 5.3: Expected values of the non-zero components of the anisotropic tensor **Q** on Cartesian coordinates for the Couette flow.

	Q_{xx}	$Q_{xy},\ Q_{yx}$	Q_{yy}	Q_{zz}
$\theta \to (0, \pi)^+$	λ_2	0^+	λ_1	λ_3
$\theta \to (0, \pi)^-$	λ_2	0^-	λ_1	λ_3
$\theta \to \pm(\pi/2)^+$	λ_1	0^+	λ_2	λ_3
$\theta \to \pm(\pi/2)^-$	λ_1	0^-	λ_2	λ_3
Maximum	λ_1	$(\lambda_1 - \lambda_2)/2$	λ_1	λ_3
Minimum	λ_2	$(\lambda_2 - \lambda_1)/2$	λ_2	λ_3

at $y = 0$ ($\theta = 0, \pi$); Q_{xy} varies between -0.1 and 0.1, with maximum values at $\theta = 3\pi/4$ and $-\pi/4$, and minimum values at $\pi/4$ and $-3\pi/4$. The values obtained with solver `sbm4Foam` are presented in Figure 5.4 and are shown to agree with the expected values.

5.3 Flow on a Couette Rheometer

5.3.1 Influence of the Simulation Setup

Boundary Condition

Choosing the implicit or explicit formulation for the solid-phase fraction equation with the two-fluid model has an impact on the boundary conditions applied to this equation. As mentioned before, with the implicit formulation, the gradient boundary condition specified for ϕ is more strongly imposed when compared to the explicit formulation. The steady-state solid-phase fraction profiles are shown in Figure 5.5 for both formulations of the TFM, and for the SBM with its explicit formulation. Near the inner boundary, simulations with the different models using the explicit formulation provide different values of ϕ at the wall, but with similar behavior, including its radial derivative as it approaches the inner cylinder wall. For the implicit formulation, the zero normal gradient boundary condition is seen to affect the behavior of the radial phase-fraction profile close to the inner cylinder, which visibly approaches the boundary with a null derivative. Since this boundary condition has no physical meaning for the modeled phenomena and influences the results mainly in the same region where the torque is being calculated, the explicit formulation will be used hereinafter.

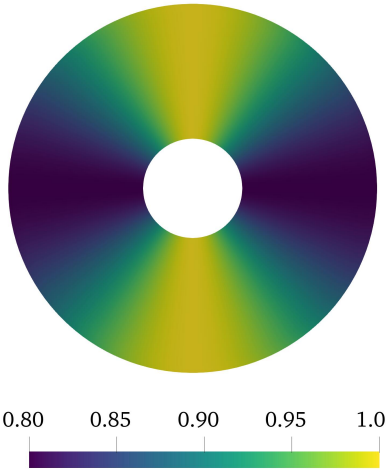

(a)

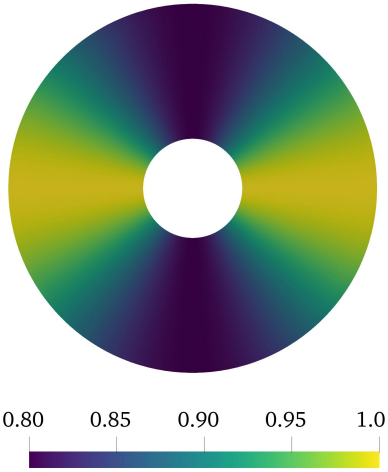

(b)

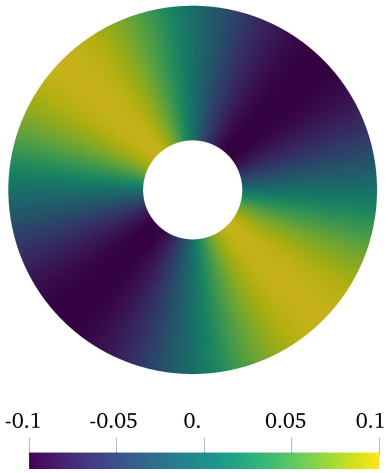

(c)

Figure 5.4: Cartesian components (a) Q_{xx}, (b) Q_{yy}, and (c) Q_{xy} of the anisotropic tensor $\mathbf{Q}$ obtained with solver `sbm4Foam` using the frame-invariant formulation.

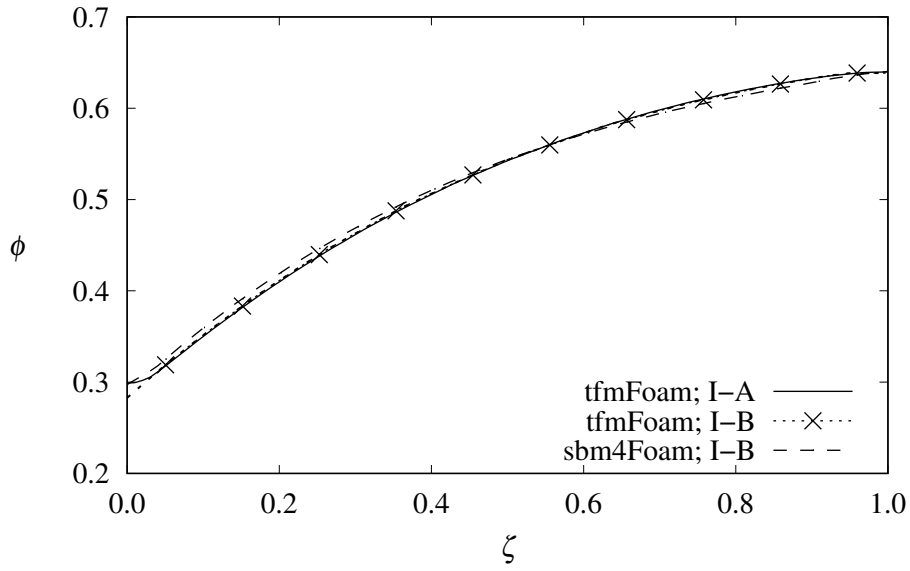

Figure 5.5: Comparison of the dispersed-phase fraction profiles obtained for the Couette flow in geometry A, using the implicit and explicit treatments of the normal stress terms in the particle's continuity equation.

Skewness Correction

To analyze the influence of mesh skewness on the results of the simulations, numerical schemes with and without skewness corrections (setups II and I, respectively) were tested on meshes with both uniform and non-uniform radial refinement, with the same rotating velocity of the inner cylinder ($\omega = 4\ rps$) and the explicit formulation for the phase-fraction equation (Equation 4.51). Figure 5.6 presents the results of these simulations with the suspension balance model. Figure 5.6-a compares the results for the grids with uniform and non-uniform refinement in the radial direction. No difference is observed in these results due to the refinement close to the boundaries. Therefore, all the next simulations with the SBM were performed using the uniform grid. Results for the simulations using setups I and II on the uniform mesh are presented in Figure 5.6-b, showing that the skewness correction did not provide any influence on them. Thus, all the next simulations with the SBM were carried out using setup I-B, without the application of the skewness correction.

The comparison of the results for simulations using the two-fluid model with both setups provides a curious result, shown in Figure 5.7. Setup I-B, without skewness correction, provided a result very similar to the one previously obtained with the suspension balance model, plotted again for comparison. However, the skewness correction used in setup II-B significantly changed the results of the dispersed-phase fraction profile near the boundary regions, with less agreement with the experimen-

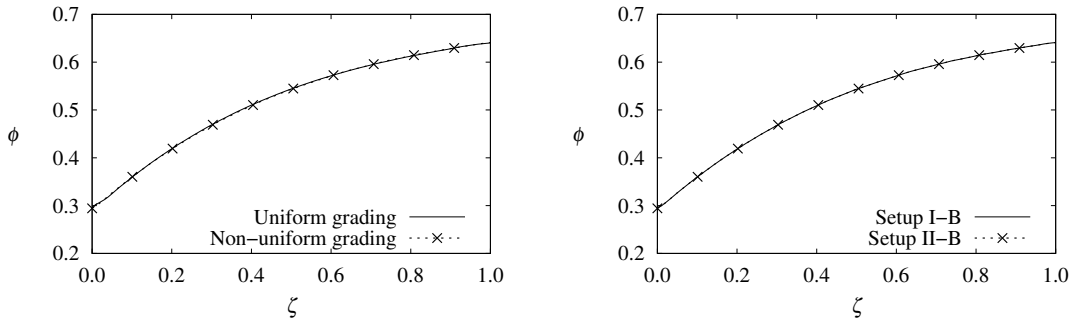

(a) (b)

Figure 5.6: Influence of (a) grading and (b) skewness correction on the steady-state solid-phase fraction profiles obtained with the suspension balance model (`sbm4Foam`) for the Couette flow in geometry A. Results in (a) used setup I-B.

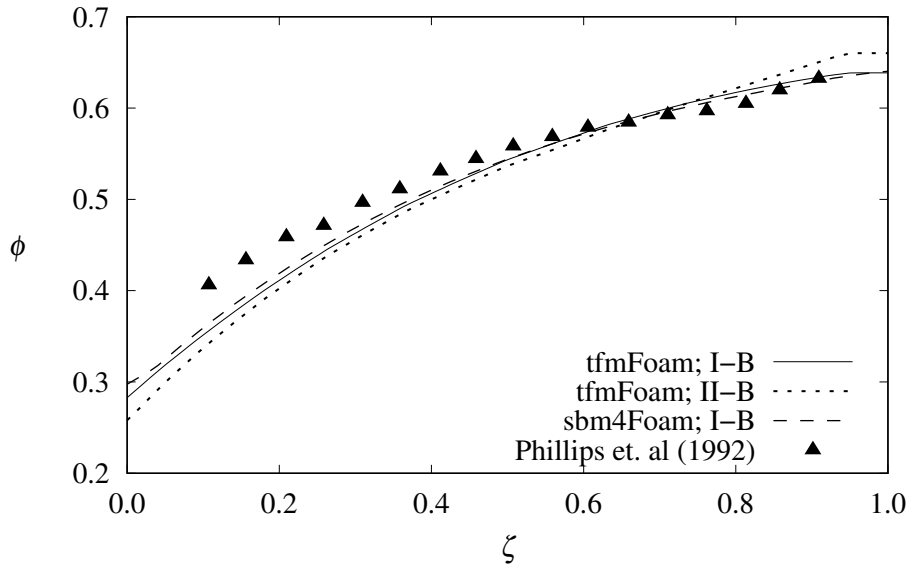

Figure 5.7: Influence of the skewness correction on the dispersed-phase fraction profiles predicted by the two-fluid model (`tfmFoam`) for the Couette flow in geometry A.

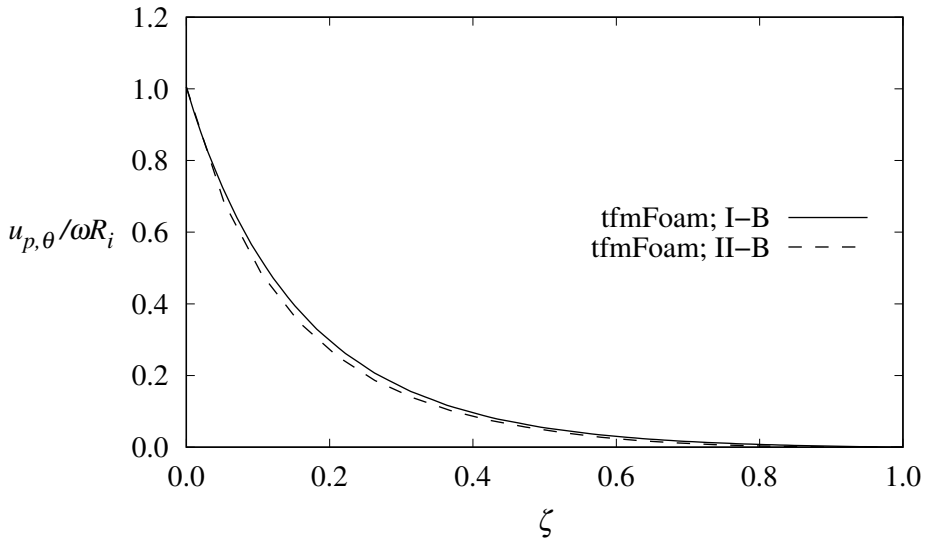

Figure 5.8: Influence of the skewness correction on the particle-phase angular velocity predicted by the two-fluid model (`tfmFoam`) for the Couette flow in geometry A.

tal data. Another change was also observed in the particle-phase angular velocity profile, as shown in Figure 5.8.

It seems that the skewness correction, when applied to multiple velocity fields, acts as a source of numerical error in the simulation. To avoid this behavior, no skewness correction was used to obtain the results presented hereinafter with any of the models. This OpenFOAM® feature needs to be more deeply investigated in order to understand the observed behavior and, perhaps, improve its implementation.

Computational Cost

The simulations with setup I-B (explicit treatment of the normal stress divergence and no skewness correction) and cylinder rotation varying from 0.5 to 48 *rps* were performed using both solvers on the three considered Couette geometries (listed in Table 4.1). The results for geometry A and $\omega = 1$ *rps* were selected to compare the computation cost of solvers `sbm4Foam` and `tfmFoam`. They were performed in serial runs using an Intel® Core™ i7-7800X CPU @ 3.50GHz (6 cores, 16 Gb RAM), with total execution time needed for the simulations to achieve the steady state of 1.6 hours with the SBM and 43.1 hours with the TFM. This significant difference is due to the different strategies adopted regarding the time step: for the two-fluid solver, the explicit formulation of the anisotropic stress (Equation 4.51) may cause instabilities when the maximum packing fraction is approached. If these instabilities occur, the Courant number must be reduced by reducing the time step - stable results

Table 5.4: Values of the time step used with the `sbm4Foam` solver for the simulation with $\omega = 1$ *rps* and the respective maximum Courant numbers.

Range (revolutions)	Δt (s)	Maximum Courant
0 to 20	0.005	0.55
21 to 100	0.01	1.1
101 to 1000	0.05	5.3
1001 to 2000	0.1	10.7
2001 to 5000	0.5	53.8
5001 to 12000	1.0	107.5

were obtained using a time step of $\Delta t = 0.005$ s, kept constant during the whole run, yielding a maximum Courant number of $Co = 0.65$. This instability problem is not faced by the suspension balance model, which allows increasing the time step to accelerate the run. The values of the time steps used for the simulation with the `sbm4Foam` solver and the corresponding maximum Courant numbers are reported in Table 5.4.

5.3.2 Estimation of Rheological Parameters

Using setup I-B, simulations varying the inner cylinder rotation from 0.5 to 48 *rps* were performed for geometry A to estimate the suspension's power-law model parameters. Regardless of the rotational speed of the inner cylinder, all simulations performed with each model provided exactly the same steady-state results for the solid-phase fraction profile and dimensionless velocity. This independence of the steady-state dispersed-phase fraction on the rotational speed is proven by dimensional analysis of both models, detailed in Appendix B, and was observed experimentally by PHILLIPS *et al.* [3]. This observation suggests a Newtonian behavior of the suspension, with no dependence of the developed dispersed-phase fraction profile and, consequently, of the viscosity, on the applied shear rate. The minimum and maximum values of the solid-phase fraction are observed, respectively, at the boundaries of the inner and outer cylinders, being listed in Table 5.5. The shear rate values at the inner cylinder surface, represented by $\dot{\gamma}_w$, and the particle's Reynolds number are shown in Table 5.6 for all simulations.

The steady-state radial profiles for the dispersed-phase fraction obtained with both models are compared to the experimental data and to the predicted values from the semi-analytical solution of the suspension balance model [14] in Figure 5.9. Considering the 2% minimum experimental error for the data of PHILLIPS *et al.* [3] and the estimated grid uncertainties, both models provide results statistically equivalent to the experimental data only in the outer half of the gap. The SBM and TFM simulations give different results close to the inner cylinder up until $\zeta \approx 0.3$.

Table 5.5: Mean values and standard deviation of the steady-state dispersed-phase fraction and the uncertainty on its determination obtained from the Couette flow simulations in geometry A with different cylinder rotations.

		$r = R_i$		$r = R_o$	
		SBM	TFM	SBM	TFM
ϕ	Mean	0.2975	0.2829	0.6403	0.6386
	Std. deviation	0.38×10^{-5}	17.4×10^{-5}	0.21×10^{-5}	25.3×10^{-5}
U_{m2}	Mean	0.0013	0.0021	0.0027	0.0046
	Std. Deviation	0.16×10^{-7}	12.6×10^{-7}	0.09×10^{-7}	18.4×10^{-7}

Table 5.6: Shear rate at the inner cylinder for the Couette flow simulations in geometry A at the steady-state.

	$\dot{\gamma}_w$ $(1/s)$		Re_p	
ω (rps)	SBM	TFM	SBM	TFM
0.5	10.22	10.72	1.46×10^{-4}	1.53×10^{-4}
1.0	20.43	21.39	2.91×10^{-4}	3.05×10^{-4}
2.0	40.86	42.80	5.82×10^{-4}	6.10×10^{-4}
3.0	61.29	64.18	8.73×10^{-4}	9.14×10^{-4}
4.0	81.72	85.58	1.16×10^{-3}	1.22×10^{-3}
8.0	163.45	171.14	2.33×10^{-3}	2.44×10^{-3}
16.0	326.89	342.42	4.66×10^{-3}	4.88×10^{-3}
48.0	980.69	1026.77	1.40×10^{-2}	1.46×10^{-2}

Both models predicted dispersed-phase fraction radial profiles that are statistically equivalent to the semi-analytical solution of MORRIS and BOULAY [14]. Despite the lack of consensus on how to introduce the normal stresses responsible for shear-induced migration on the multiphase framework, as discussed in the literature review based on the papers of NOTT *et al.* [49] and JAMSHIDI *et al.* [50], the formulation of MUNICCHI *et al.* [16] successfully captures the essential behavior of the suspension and provides results that agree well with the suspension balance model.

Parameters m and n from Equation 3.59 are determined using the orthogonal distance regression (ODR) using as the uncertainty in the torque values the grid uncertainty given in Table 5.2. Since the rotating velocity ω is imposed for each simulation, no error was considered for this variable. The calculated values for the torque at the inner cylinder for each simulation are plotted in Figure 5.10 along with the fitted curves using Equation 3.59. Notice that the difference between the torque calculated using these both models increases with the rotational speed of the inner cylinder.

The fitted parameters of the power-law model (Equation 3.59) are shown in Table 5.7. Despite the presence of normal stress anisotropy being a non-Newtonian feature of the suspension under study, the fitted behavior is of a typically Newtonian fluid with $n = 1$. Thus, parameter m can and shall be from now on referred to as the

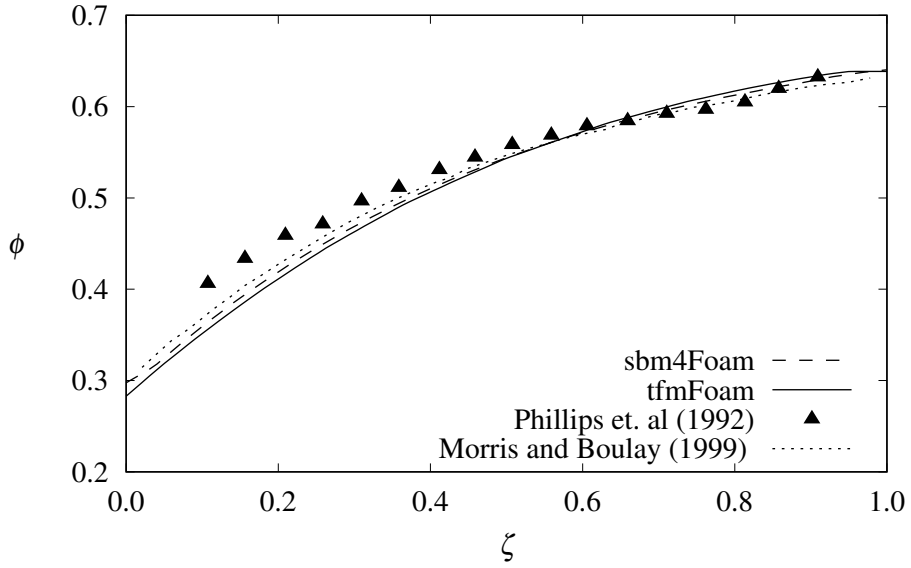

Figure 5.9: Radial profiles of the dispersed-phase fraction at the steady state obtained for the Couette flow simulations in geometry A, and the literature experimental and semi-analytical solution data.

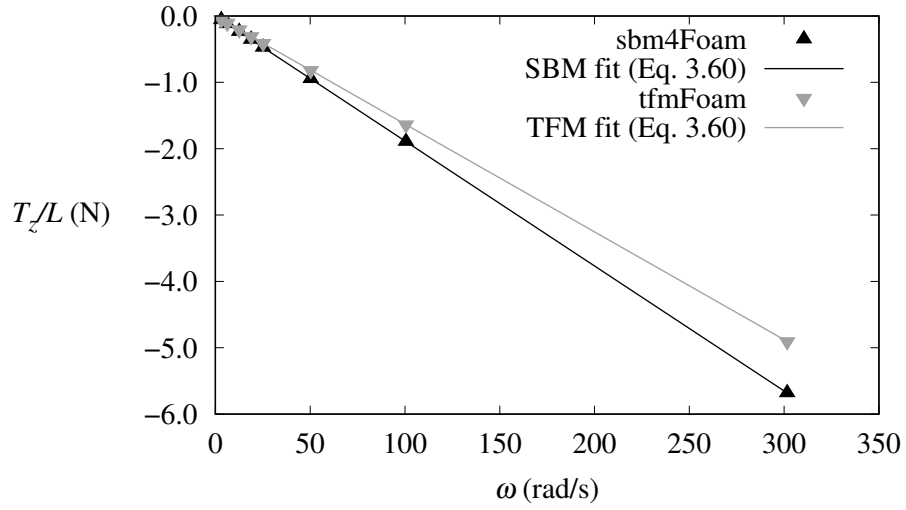

Figure 5.10: z-component of the torque at the inner cylinder calculated from the Couette flow simulations in geometry A with the `sbm4Foam` and `tfmFoam` solvers.

Table 5.7: Estimates for the rheological parameters of the power-law model using the simulated results from the Couette flows in geometry A with the `sbm4Foam` and `tfmFoam` solvers.

	SBM	TFM
n	$1.00 \pm 1.9 \times 10^{-5}$	$1.00 \pm 0.95 \times 10^{-5}$
m $(Pa.s)$	33.95 ± 0.009	29.33 ± 0.41
ϕ_{calc}	0.382	0.355

apparent dynamic viscosity of the suspension. Using the results obtained with both models, different values of the apparent viscosity are estimated, with a higher value obtained from the suspension balance model simulations. Moreover, it should be noted that the values of the suspension's apparent viscosity are significantly greater than the viscosity of the pure fluid phase, $\mu_f = 9.45\ Pa.s$, and they do not match the suspension's viscosity values calculated using Equation 3.26 for the particles' shear viscosity neither using the value of the simulated dispersed-phase fraction at the inner cylinder surface nor the bulk solid-phase fraction. The dispersed-phase fraction values for which the estimated apparent viscosities correspond to the predictions of Equation 3.26 are also shown in Table 5.7 as ϕ_{calc}. This contradictory conclusion shows that, considering simple non-Newtonian models such as the power-law, the apparent viscosity determined experimentally does not match the actual local suspension viscosity close to the inner cylinder nor the viscosity of the suspension if it was homogeneous, according to the viscosity model of MORRIS and BOULAY [14].

Geometry Dependence of the Power-Law Parameters

After the determination of the model parameters using the Couette rheometer A, the remaining simulations for geometries B and C were performed using the `sbm4Foam` solver to investigate the dependence on the rheometer geometry of the segregation profiles and, consequently, of the estimated rheological parameters. The dispersed-phase fraction radial profiles obtained from simulations in geometries A, B and C are shown in Figure 5.11, with the simulated values of ϕ at the cylinder walls reported in Table 5.8 along with the uncertainty on their determination. The simulated phase-fraction profiles from geometries A and C are equivalent, while for geometry B less segregation of the phases is observed. The suspension's angular velocity radial profiles are presented in Figure 5.12, which shows the impact of the different segregation profiles on the suspension's velocity. It is seen also for the radial velocity profile that simulations in geometries A and C provide results that are equivalent. These observations show that the similarity of the flows is dictated by the ratio between the inner cylinder and the gap size, R_i/l, which is the same for geometries A and C.

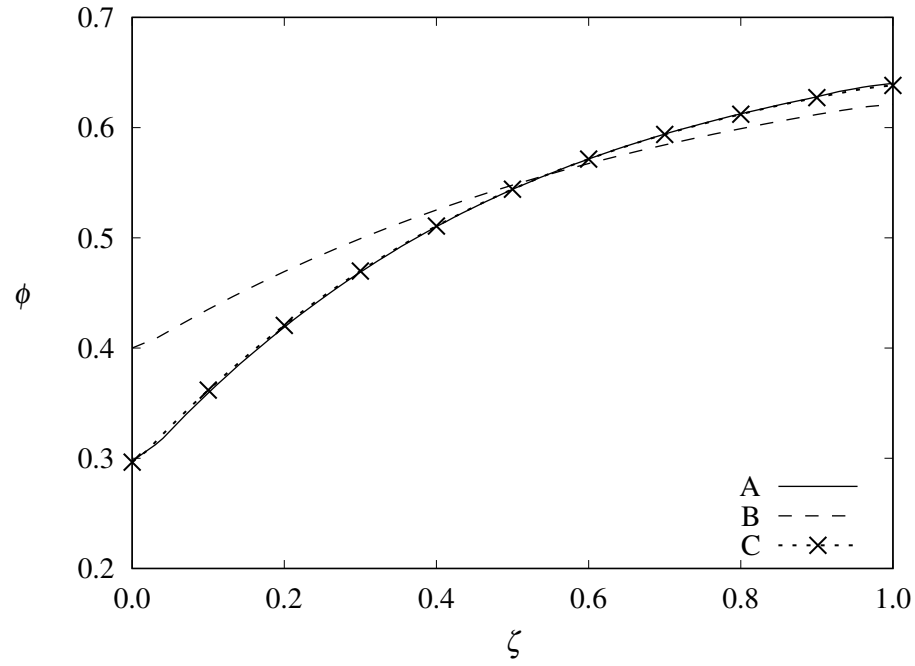

Figure 5.11: Radial profiles of the dispersed-phase fraction at the steady state obtained for the Couette flow simulations in different geometries using the `sbm4Foam` solver.

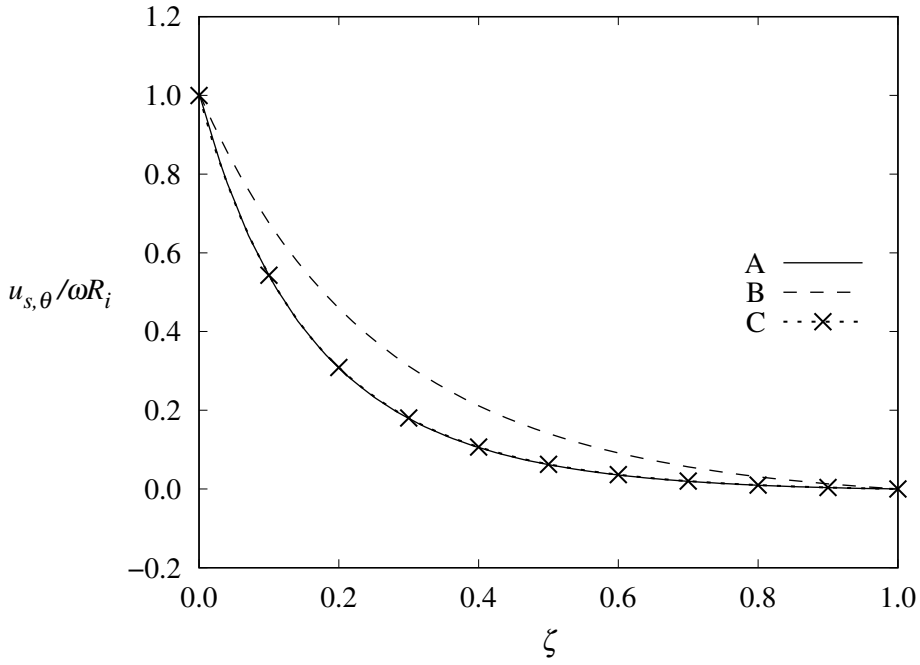

Figure 5.12: Radial profiles of the angular suspension velocity at the steady state obtained for the Couette flow simulations in different geometries using the `sbm4Foam` solver.

Table 5.8: Mean values and standard deviation of the steady-state dispersed-phase fraction and the uncertainty on its determination obtained from the Couette flow simulations in geometries B and C with different cylinder rotations. Simulations were performed using the `sbm4Foam` solver.

		B		C	
		$r = R_i$	$r = R_o$	$r = R_i$	$r = R_o$
ϕ	Mean	0.4004	0.6210	0.2965	0.6382
	Std. Deviation	6.76×10^{-4}	2.77×10^{-4}	1.53×10^{-4}	1.62×10^{-4}
U_{m2}	Mean	0.0107	0.0132	0.0076	0.0163
	Std. Deviation	0.16×10^{-6}	6.48×10^{-6}	3.91×10^{-6}	4.14×10^{-6}

The calculated values for the torque at the inner cylinder are presented in Figure 5.13 for geometries A, B, and C. Repeating the procedure to estimate the power-law parameters from Equation 3.59 using ODR with the results from simulations in geometries B and C provides the values shown in Table 5.9. The corresponding values of ϕ_{calc} are also reported in this table, which are calculated using the apparent suspension viscosities m to determine the particle-phase shear viscosity and, then, determine the corresponding phase-fraction value using Equation 3.26. The previously obtained results for geometry A using the `sbm4Foam` solver are repeated for comparison. A value of $n = 1$ is estimated with the results from simulations in all geometries, representing a Newtonian behavior of the suspension. The estimated apparent viscosities, on the other hand, are all statistically different. For simulations in geometries A and C, which provided the same values of ϕ at the cylinder walls, the estimated values differ only by 1.87%. Results from the flow simulations in geometry B provided a greater value of the suspension's apparent viscosity, as expected since the dispersed-phase fraction at the inner cylinder wall was also greater than the simulated values for geometries A and C. Therefore, the estimation of rheological parameters depends on the size of the rheometer and the associated segregation profile. Despite the independence of the dispersed-phase fraction profiles on the imposed shear-rate and of the estimation of a $n = 1$ parameter for the power-law model, the geometry dependence represents a non-Newtonian behavior. Hence, for suspension under the same flow conditions considered in this work with dominance of the viscous effects and may exhibit shear-induced migration, the experimental measurement of the suspension's viscosity and the data interpretation are not straightforward since significantly different results may be obtained using different rheometers.

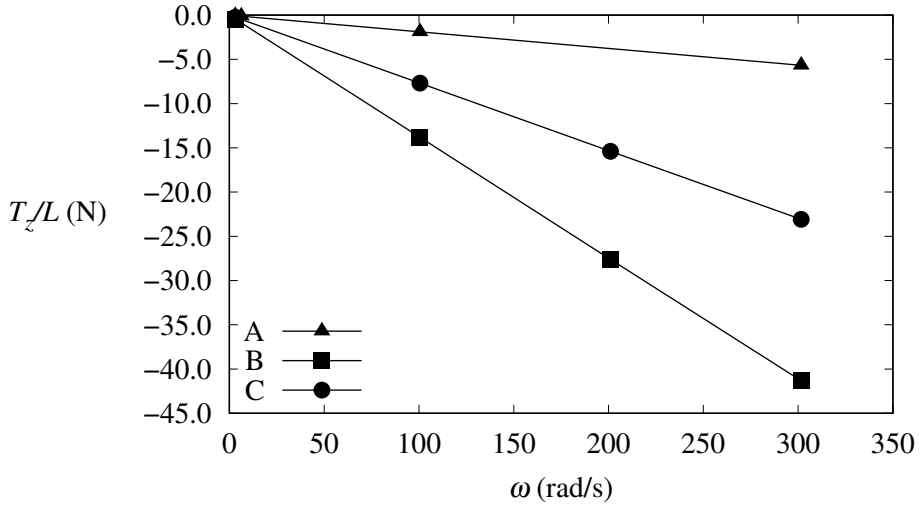

Figure 5.13: z-component of the torque at the inner cylinder calculated from the Couette flow simulations with the `sbm4Foam` solver in different geometries.

Table 5.9: Estimates for the rheological parameters of the power-law model using the simulated results from the Couette flows in geometries A, B, and C with the `sbm4Foam` solver.

	A	B	C
n	$1.00 \pm 1.9 \times 10^{-5}$	$1.00 \pm 0.49 \times 10^{-4}$	$1.00 \pm 2.1 \times 10^{-4}$
m $(Pa.s)$	33.95 ± 0.009	56.04 ± 3.829	34.59 ± 0.10
ϕ_{calc}	0.382	0.473	0.398

5.4 Channel Flow

Simulations for all considered linear channel geometries (listed in Table 4.4) were performed using the `tfmFoam` solver, using the same suspension employed in the analysis of the Couette flow. To confirm if a fully-developed flow regime was achieved, the dispersed-phase fraction and the x-component of the suspension's velocity were evaluated along the center line of the channel, as shown in Figures 5.14 and 5.15, respectively. It is shown that only the simulation performed in geometry D did not achieve a fully-developed state. According to the estimated minimum lengths (see Table 4.4), this is the geometry for which the actual channel length was shorter, with $L \approx 2L_{min}$, due to the significant increase in the computational cost of the simulations. Therefore, the remaining analysis considers only the simulations in geometries A, B, and C.

Results for the minimum and maximum values of the dispersed-phase fraction are presented in Table 5.10. Regardless of the mean velocity of the flow, the same steady-

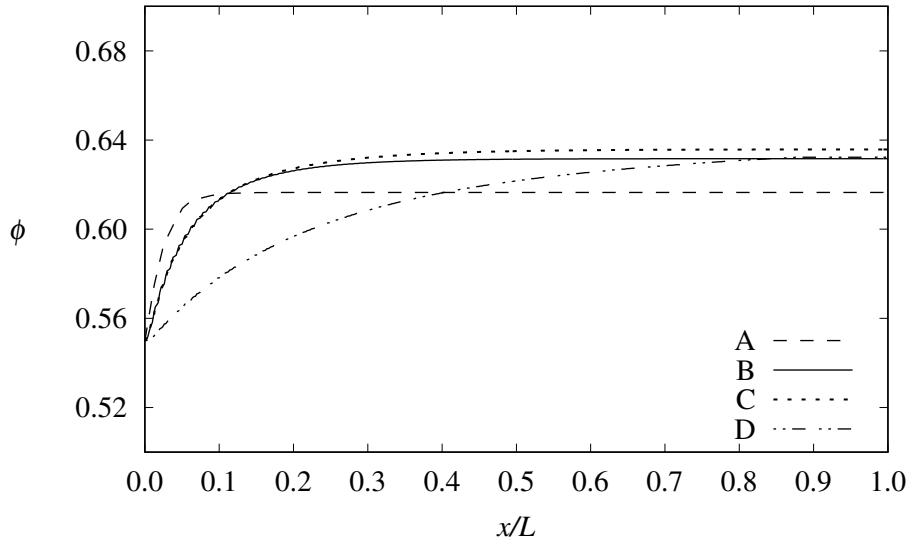

Figure 5.14: Dispersed-phase fraction axial profiles along the center line of the 2-D channels A, B, C, and D.

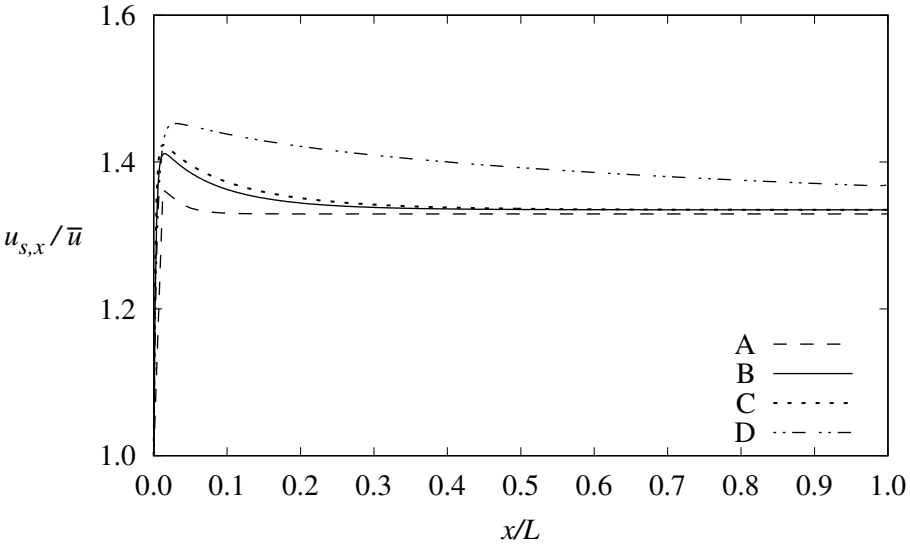

Figure 5.15: x-component of the suspension's velocity along the center line of the 2-D channels A, B, C, and D.

Table 5.10: Minimum and maximum values of the dispersed-phase fraction and wall shear rate obtained for the 2-D channel simulations.

Geometry	$\overline{u}$ (m/s)	ϕ_{min}	ϕ_{max}	$\dot{\gamma}_w$ $(1/s)$	Re_p
A	2	0.450	0.617	1926.3	2.74×10^{-2}
A	0.2	0.450	0.617	192.6	2.74×10^{-3}
A	0.02	0.450	0.617	19.3	2.74×10^{-4}
B	2	0.435	0.632	974.2	1.39×10^{-2}
B	0.2	0.435	0.632	97.4	1.39×10^{-3}
B	0.02	0.435	0.632	9.7	1.39×10^{-4}
C	2	0.431	0.636	779.5	1.11×10^{-2}

state dispersed-phase fraction vertical profile is predicted for a given geometry. Thus, for the flow simulations in geometries A and B, the three maximum and minimum reported values of ϕ are identical. This independence of the results on the velocity boundary condition had already been observed for the Couette flow simulations and explained by dimensional analysis of both models. Once this behavior was confirmed for the 2-D channel in geometries A and B, the following simulations in geometries C and D were performed for only one value of the mean velocity (results from geometry D are not included in Table 5.10 since they were disregarded from this analysis). The values for the shear rate at the walls are also presented in Table 5.10 as $\dot{\gamma}_w$: they are within the same range of shear rates imposed on the Couette flow simulations used to estimate the power-law model parameters (reported in Table 5.6); the resulting particle's Reynolds number are also reported in Table 5.10.

The steady-state dispersed-phase fraction profiles obtained for the different geometries are plotted in Figure 5.16 along a vertical line located at the fully-developed section of the channels. As can also be observed from the ϕ_{min} and ϕ_{max} values in Table 5.10, Figure 5.16 shows that the dispersed-phase fraction cross-sectional profiles are geometry dependent. As the channel width increases from geometry A to C, so does the segregation. This important observation shows that, even for similar geometries, different rheological responses may be observed for the flow of a given suspension, as was previously observed also for the Couette flows. The different dispersed-phase fraction profiles lead to different velocity profiles, as seen in Figure 5.17. Since the width difference between B and C is inferior to that between A and B (4 mm versus 2 mm), the differences in the solid-phase fraction and velocity profiles, particularly for the latter, in Figures 5.16 and 5.17, are quite small for geometries B and C.

Table 5.11 shows the pressure drop in the fully-developed section of the channels calculated by two different procedures. The pressure drop values estimated using Equation 3.61 and the power-law parameters listed in Table 5.7 regarding the two-fluid model estimates are called $(-\Delta P/\Delta L)_{calc}$, whereas the values obtained from

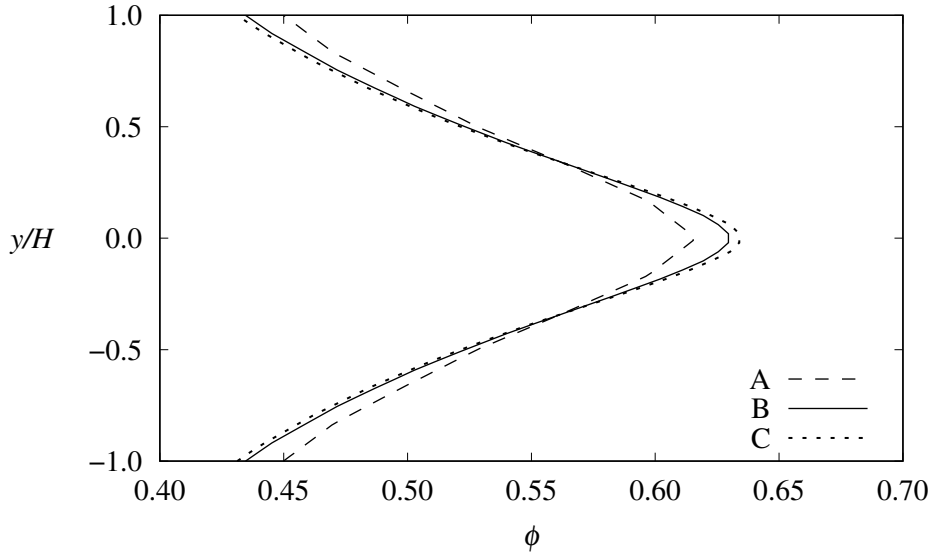

Figure 5.16: Vertical profile of the steady-state dispersed-phase fraction for the 2-D channel flows in geometries A, B, and C.

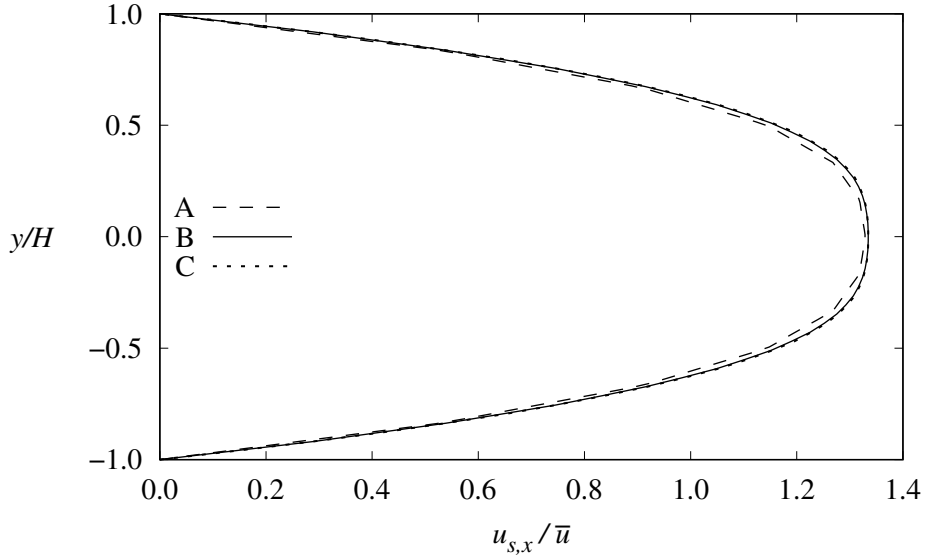

Figure 5.17: Vertical profile of the steady-state x-component of the suspension's velocity for the 2-D channel flows in geometries A, B, and C.

Table 5.11: Comparison of the estimated and simulated values of the pressure drop in the linear channel simulations with geometries A, B, and C. The estimated pressure drops consider the power-law coefficients obtained from the simulations of the Couette flow in geometry A using the `tfmFoam` solver.

Geometry	$\overline{u}$ (m/s)	$\left(-\frac{\Delta P}{\Delta L}\right)_{calc}$ (Pa/m)	$\left(-\frac{\Delta P}{\Delta L}\right)_{sim}$ (Pa/m)	Rel. Dif. (%)
A	2	1.10×10^7	1.88×10^7	41.52
A	0.2	1.10×10^6	1.88×10^6	41.52
A	0.02	1.10×10^5	1.88×10^5	41.52
B	2	2.75×10^6	4.41×10^6	37.63
B	0.2	2.75×10^5	4.41×10^5	37.63
B	0.02	2.75×10^4	4.41×10^4	37.63
C	2	1.76×10^6	2.78×10^6	36.64

Table 5.12: Comparison of the estimated and simulated values of the pressure drop in the linear channel simulations with geometries A, B, and C. The estimated pressure drops consider the power-law coefficients obtained from the simulations of the Couette flow in geometry B using the `sbm4Foam` solver.

Geometry	$\overline{u}$ (m/s)	$\left(-\frac{\Delta P}{\Delta L}\right)_{calc}$ (Pa/m)	$\left(-\frac{\Delta P}{\Delta L}\right)_{sim}$ (Pa/m)	Rel. Dif. (%)
A	2	2.10×10^7	1.88×10^7	11.73
A	0.2	2.10×10^6	1.88×10^6	11.73
A	0.02	2.10×10^5	1.88×10^5	11.73
B	2	5.25×10^6	4.41×10^6	19.15
B	0.2	5.25×10^5	4.41×10^5	19.15
B	0.02	5.25×10^4	4.41×10^4	19.15
C	2	3.36×10^6	2.78×10^6	21.06

the 2-D channel flow simulations are reported as $(-\Delta P/\Delta L)_{sim}$ for comparison, followed by their relative differences. The actual pressure drops measured with the channel flow simulations' results are higher than those predicted using the analytical solution and estimated parameters, with differences varying from 36% to 41%. Since the simulations of the Couette flow in geometry B using the `sbm4Foam` solver provided a significantly different estimation of the suspension's apparent viscosity, the comparisons made in Table 5.11 were repeated, using the value of m corresponding to the estimates from this geometry. The calculated pressure drops are shown in Table 5.12, along with the relative difference to the simulated values. The difference between the estimated and the simulated values decreased significantly, varying from 11% to 21%.

Additionally, the observed values of $(-\Delta P/\Delta L)_{sim}$ from Table 5.11 are used in Equation 3.61 with $n = 1$ to determine the corresponding suspension's apparent viscosity, which is in turn used to calculate the particle-phase shear viscosity $\mu_p = \mu_s - \mu_f$ together with Equation 3.26 to determine the corresponding value of the dispersed-phase fraction. These corresponding values are reported in Table 5.13 as,

Table 5.13: Estimated apparent viscosity and corresponding solid-phase fraction calculated with the linear channel simulations' results for geometries A, B, and C.

Geometry	$\overline{u}$ (m/s)	m_{calc} $(Pa.s)$	ϕ_{calc}
A	2	50.16	0.470
A	0.2	50.16	0.470
A	0.02	50.16	0.470
B	2	47.03	0.441
B	0.2	47.03	0.441
B	0.02	47.03	0.441
C	2	46.29	0.423

respectively, m_{calc} and ϕ_{calc}. The apparent viscosities m_{calc} decrease from geometry A to C, with the increase in particle segregation, with values that are higher than those estimated with the Couette flow simulations in geometries A and C but are lower than the one from geometry B (see Table 5.9). By comparing the values of the dispersed-phase fraction at the inner Couette cylinder and the channel walls, we see that even if the segregation profile obtained for the channel flows presented the same maximum and minimum values of ϕ than any of the considered Couette geometries, the estimated apparent viscosities using Equation 3.59 and 3.61 would not be the same.

Chapter 6

Conclusions

The present work focused on studying the effects of the shear-induced migration in dense suspension flows of non-colloidal, non-Brownian, and neutrally buoyant rigid spheres dispersed in a Newtonian fluid, flowing in the Stokes regime. The Couette and 2-D straight channel flows were simulated using the open-source software OpenFOAM-v7®.

An improved implementation of the suspension balance model is presented and will be made available to the scientific community after the publication of its results. The improved solver uses the model of MORRIS and BOULAY [14] for the suspension's shear viscosity, which provides more accurate results than the viscosity model implemented in the original solver. It features a frame-independent formulation of the anisotropic particle-phase stress tensor, which can be used to simulate three-dimensional flows in generic geometries regardless of the main directions of the flow. An improved momentum interpolation scheme is included to eliminate numerical oscillations in the simulated dispersed-phase fraction field.

An implementation of the two-fluid model accounting for shear-induced particle migration is presented and compared to the improved implementation of the suspension balance model through a series of simulations of suspension flows in a Couette cell. Both models are shown to be qualitatively compatible, with slightly different results in the inner region of the Couette cell gap. Therefore, for situations in which the SBM assumptions are valid and the interest is to obtain the steady state results, there is an advantage on using this simplified solver (`sbm4Foam`) instead of the complete and more computationally demanding TFM solver (`tfmFoam`).

By using the Couette simulations' results in different geometries as input for the rheological characterization of the suspension similarly to the experimental procedure, it was shown that, even though the suspension behaves as a Newtonian fluid regarding the dependence of the viscosity with the shear rate, its viscosity depends on the geometry of the rheometer used on the characterization procedure, which is intrinsically a non-Newtonian characteristic. Therefore, the classical procedure of

assuming a simple non-Newtonian model (in this case, of a power-law fluid) and fitting the experimental data to the analytical solution does not provide an accurate description of the suspension. Flow simulations in different 2-D straight channels showed that the rheological characterization of the suspension obtained mimicking classic rheometry experiments is not sufficient to accurately predict the suspension flow in different flow conditions and confirmed the dependency of the estimated rheological parameters on the flow geometry.

6.1 Future Work Suggestions

Considering the results obtained in this work, future work is needed to better understand to what extent the shear-induced migration interferes with the results of the experimental characterization procedure of suspensions. Both presented models can be extended to include other effects besides the shear-induced migration, such as those due to Brownian motion, buoyancy, and polydispersity. The latter has to be carefully considered since the behavior of different-sized particles can be controlled by different types of interaction (e.g., Brownian motion may be dominant for finer particles and shear-induced migration for the larger ones). Then, the resulting solvers can be used to analyze the influence of each phenomenon on the suspension flow and simulate different conditions, including the experimental procedure in smaller rheometers.

References

[1] COUSSOT, P., ANCEY, C. "Rheophysical Classification of Concentrated Suspensions and Granular Pastes", *Physical Review E*, v. 59, pp. 4445 – 4457, 1999. doi: 10.1103/PhysRevE.59.4445.

[2] LEIGHTON, D., ACRIVOS, A. "The shear-induced migration of particles in concentrated suspensions", *Journal of Fluid Mechanics*, v. 181, pp. 415–439, 1987. doi: 10.1017/S0022112087002155.

[3] PHILLIPS, R. J., ARMSTRONG, R. C., BROWN, R. A., et al. "A constitutive equation for concentrated suspensions that accounts for shear induced particle migration", *Physics of Fluids A*, v. 4:1, pp. 30 – 40, 1992. doi: 10.1063/1.858498.

[4] KANG, C., MIRBOD, P. "Shear-induced particle migration of semi-dilute and concentrated Brownian suspensions in both Poiseuille and circular Couette flow", *International Journal of Multiphase Flow*, v. 126, n. 103239, 2020. doi: 10.1016/j.ijmultiphaseflow.2020.103239.

[5] JAMSHIDI, R., ANGELI, P., MAZZEI, L. "On the closure problem of the effective stress in the Eulerian-Eulerian and mixture modeling approaches for the simulation of liquid-particle suspensions", *Physics of Fluid*, v. 31, n. 013302, 2019. doi: 10.1063/1.5081677.

[6] MILLER, R. M., MORRIS, J. F. "Normal stress-driven migration and axial development in pressure-driven flow of concentrated suspensions", *Journal of Non-Newtonian Fluid Mechanics*, v. 135, pp. 149–165, 2006. ISSN: 0377-0257. doi: 10.1016/j.jnnfm.2005.11.009.

[7] DRIJER, I., VAN DE LAAR, T., VOLLEBREGT, H., et al. "From highly specialised to generally available modelling of shear induced particle migration for flow segregation based separation technology", *Separation and Purification Technology*, v. 192, pp. 99 – 109, 2018. doi: 10.1016/j.seppur.2017.10.001.

[8] SCHROËN, K., VAN DINTHER, A., STOCKMANN, R. "Particle migration in laminar shear fields: A new basis for large scale separation technology?" *Separation and Purification Technology*, v. 174, pp. 372 – 388, 2017. doi: 10.1016/j.seppur.2016.10.057.

[9] GILLISSEN, J. J. J., WILSON, H. J. "Modelling Sphere Suspension Microstructure and Stress", *Physical Review E*, v. 98, n. 033119, 2018. doi: 10.1103/PhysRevE.98.033119.

[10] GUAZZELLI, E., POULIQUEN, O. "Rheology of dense granular suspensions", *Journal of Fluid Mechanics*, v. 852, pp. 748–783, 2018. doi: 10.1017/jfm.2018.5489.

[11] DONTSOV, E., PEIRCE, A. "Slurry flow, gravitational settling and a proppant transport model for hydraulic fractures", *Journal of Fluid Mechanics*, v. 760, pp. 567–590, 2014. doi: 10.1017/jfm.2014.606.

[12] ALMASHWALI, A. A., BAVOH, C. B., LAL, B., et al. "Gas Hydrate in Oil-Dominant Systems: A Review", *ACS Omega*, v. 7, pp. 27021–27037, 2022. doi: 10.1021/acsomega.2c02278.

[13] NOTT, P. R., BRADY, J. F. "Pressure-driven flow of suspensions: simulation and theory", *Journal of Fluid Mechanics*, v. 275, pp. 157 – 199, 1994. doi: 10.1017/S0022112094002326.

[14] MORRIS, J. F., BOULAY, F. "Curvilinear flows of noncolloidal suspensions: The role of normal stresses", *Journal of Rheology*, v. 43, pp. 1213 – 1237, 1999. doi: 10.1122/1.551021.

[15] DBOUK, T., LEMAIRE, E., LOBRY, L., et al. "Shear-induced particle migration: Predictions from experimental evaluation of the particle stress tensor", *Journal of Non-Newtonian Fluid Mechanics*, v. 198, pp. 78 – 95, 2013. doi: 10.1016/j.jnnfm.2013.03.006.

[16] MUNICCHI, F., NAGRANI, P. P., CHRISTOV, I. C. "A two-fluid model for numerical simulation of shear-dominated suspension flows", *International Journal of Multiphase Flow*, v. 120, n. 103079, 2019. doi: 10.1016/j.ijmultiphaseflow.2019.07.015.

[17] WELLER, H. G., TABOR, G., JASAK, H., et al. "A tensorial approach to computational continuum mechanics using object-oriented techniques", *Computers in Physics*, v. 12, pp. 620–631, 1998. doi: 10.1063/1.168744.

[18] EINSTEIN, A. "Eine neue Bestimmung der Moleküldimensionen", *Annalen der Physik*, v. 324, n. 2, pp. 289–306, 1906. doi: 10.1002/andp.19063240204.

[19] EINSTEIN, A. "Berichtigung zu meiner Arbeit: Eine neue Bestimmung der Moleküldimensionen", *Annalen der Physik*, v. 339, n. 3, pp. 591–592, 1911. doi: 10.1002/andp.19113390313.

[20] GADALA-MARIA, F., ACRIVOS, A. "Shear-Induced Structure in a Concentrated Suspension of Solid Spheres", *Journal of Rheology*, v. 24, n. 6, pp. 799–814, 1980. doi: 10.1122/1.549584.

[21] HOFFMAN, R. L. "Discontinuous and Dilatant Viscosity Behavior in Concentrated Suspensions. I. Observation of a Flow Instability", *Transactions of the Society of Rheology*, v. 16, n. 1, pp. 155–173, 1972. doi: 10.1122/1.549250.

[22] BOSSIS, G., BRADY, J. F. "Dynamic simulation of sheared suspensions. I. General method", *The Journal of Chemical Physics*, v. 80, n. 10, pp. 5141–5154, 1984. doi: 10.1063/1.446585.

[23] BRADY, J. F. "Computer simulation of viscous suspensions", *Chemical Engineering Science*, v. 56, n. 9, pp. 2921–2926, 2001. doi: 10.1016/S0009-2509(00)00475-9.

[24] SETO, R., GIUSTERI, G., MARTINIELLO, A. "Microstructure and thickening of dense suspensions under extensional and shear flows", *Journal of Fluid Mechanics*, v. 825, n. R3, 2017. doi: 10.1017/jfm.2017.469.

[25] YURKOVETSKY, Y. *I. Statistical mechanics of bubbly liquids. II. Behavior of sheared suspensions of non-Brownian particles*. Ph. D. thesis, California Institute of Technology, Pasadena, California, USA, 1998.

[26] HERNÁNDEZ, R. "Dynamics of concentrated suspensions in two-dimensional channel flow for non-Newtonian slurries", *International Journal of Multiphase Flow*, v. 139, n. 103616, 2021. doi: 10.1016/j.ijmultiphaseflow.2021.103616.

[27] SIQUEIRA, I., DE SOUZA MENDES, P. "On the pressure-driven flow of suspensions: Particle migration in apparent yield-stress fluids", *Journal of Non-Newtonian Fluid Mechanics*, v. 265, pp. 92–98, 2019. ISSN: 0377-0257. doi: 10.1016/j.jnnfm.2019.02.002.

[28] DREW, D. A., LAHEY, R. T. "Analytical modeling of multiphase flow". In: *Particulate Two-Phase Flow*, cap. 16, Boston, Butterworth-Heinemann, 1993.

[29] MAZZEI, L. "Recent Advances in Modeling Gas-Particle Flows". In: *Handbook of Multiphase Flow Science and Technology*, pp. 1–43, Singapore, Springer Singapore, 2017. ISBN: 978-981-4585-86-6. doi: 10.1007/978-981-4585-86-6_8-1.

[30] MILLS, P., SNABRE, P. "Rheology and Structure of Concentrated Suspensions of Hard Spheres. Shear Induced Particle Migration", *Journal de Physique II*, v. 5, pp. 1597–1608, 1995. doi: 10.1051/jp2:1995201.

[31] BRADY, J. F., MORRIS, J. F. "Microstructure of strongly sheared suspensions and its impact on rheology and diffusion", *Journal of Fluid Mechanics*, v. 348, n. 1, pp. 103–139, 1997. doi: 10.1017/S0022112097006320.

[32] MORRIS, J. F., BRADY, J. F. "Pressure-driven flow of a suspension: buoyancy effects", *International Journal of Multiphase Flows*, v. 24, pp. 105 – 130, 1997. doi: 10.1016/S0301-9322(97)00035-9.

[33] MILLER, R. M., P.SINGH, J., MORRIS, J. F. "Suspension flow modeling for general geometries", *Chemical Engineering Science*, v. 64, pp. 4597 – 4610, 2009. doi: 10.1016/j.ces.2009.04.033.

[34] DBOUK, T., LOBRY, L., LEMAIRE, E. "Normal stresses in concentrated non-Brownian suspensions", *Journal of Fluid Mechanics*, v. 715, pp. 239 – 272, 2013. doi: 10.1017/jfm.2012.516.

[35] DEBOEUF, A. *Interactions hydrodynamiques dans les suspensions macroscopiques*. Ph. D. thesis, Université Pierre et Marie Curie - Paris VI, 2008.

[36] DEBOEUF, A., GAUTHIER, G., MARTIN, J., et al. "Particle Pressure in a Sheared Suspension: A Bridge from Osmosis to Granular Dilatancy", *Physical Review Letters*, v. 102, n. 108301, 2009. doi: 10.1103/PhysRevLett.102.108301.

[37] BOYER, F., POULIQUEN, O., GUAZZELLI, E. "Dense suspensions in rotating-rod flows: normal stresses and particle migration", *Journal of Fluid Mechanics*, v. 686, pp. 5 – 25, 2011. doi: 10.1017/jfm.2011.272.

[38] COUTURIER, E., BOYER, F., POULIQUEN, O., et al. "Suspensions in a tilted trough: second normal stress difference", *Journal of Fluid Mechanics*, v. 686, pp. 26–39, 2011. doi: 10.1017/jfm.2011.315.

[39] SINGH, A., NOTT, P. R. "Experimental measurements of the normal stresses in sheared Stokesian suspensions", *Journal of Fluid Mechanics*, v. 490, pp. 293–320, 2003. doi: 10.1017/S0022112003005366.

[40] ZARRAGA, I. E., HILL, D. A., LEIGHTON, D. T. "The characterization of the total stress of concentrated suspensions of noncolloidal spheres in Newtonian fluids", *Journal of Rheology*, v. 44, pp. 185–220, 2000. doi: 10.1122/1.551083.

[41] GAO, C., XU, B., GILCHRIST, J. "Mixing and segregation of microspheres in microchannel flows of mono- and bidispersed suspensions", *Physical Review E*, v. 79, n. 036311, 2009. doi: 10.1103/PhysRevE.79.036311.

[42] FRANK, M., ANDERSON, D., WEEKS, E., et al. "Particle migration in pressure driven flow of Brownian suspension", *Journal of Fluid Mechanics*, v. 493, pp. 363–378, 2003. doi: 10.1017/S0022112003006001.

[43] VON PFEIL, K., GRAHAM, M. D., KLINGENBERG, D. J., et al. "Structure evolution in electrorheological and magnetorheological suspensions from a continuum perspective", *Journal of Applied Physics*, v. 93, n. 9, pp. 5769–5779, 2003. doi: 10.1063/1.1563037.

[44] BOYER, F., GUAZZELLI, E., POULIQUEN, O. "Unifying Suspension and Granular Rheology", *Physical Review Letters*, v. 107, n. 188301, 2011. doi: 10.1103/PhysRevLett.107.188301.

[45] DA CRUZ, F., EMAM, S., PROCHNOW, M., et al. "Rheophysics of dense granular materials: Discrete simulation of plane shear flows", *Physical Review E*, v. 72, n. 021309, 2005. doi: 10.1103/PhysRevE.72.021309.

[46] FORTERRE, Y., POULIQUEN, O. "Flows of Dense Granular Media", *Annual Review of Fluid Mechanics*, v. 40, n. 1, pp. 1–24, 2008. doi: 10.1146/annurev.fluid.40.111406.102142.

[47] LECAMPION, B., GARAGASH, D. I. "Confined flow of suspensions modelled by a frictional rheology", *Journal of Fluid Mechanics*, v. 759, pp. 197–235, 2014. doi: 10.1017/jfm.2014.557.

[48] TIWARI, P., ANTAL, S. P., PODOWSKI, M. Z. "Modeling shear-induced diffusion force in particulate flows", *Computers & Fluids*, v. 38, n. 4,

pp. 727–737, 2009. ISSN: 0045-7930. doi: 10.1016/j.compfluid.2008.09.007.

[49] NOTT, P., GUAZZELLI, E., POULIQUEN, O. "The suspension balance model revisited", *Physics of Fluids*, v. 23, n. 43304, 2011. doi: 10.1063/1.3570921.

[50] JAMSHIDI, R., GILLISSEN, J. J. J., ANGELI, P., et al. "Roles of solid effective stress and fluid-particle interaction force in modeling shear-induced particle migration in non-Brownian suspensions", *Physical Review Fluids*, v. 6, n. 014301, 2021. doi: 10.1103/PhysRevFluids.6.014301.

[51] PHILLIPS, R. J., BRADY, J. F., BOSSIS, G. "Hydrodynamic transport properties of hard-sphere dispersions. I. Suspensions of freely mobile particles", *The Physics of Fluids*, v. 31, n. 12, pp. 3462–3472, 1988. doi: 10.1063/1.866914.

[52] RICHARDSON, J., ZAKI, W. "Sedimentation and fluidisation: Part I", *Chemical Engineering Research and Design*, v. 75, pp. S82–S100, 1997. ISSN: 0263-8762. doi: 10.1016/S0263-8762(97)80006-8.

[53] INKSON, N. J., PAPOULIAS, D., TANDON, M., et al. "An Eulerian-Eulerian formulation of suspension rheology using the finite volume method", *Journal of Non-Newtonian Fluid Mechanics*, v. 245, pp. 38–48, 2017. ISSN: 0377-0257. doi: 10.1016/j.jnnfm.2017.05.002.

[54] BIRD, R. B., STEWART, W. E., LIGHTFOOT, E. N. *Transport Phenomena*. 2 ed. New York / Chichester / Weinheim / Brisbane / Singapore / Toronto, John Wiley & Sons, Inc., 2002.

[55] ANDRADE, D. E., FERRARI, M., COUSSOT, P. "The liquid regime of waxy oils suspensions: A magnetic resonance velocimetry analysis", *Journal of Non-Newtonian Fluid Mechanics*, v. 279, n. 104261, 2020. ISSN: 0377-0257. doi: 10.1016/j.jnnfm.2020.104261.

[56] CHERNOBUROVA, O., JENNY, M., KIESGEN DE RICHTER, S., et al. "Dynamic Behavior of Dilute Bentonite Suspensions under Different Chemical Conditions Studied via Magnetic Resonance Imaging Velocimetry", *Colloids and Interfaces*, v. 2, n. 41, 2018. ISSN: 2504-5377. doi: 10.3390/colloids2040041.

[57] HOLLINGSWORTH, K. G., JOHNS, M. L. "Rheo-nuclear magnetic resonance of emulsion systems", *Journal of Rheology*, v. 48, n. 4, pp. 787–803, 2004. doi: 10.1122/1.1753277.

[58] OVARLEZ, G., RODTS, S., RAGOUILLIAUX, A., et al. "Wide-gap Couette flows of dense emulsions: Local concentration measurements, and comparison between macroscopic and local constitutive law measurements through magnetic resonance imaging", *Physical Review E*, v. 78, n. 036307, 2008. doi: 10.1103/PhysRevE.78.036307.

[59] JASAK, H. *Error Analysis and Estimation for the Finite Volume Method with Applications to Fluid Flows*. Ph. D. thesis, Imperial College of Science, Technology and Medicine, University of London, 1996.

[60] PASSALACQUA, A., FOX, R. "Implementation of an iterative solution procedure for multi-fluid gas–particle flow models on unstructured grids", *Powder Technology*, v. 213, pp. 174–187, 2011. doi: 10.1016/j.powtec.2011.07.030.

[61] CELIK, I., GHIA, U., ROACHE, P., et al. "Procedure of Estimation and Reporting of Uncertainty Due to Discretization in CFD Applications", *Journal of Fluids Engineering*, v. 130, n. 078001, 2008. doi: 10.1115/1.2960953.

[62] PHILLIPS, T. S., ROY, C. J. "Richardson Extrapolation-Based Discretization Uncertainty Estimation for Computational Fluid Dynamics", *Journal of Fluids Engineering*, v. 136, n. 121401, 2014. doi: 10.1115/1.4027353.121401.

[63] FERZIGER, J. H., PERIC, M. *Computational Methods for Fluid Dynamics*. Berlin, Heidelberg, New York, Barcelona, Hong Kong, London, Milan, Paris, Tokyo, Springer, 2002. ISBN: 3-540-42074-6.

[64] GREENSHIELDS, C. *OpenFOAM v7 User Guide*. London, UK, The OpenFOAM Foundation, 2019. Disponível em: <`https://doc.cfd.direct/openfoam/user-guide-v7`>.

[65] GOLUB, G. H., VAN LOAN, C. F. *Matrix Computation*. Baltimore, Maryland, USA, The Johns Hopkins University Press, 2013. ISBN: 978-1-4214-0794-4.

Appendix A

Development of the Analytical Solutions

A.1 Couette Rheometer

Consider again the flow described in Section 3.2.1: the incompressible two-dimensional Stokes flow of a homogeneous power-law fluid on a horizontal cylindrical Couette cell. Figure 3.2 is repeated here for clarity. The inner cylinder of radius R_i rotates at an angular velocity ω, while the outer cylinder of radius R_o is stationary. The total length L of the cylinder is considered to be sufficient to neglect end effects.

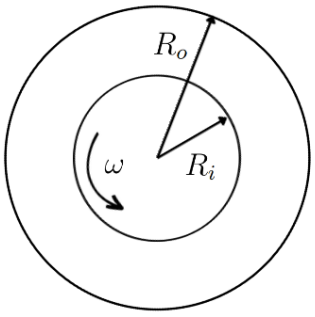

Figure 3.2: Couette rheometer geometry used to obtain the analytical solution for a power-law fluid.

If the effects of gravity are neglected, the flow is symmetric with respect to the angular coordinate, i.e., no field variable depends on θ and the velocity $\mathbf{u}$ can be written as:

$$\mathbf{u} = u_\theta(r)\hat{\mathbf{e}}_\theta. \tag{A.1}$$

From the definition of a power-law fluid [54]:

$$\boldsymbol{\tau} = 2m\dot{\gamma}^{n-1}\mathbf{E} \tag{A.2}$$

where m and n are the two coefficients of the model to be determined from the simulations. If $n = 1$, Equation A.2 reduces to the Newtonian model and $m = \mu$.

To determine the strain rate tensor $\mathbf{E}$, first we need to find the expression for $\nabla\mathbf{u}$:

$$\nabla\mathbf{u} = \frac{du_\theta}{dr}\hat{\mathbf{e}}_r\hat{\mathbf{e}}_\theta - \frac{u_\theta}{r}\hat{\mathbf{e}}_\theta\hat{\mathbf{e}}_r. \tag{A.3}$$

Then:

$$\begin{aligned}\mathbf{E} &= \frac{1}{2}\left[(\nabla\mathbf{u}) + (\nabla\mathbf{u})^T\right] \\ &= \frac{1}{2}\left[\left(\frac{du_\theta}{dr}\hat{\mathbf{e}}_r\hat{\mathbf{e}}_\theta - \frac{u_\theta}{r}\hat{\mathbf{e}}_\theta\hat{\mathbf{e}}_r\right) + \left(\frac{du_\theta}{dr}\hat{\mathbf{e}}_\theta\hat{\mathbf{e}}_r - \frac{u_\theta}{r}\hat{\mathbf{e}}_r\hat{\mathbf{e}}_\theta\right)\right] \\ &= \frac{1}{2}\left[\left(\frac{du_\theta}{dr} - \frac{u_\theta}{r}\right)\hat{\mathbf{e}}_r\hat{\mathbf{e}}_\theta + \left(\frac{du_\theta}{dr} - \frac{u_\theta}{r}\right)\hat{\mathbf{e}}_\theta\hat{\mathbf{e}}_r\right].\end{aligned} \tag{A.4}$$

Recognizing on the expression above that $E_{r\theta} = E_{\theta r}$, we can simplify the expression for the strain rate tensor:

$$\mathbf{E} = E_{r\theta}\hat{\mathbf{e}}_r\hat{\mathbf{e}}_\theta + E_{r\theta}\hat{\mathbf{e}}_\theta\hat{\mathbf{e}}_r \tag{A.5}$$

where

$$E_{r\theta} = \frac{1}{2}r\frac{d}{dr}\left(\frac{u_\theta}{r}\right). \tag{A.6}$$

The shear rate is given by:

$$\begin{aligned}\dot{\gamma} &= \sqrt{2\mathbf{E} : \mathbf{E}} \\ &= \sqrt{2\left(E_{\theta r}E_{r\theta} + E_{r\theta}E_{\theta r}\right)} \\ &= \sqrt{4E_{r\theta}^2} \\ &= 2\left|E_{r_\theta}\right|.\end{aligned} \tag{A.7}$$

Knowing that $du_\theta/dr < 0$, we can write:

$$\dot{\gamma} = -2E_{r_\theta}. \tag{A.8}$$

Replacing the expressions for the strain rate tensor and for the shear rate in Equation A.2 yields:

$$\begin{aligned}\boldsymbol{\tau} &= 2m\left(-2E_{r\theta}\right)^{n-1}\left[E_{r\theta}\hat{\mathbf{e}}_r\hat{\mathbf{e}}_\theta + E_{r\theta}\hat{\mathbf{e}}_\theta\hat{\mathbf{e}}_r\right] \\ &= m\left[-r\frac{d}{dr}\left(\frac{u_\theta}{r}\right)\right]^{n-1} \times \left[r\frac{d}{dr}\left(\frac{u_\theta}{r}\right)\hat{\mathbf{e}}_r\hat{\mathbf{e}}_\theta + r\frac{d}{dr}\left(\frac{u_\theta}{r}\right)\hat{\mathbf{e}}_\theta\hat{\mathbf{e}}_r\right].\end{aligned} \tag{A.9}$$

Then:

$$\boldsymbol{\tau} = \tau_{r\theta}\hat{\mathbf{e}}_r\hat{\mathbf{e}}_\theta + \tau_{\theta r}\hat{\mathbf{e}}_\theta\hat{\mathbf{e}}_r \tag{A.10}$$

where

$$\tau_{r\theta} = \tau_{\theta r} = -m\left[-r\frac{d}{dr}\left(\frac{u_\theta}{r}\right)\right]^n. \tag{A.11}$$

The radial component of the momentum equation for the steady-state flow is:

$$-\rho\frac{[u_\theta(r)]^2}{r} = -\frac{dp}{dr}. \tag{A.12}$$

Thus:

$$p(r) = \rho\int_{R_i}^{R_o}\frac{[u_\theta(r)]^2}{r}dr. \tag{A.13}$$

Once the velocity field is known, the integral in the latest equation can be solved to find an expression for the pressure field.

The angular component of the momentum equation for the steady-state flow simplifies to:

$$\begin{aligned} 0 =& \frac{1}{r^2}\frac{d}{dr}\left(r^2\tau_{r\theta}\right) \\ =& \frac{d\tau_{r\theta}}{dr} + \frac{2\tau_{r\theta}}{r}. \end{aligned} \tag{A.14}$$

Replacing the expression found for $\tau_{r\theta}$, Equation A.14 can be written as:

$$0 = r\frac{d}{dr}\left[-r\frac{d}{dr}\left(\frac{u_\theta}{r}\right)\right]^n + 2\left[-r\frac{d}{dr}\left(\frac{u_\theta}{r}\right).\right]^n \tag{A.15}$$

Applying the following change of variable to solve the differential equation:

$$\Gamma = -r\frac{d}{dr}\left(\frac{u_\theta}{r}\right). \tag{A.16}$$

Thus, Equation A.15 in terms of Γ reads:

$$\begin{aligned} 0 =& r\frac{d}{dr}\left(\Gamma^n\right) + 2\Gamma^n \\ =& rn\Gamma^{n-1}\frac{d\Gamma}{dr} + 2\Gamma^n \end{aligned} \tag{A.17}$$

or, as $\Gamma \neq 0$:

$$0 = \frac{rn}{\Gamma}\frac{d\Gamma}{dr} + 2. \tag{A.18}$$

Separating and integrating the latest expression leads to the solution of the differential equation for Γ:

$$\Gamma(r) = Br^{-2/n}. \tag{A.19}$$

The solution for $u_\theta(r)$ is found from the solution of Γ:

$$Br^{-2/n} = -r\frac{d}{dr}\left(\frac{u_\theta}{r}\right) \tag{A.20}$$

$$u_\theta(r) = Cr + \frac{B}{2}nr^{1-2/n} \tag{A.21}$$

where B and C are the integration constants.

For a stationary outer cylinder, the no-slip condition is applied at $r = R_o$,

$$u_\theta|_{r=R_o} = 0 = CR_o + \frac{B}{2}nR_o^{1-2/n} \tag{A.22}$$

providing the expression for constant C:

$$C = -\frac{Bn}{2}R_o^{-2/n}. \tag{A.23}$$

Substituting C into the solution of $u_\theta(r)$:

$$u_\theta(r) = \frac{Bn}{2}\left[r^{1-2/n} - rR_o^{-2/n}\right]. \tag{A.24}$$

If the inner cylinder is rotating with angular velocity ω, the second boundary condition, at $r = R_i$, yields:

$$u_\theta|_{r=R_i} = \omega R_i = \frac{Bn}{2}\left[R_i^{1-2/n} - R_iR_o^{-2/n}\right]. \tag{A.25}$$

Hence, the following expression is found for constant B:

$$B = -\frac{2\omega}{n}\left[R_o^{-2/n} - R_i^{-2/n}\right]^{-1} \tag{A.26}$$

and the final expression for the velocity is:

$$u_\theta(r) = \omega r\,\frac{1-(r/R_o)^{-2/n}}{1-\left(\frac{R_i}{R_o}\right)^{-2/n}}. \tag{A.27}$$

The torque over a given surface is given by:

$$\mathbf{T} = \int_S \mathbf{r}\times(\hat{\mathbf{n}}\cdot\mathbf{S})\,dA. \tag{A.28}$$

where $\hat{\mathbf{n}}$ is the surface's unit normal vector and $\mathbf{r}$ is the position vector relative to the center of rotation. At the inner cylinder, the normal unit vector is $\hat{\mathbf{n}} = \hat{\mathbf{e}}_r$. The position vector, with the center of rotation at the origin of the cylindrical coordinate

system, and the differential surface area with constant radius are, respectively:

$$\mathbf{r} = r\hat{\mathbf{e}}_r + \hat{\mathbf{e}}_z \tag{A.29}$$

$$dA = 2\pi r dz d\theta. \tag{A.30}$$

The stress tensor $\mathbf{S}$ is defined by:

$$\mathbf{S} = -p\mathbf{I} + \boldsymbol{\tau}. \tag{A.31}$$

Therefore, the argument inside the integral in Equation A.28 is:

$$\begin{aligned} \mathbf{r} \times (\hat{\mathbf{n}} \cdot \mathbf{S}) &= (r\hat{\mathbf{e}}_r + \hat{\mathbf{e}}_z) \times [\hat{\mathbf{e}}_r \cdot (-p\mathbf{I} + \boldsymbol{\tau})] \\ &= (r\hat{\mathbf{e}}_r + \hat{\mathbf{e}}_z) \times (-p\hat{\mathbf{e}}_r + \tau_{r\theta}\hat{\mathbf{e}}_\theta) \\ &= r\tau_{r\theta}\hat{\mathbf{e}}_z - pz\hat{\mathbf{e}}_\theta - z\tau_{r\theta}\hat{\mathbf{e}}_r. \end{aligned} \tag{A.32}$$

Integrating the expression for the torque at the inner cylinder:

$$\begin{aligned} \mathbf{T} &= \int_{-L/2}^{L/2} 2\pi R_i \left(R_i \, \tau_{r\theta}|_{r=R_i} - pz\hat{\mathbf{e}}_\theta - z \, \tau_{r\theta}|_{r=R_i} \hat{\mathbf{e}}_r \right) dz \\ &= 2\pi R_i \left[R_i z \, \tau_{r\theta}|_{r=R_i} \hat{\mathbf{e}}_z - \frac{pz^2}{2}\hat{\mathbf{e}}_\theta - \frac{\tau_{r\theta}|_{r=R_i} z^2}{2}\hat{\mathbf{e}}_r \right]_{z=-L/2}^{z=L/2}. \end{aligned} \tag{A.33}$$

The last two terms on the right-hand side of the equation evaluated at $z = -L/2$ and $z = L/2$ cancel out. Then, the resulting expression for the torque is:

$$\mathbf{T} = 2\pi R_i^2 L \, \tau_{r\theta}|_{r=R_i} \hat{\mathbf{e}}_z. \tag{A.34}$$

Substituting the expression found for Γ (Equation A.20) into the expression for $\tau_{r\theta}$ (Equation A.11):

$$\begin{aligned} \tau_{r\theta}|_{r=R_i} &= -m \, (\Gamma)^n \\ &= -m \left(B R_i^{-2/n} \right)^n \\ &= -\frac{m}{R_i^2} \left[\frac{2\omega}{n} \left(R_i^{-2/n} - R_o^{-2/n} \right)^{-1} \right]^n. \end{aligned} \tag{A.35}$$

Then, the z-component of the torque at the inner cylinder is:

$$\left. \frac{T_z}{L} \right|_{r=R_i} = -2\pi m \left(\frac{2\omega}{n} \right)^n \left(R_o^{-2/n} - R_i^{-2/n} \right)^{-n}. \tag{A.36}$$

A.2 Channel Flow

For the channel flow, Figure 3.3 and the flow conditions are also repeated for clarity: consider the incompressible two-dimensional Stokes flow at the steady state of the same homogeneous power-law fluid as described before, flowing in a channel with half-width H, as represented in Figure 3.3. Fluid enters the channel with a mean velocity $\overline{u}$ and, neglecting the effects of gravity, the developed flow will be symmetric with respect to the center line at $y = 0$. The goal of this analysis is to determine an expression for the pressure drop ΔP between the x-normal surfaces of the control volume represented in Figure 3.3.

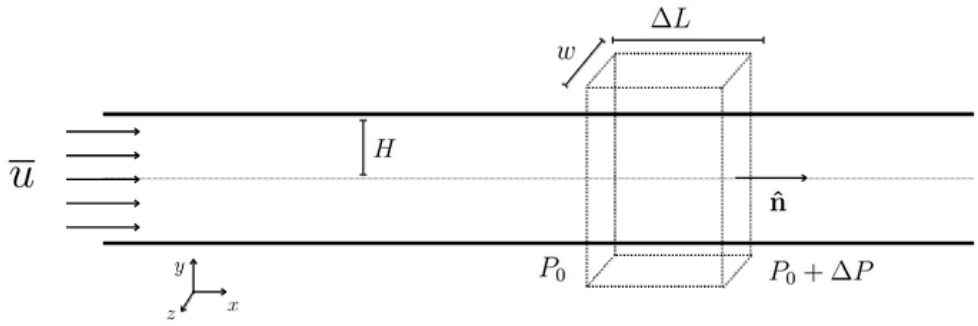

Figure 3.3: Straight 2-D channel geometry used to obtain the analytical solution for a power-law fluid.

For the fully-developed flow, velocity depends only on the y coordinate:

$$\mathbf{u} = u_x(y)\hat{\mathbf{e}}_x \tag{A.37}$$

and its gradient is:

$$\nabla\mathbf{u} = \frac{du_x}{dy}\hat{\mathbf{e}}_y\hat{\mathbf{e}}_x. \tag{A.38}$$

Thus, the rate of strain tensor is:

$$\mathbf{E} = \frac{1}{2}\left[\frac{du_x}{dy}\hat{\mathbf{e}}_y\hat{\mathbf{e}}_x + \frac{du_x}{dy}\hat{\mathbf{e}}_x\hat{\mathbf{e}}_y\right] \tag{A.39}$$

with components:

$$E_{xy} = E_{yx} = \frac{1}{2}\frac{du_x}{dy} \tag{A.40}$$

and the shear rate:

$$\begin{aligned}\dot{\gamma} &= \sqrt{2\left(E_{xy}E_{yx} + E_{yx}E_{xy}\right)} \\ &= \sqrt{4E_{xy}^2} \\ &= 2\left|E_{xy}\right|.\end{aligned} \tag{A.41}$$

Since $du_x/dy \leq 0$ for $y \in [0, H]$, the solution was developed for this half of the channel, where:

$$\dot{\gamma} = -2E_{xy}. \tag{A.42}$$

Tensor $\boldsymbol{\tau}$ is now given by:

$$\begin{aligned}
\boldsymbol{\tau} &= 2m\dot{\gamma}^{n-1}\mathbf{E} \\
&= 2m\left(-\frac{du_x}{dy}\right)^{n-1} \times \frac{1}{2}\left[\frac{du_x}{dy}\hat{\mathbf{e}}_y\hat{\mathbf{e}}_x + \frac{du_x}{dy}\hat{\mathbf{e}}_x\hat{\mathbf{e}}_y\right] \\
&= \tau_{xy}\hat{\mathbf{e}}_x\hat{\mathbf{e}}_y + \tau_{yx}\hat{\mathbf{e}}_y\hat{\mathbf{e}}_x
\end{aligned} \tag{A.43}$$

where:

$$\tau_{xy} = \tau_{yx} = -m\left(-\frac{du_x}{dy}\right)^n. \tag{A.44}$$

The momentum equation for the y direction is:

$$0 = \frac{\partial p}{\partial y} - \frac{\partial \tau_{xy}}{\partial x}. \tag{A.45}$$

Since τ_{xy} depends only on y, the second term on the expression above is zero. Then, pressure is constant with respect to y.

The momentum equation for the x direction is:

$$0 = \frac{dp}{dx} - \frac{d\tau_{yx}}{dy}. \tag{A.46}$$

Integrating the latest equation over an element volume $dV = dxdydz$ at a generic position y yields:

$$\begin{aligned}
0 &= \int_0^w \int_0^{\Delta L} \int_0^y \frac{dp}{dx} dydxdz - \int_0^w \int_0^{\Delta L} \int_0^y \frac{d\tau_{yx}}{dy} dydxdz \\
&= \int_0^{\Delta L} \frac{dp}{dx} ywdx - \int_0^y \frac{d\tau_{yx}}{dy} \Delta L w dy \\
&= yw\Delta P - w\Delta L\left[\tau_{yx}|_y - \tau_{yx}|_{y=0}\right].
\end{aligned} \tag{A.47}$$

With $du_x/dy = 0$ at the center line, the above expression reduces to:

$$\tau_{yx} = \left(\frac{\Delta P}{\Delta L}\right) y. \tag{A.48}$$

Substituting Equation A.48 into Equation A.44, an expression for the velocity is obtained:

$$\left(\frac{\Delta P}{\Delta L}\right) y = -m\left(-\frac{du_x}{dy}\right)^n. \tag{A.49}$$

Separation and integration of the differential equation lead to:

$$\left[\frac{1}{m}\left(-\frac{\Delta P}{\Delta L}\right)\right]^{1/n}\int y^{1/n}dy = -\int du_x \tag{A.50}$$

$$u_x(y) = B - \frac{ny^{1+1/n}}{n+1}\left[\frac{1}{m}\left(-\frac{\Delta P}{\Delta L}\right)\right]^{1/n}. \tag{A.51}$$

Applying the no-slip condition at the upper wall of the channel:

$$u_x|_{y=H} = 0 = B - \frac{nH^{1+1/n}}{n+1}\left[\frac{1}{m}\left(-\frac{\Delta P}{\Delta L}\right)\right]^{1/n} \tag{A.52}$$

gives:

$$B = \frac{nH^{1+1/n}}{n+1}\left[\frac{1}{m}\left(-\frac{\Delta P}{\Delta L}\right)\right]^{1/n}. \tag{A.53}$$

Then, the final expression for the velocity is:

$$u_x(y) = \frac{n}{n+1}\left[\frac{1}{m}\left(-\frac{\Delta P}{\Delta L}\right)\right]^{1/n}\left[H^{1+1/n} - y^{1+1/n}\right]. \tag{A.54}$$

A relation between the pressure drop and the mean velocity of the flow ($\overline{u}$) can be found by, first, calculating the volumetric flow rate through an arbitrary section of the channel normal to the flow direction:

$$Q = \int_A (\hat{\mathbf{n}}\cdot\mathbf{u})\, dA. \tag{A.55}$$

The normal unit vector is $\hat{\mathbf{n}} = \hat{\mathbf{e}}_x$ and the differential surface area element is $dA = wdy$. Then, considering that the flow is symmetric with respect to the center line at $y = 0$, the volumetric flow rate is:

$$\begin{aligned} Q &= \int_{-H}^{H} u_x w dy \\ &= 2w\int_0^H \frac{n}{n+1}\left[\frac{1}{m}\left(-\frac{\Delta P}{\Delta L}\right)\right]^{1/n}\left[H^{1+1/n} - y^{1+1/n}\right]dy \\ &= \frac{2wn}{2n+1}\left[\frac{1}{m}\left(-\frac{\Delta P}{\Delta L}\right)\right]^{1/n} H^{2+1/n}. \end{aligned} \tag{A.56}$$

Finally, in terms of the mean velocity:

$$\overline{u} = \frac{Q}{2Hw} = \frac{n}{2n+1}\left[\frac{1}{m}\left(-\frac{\Delta P}{\Delta L}\right)\right]^{1/n} H^{1+1/n}. \tag{A.57}$$

Appendix B

Dimensional Analysis of the Suspension Flow in a Couette Cell

In order to perform the dimensional analysis, the following length and velocity scales were considered:

$$l = R_o - R_i \ , \qquad v = 2\pi\omega R_i. \tag{B.1}$$

Then, the following dimensionless variables are defined:

$$\tau = \frac{v}{l}t \ , \qquad \check{p} = \frac{pl}{\mu_f v} \ , \qquad \check{\mathbf{u}} = \frac{\mathbf{u}}{v} \tag{B.2}$$

$$\check{r} = \frac{r}{l} \ , \qquad \check{\theta} = \theta \ , \qquad \check{z} = \frac{z}{l}. \tag{B.3}$$

B.1 Suspension Balance Model

Starting from the suspension's continuity equation (Equation 3.30), we have:

$$\begin{aligned} 0 &= \nabla \cdot \mathbf{u}_s \\ &= \frac{1}{l}\check{\nabla} \cdot (v\check{\mathbf{u}}_s) \\ &= \check{\nabla} \cdot \check{\mathbf{u}}_s \end{aligned} \tag{B.4}$$

and for the suspension's momentum equation (Equation 3.34):

$$0 = \nabla \cdot (-p\mathbf{I} + 2\mu_s \mathbf{E}_s - \mu_n \dot{\gamma}\mathbf{Q}) \, . \tag{B.5}$$

Writing the rate of strain tensor in terms of the dimensionless variables, for

$i = s, f, p$:

$$\begin{aligned}\mathbf{E}_i &= \frac{1}{2}\left[(\nabla \mathbf{u}_i) + (\nabla \mathbf{u}_i)^T\right] \\ &= \frac{1}{2}\left[\frac{v}{l}\left(\check{\nabla}\check{\mathbf{u}}_i\right) + \frac{v}{l}\left(\check{\nabla}\check{\mathbf{u}}_i\right)^T\right] \\ &= \frac{v}{l}\check{\mathbf{E}}_i\end{aligned} \tag{B.6}$$

and the shear rate is:

$$\begin{aligned}\dot{\gamma} &= 2\sqrt{\mathbf{E}_s : \mathbf{E}_s} \\ &= 2\sqrt{\left(\frac{v}{l}\right)^2\left(\check{\mathbf{E}}_s : \check{\mathbf{E}}_s\right)} \\ &= \frac{v}{l}\check{\gamma}.\end{aligned} \tag{B.7}$$

Substituting the expressions for the rate of strain tensor and shear rate from Equations B.6 and B.7, respectively, into Equation B.5:

$$\begin{aligned}0 &= \frac{1}{l}\check{\nabla}\cdot\left(-\frac{v}{l}\mu_f\check{p}\mathbf{I} + 2\mu_s\frac{v}{l}\check{\mathbf{E}}_s - \mu_n\frac{v}{l}\check{\gamma}\mathbf{Q}\right) \\ &= \check{\nabla}\cdot\left(-\mu_f\check{p}\mathbf{I} + 2\mu_s\check{\mathbf{E}}_s - \mu_n\check{\gamma}\mathbf{Q}\right).\end{aligned} \tag{B.8}$$

Dividing both sides of the last equation by the fluid's viscosity and defining a relative viscosity $\eta \equiv \mu/\mu_f$, we have the final form of the suspension's dimensionless momentum equation:

$$0 = \check{\nabla}\cdot\left(-\check{p}\mathbf{I} + 2\eta_s\check{\mathbf{E}}_s - \eta_n\check{\gamma}\mathbf{Q}\right). \tag{B.9}$$

Before carrying on to the analysis of the particle-phase continuity equation, Equation 3.15 is written as:

$$\frac{\partial\phi}{\partial t} + \mathbf{u}_s\cdot(\nabla\phi) = -\nabla\cdot[M\nabla\cdot\mathbf{S}_p] \tag{B.10}$$

with $M = 2a^2 f(\phi)/9\mu_f$. For its left-hand side, we have:

$$\begin{aligned}\frac{\partial\phi}{\partial t} + \mathbf{u}_s\cdot(\nabla\phi) &= \frac{v}{l}\frac{\partial\phi}{\partial\tau} + v\check{\mathbf{u}}_s\cdot\left(\frac{1}{l}\check{\nabla}\phi\right) \\ &= \frac{v}{l}\left[\frac{\partial\phi}{\partial\tau} + \check{\mathbf{u}}_s\cdot\left(\check{\nabla}\phi\right)\right].\end{aligned} \tag{B.11}$$

Using relations B.6 and B.7 on the right-hand side of Equation B.10, with the

definition of the particle-phase stress tensor given by Equation 3.18:

$$\begin{aligned}\nabla \cdot [M\nabla \cdot \mathbf{S}_p] &= \frac{1}{l}\check{\nabla} \cdot \left\{ \frac{M}{l}\check{\nabla} \cdot \left[\frac{v}{l} \left(2\mu_p \check{\mathbf{E}}_s - \mu_n \check{\gamma}\mathbf{Q} \right) \right] \right\} \\ &= \frac{v}{l^3}\check{\nabla} \cdot \left[M\check{\nabla} \cdot \left(2\mu_p \check{\mathbf{E}}_s - \mu_n \check{\gamma}\mathbf{Q} \right) \right].\end{aligned} \tag{B.12}$$

Then, replacing the expressions for both left and right-hand sides into Equation B.10 gives:

$$\frac{v}{l}\left[\frac{\partial \phi}{\partial \tau} + \check{\mathbf{u}}_s \cdot \left(\check{\nabla}\phi \right) \right] = -\frac{v}{l^3}\check{\nabla} \cdot \left[M\check{\nabla} \cdot \left(2\mu_p \check{\mathbf{E}}_s - \mu_n \check{\gamma}\mathbf{Q} \right) \right] \tag{B.13}$$

$$\frac{\partial \phi}{\partial \tau} + \check{\mathbf{u}}_s \cdot \left(\check{\nabla}\phi \right) = -\frac{1}{l^2}\check{\nabla} \cdot \left[\frac{2a^2 f(\phi)}{9\mu_f}\check{\nabla} \cdot \left(2\mu_p \check{\mathbf{E}}_s - \mu_n \check{\gamma}\mathbf{Q} \right) \right] \tag{B.14}$$

and the final form of the dimensionless particle-phase continuity is:

$$\frac{\partial \phi}{\partial \tau} + \check{\mathbf{u}}_s \cdot \left(\check{\nabla}\phi \right) = -\frac{2}{9}\left(\frac{a}{l} \right)^2 \check{\nabla} \cdot \left[f(\phi)\check{\nabla} \cdot \check{\mathbf{S}}_p \right] \tag{B.15}$$

where

$$\check{\mathbf{S}}_p = 2\eta_p \check{\mathbf{E}}_s - \eta_n \check{\gamma}\mathbf{Q}. \tag{B.16}$$

There are two dimensionless groups in Equation B.15 that affect the dynamics of this equation: τ and a/l. Since the ratio a/l is fixed for the simulated conditions described in Section 4.3.1, the dynamic behavior of the dispersed-phase fraction is dictated by τ. At the steady state, we have:

$$\check{\mathbf{u}}_s \cdot \left(\check{\nabla}\phi \right) = -\frac{2}{9}\frac{a^2}{l^2}\check{\nabla} \cdot \left[f(\phi)\check{\nabla} \cdot \check{\mathbf{S}}_p \right]. \tag{B.17}$$

But $\check{\mathbf{u}}_s$ and $\check{\nabla}\phi$ are orthogonal, leading to:

$$0 = \check{\nabla} \cdot \check{\mathbf{S}}_p. \tag{B.18}$$

Therefore, the steady-state solid-phase fraction profile is completely independent of the cylinder rotation velocity ω.

If we compare two scenarios with the same suspension being sheared in the same rheometer, but with different rotation velocities of the inner cylinder, both sharing the same steady-state profile of ϕ at the same instant τ, we have:

$$\tau_1 = \tau_2 \quad \longrightarrow \quad \left(\frac{v}{l}t \right)_1 = \left(\frac{v}{l}t \right)_2 \quad \longrightarrow \quad \frac{2\pi\omega_1 R_i}{l}t_1 = \frac{2\pi\omega_2 R_i}{l}t_2 \tag{B.19}$$

$$\omega_1 t_1 = \omega_2 t_2 \tag{B.20}$$

which means that the same solid-phase fraction profile is achieved after the same

number of revolutions of the inner cylinder, regardless of its rotational speed.

Finally, applying the dimensional analysis to the boundary conditions for the suspension velocity:

$$\mathbf{u}_s|_{r=R_i} = 2\pi\omega R_i \qquad \longrightarrow \qquad \check{\mathbf{u}}_s|_{\check{r}=0} = \frac{2\pi\omega R_i}{v} = 1 \tag{B.21}$$

$$\mathbf{u}_s|_{r=R_o} = 0 \qquad \longrightarrow \qquad \check{\mathbf{u}}_s|_{\check{r}=1} = 0. \tag{B.22}$$

Also, for the zero normal gradient boundary condition for the solid-phase fraction:

$$\frac{\partial\phi}{\partial r} = 0 \qquad \longrightarrow \qquad \frac{\partial\phi}{\partial\check{r}} = 0 \tag{B.23}$$

and for the pressure:

$$\frac{\partial p}{\partial r} = 0 \qquad \longrightarrow \qquad \frac{\partial\check{p}}{\partial\check{r}} = 0 \tag{B.24}$$

No dependence on any parameter of the flow, either geometrical or experimental, appears in the boundary conditions.

B.2 Two-Fluid Model

To start the analysis of the two-fluid model, the continuity equations for both phases (Equations 3.5 and 3.41) are written as:

$$\frac{\partial}{\partial t}\left(\rho_i\phi_i\right) + \nabla\cdot\left(\rho_i\phi_i\mathbf{u}_i\right) = 0, \qquad i = p, f \tag{B.25}$$

where $\phi_p \equiv \phi$ and $\phi_f = 1 - \phi$. If both phases are incompressible:

$$\begin{aligned} 0 &= \frac{\partial\phi_i}{\partial t} + \nabla\cdot\left(\phi_i\mathbf{u}_i\right) \\ &= \frac{v}{l}\frac{\partial\phi_i}{\partial\tau} + \frac{v}{l}\check{\nabla}\cdot\left(\phi_i\check{\mathbf{u}}_i\right) \\ &= \frac{\partial\phi_i}{\partial\tau} + \check{\nabla}\cdot\left(\phi_i\check{\mathbf{u}}_i\right). \end{aligned} \tag{B.26}$$

Unlike what was seen for the SBM, there is no other dimensionless group besides τ that could affect the dynamics of the phase fraction equations. Thus, the dynamic behavior is only controlled by τ, and, again, the steady-state profile of the dispersed-phase fraction is independent of the rotation velocity of the inner cylinder.

Moving on to the momentum conservation equation for the particle phase (Equation 3.9) and disregarding the body forces, we have:

$$\frac{\partial\left(\rho_p\phi\mathbf{u}_p\right)}{\partial t} + \nabla\cdot\left(\rho_p\phi\mathbf{u}_p\mathbf{u}_p\right) = \nabla\cdot\mathbf{S}_p + \mathbf{f}_p. \tag{B.27}$$

For constant ρ_p, we can write the first term on the left-hand side as:

$$\begin{aligned}\frac{\partial}{\partial t}\left(\rho_p\phi\mathbf{u}_p\right) &= \frac{v}{l}\frac{\partial}{\partial\tau}\left(v\rho_p\phi\breve{\mathbf{u}}_p\right)\\ &= \frac{v^2\rho_p}{l}\frac{\partial}{\partial\tau}\left(\phi\breve{\mathbf{u}}_p\right)\end{aligned} \tag{B.28}$$

and the second term as:

$$\begin{aligned}\nabla\cdot\left(\rho_p\phi\mathbf{u}_p\mathbf{u}_p\right) &= \frac{1}{l}\breve{\nabla}\cdot\left[v^2\rho_p\phi\breve{\mathbf{u}}_p\breve{\mathbf{u}}_p\right]\\ &= \frac{v^2\rho_p}{l}\breve{\nabla}\cdot\left(\phi\breve{\mathbf{u}}_p\breve{\mathbf{u}}_p\right).\end{aligned} \tag{B.29}$$

Using expression 3.55 for the particle-phase stress tensor, the first term on the right-hand side is:

$$\nabla\cdot\mathbf{S}_p = \nabla\cdot\left[2\mu_p\mathbf{E}_p - \frac{2}{3}\mu_p\left(\nabla\cdot\mathbf{u}_p\right)\mathbf{I} - \mu_n\dot{\gamma}\mathbf{Q}\right] \tag{B.30}$$

and using relations B.6 and B.7, we can write:

$$\begin{aligned}\nabla\cdot\mathbf{S}_p &= \frac{1}{l}\breve{\nabla}\cdot\left[2\frac{v}{l}\mu_p\breve{\mathbf{E}}_p - \frac{2}{3}\mu_p\frac{v}{l}\left(\breve{\nabla}\cdot\breve{\mathbf{u}}_p\right)\mathbf{I} - \frac{v}{l}\mu_n\breve{\gamma}\mathbf{Q}\right]\\ &= \frac{v}{l^2}\breve{\nabla}\cdot\left[2\mu_p\breve{\mathbf{E}}_p - \frac{2}{3}\mu_p\left(\breve{\nabla}\cdot\breve{\mathbf{u}}_p\right)\mathbf{I} - \mu_n\breve{\gamma}\mathbf{Q}\right].\end{aligned} \tag{B.31}$$

Considering the drag force to be the only interaction force between phases, Equation 3.44 can be written as:

$$\begin{aligned}\mathbf{f}_p &= \frac{9\mu_f\phi}{2a^2 f(\phi)}\left(\mathbf{u}_p - \mathbf{u}_f\right)\\ &= \frac{9\mu_f\phi v}{2a^2\hat{f}(\phi)}\left(\breve{\mathbf{u}}_p - \breve{\mathbf{u}}_f\right)\end{aligned} \tag{B.32}$$

where $\hat{f}(\phi) = f(\phi)/(1-\phi)$ with $f(\phi)$ defined by Equation 3.12. Thus, Equation B.27 reads:

$$\begin{aligned}\frac{v^2\rho_p}{l}\left[\frac{\partial}{\partial\tau}\left(\phi\breve{\mathbf{u}}_p\right) + \breve{\nabla}\cdot\left(\phi\breve{\mathbf{u}}_p\breve{\mathbf{u}}_p\right)\right] =& \frac{v}{l^2}\breve{\nabla}\cdot\left[2\mu_p\breve{\mathbf{E}}_p - \frac{2}{3}\mu_p\left(\breve{\nabla}\cdot\breve{\mathbf{u}}_p\right)\mathbf{I} - \mu_n\breve{\gamma}\mathbf{Q}\right]\\ &+ \frac{9\mu_f\phi v}{2a^2\hat{f}(\phi)}\left(\breve{\mathbf{u}}_p - \breve{\mathbf{u}}_f\right).\end{aligned} \tag{B.33}$$

Multiplying both sides of the last equation by $l^2/\mu_f v$ and defining $Re^* = \rho_p v l/\mu_f$,

we have:

$$Re^*\left[\frac{\partial}{\partial\tau}\left(\phi\check{\mathbf{u}}_p\right)+\check{\nabla}\cdot\left(\phi\check{\mathbf{u}}_p\check{\mathbf{u}}_p\right)\right]=\frac{1}{\mu_f}\check{\nabla}\cdot\left[2\mu_p\check{\mathbf{E}}_p-\frac{2}{3}\mu_p\left(\check{\nabla}\cdot\check{\mathbf{u}}_p\right)\mathbf{I}-\mu_n\check{\gamma}\mathbf{Q}\right]+\frac{9\phi l^2}{2a^2\hat{f}(\phi)}\left(\check{\mathbf{u}}_p-\check{\mathbf{u}}_f\right). \tag{B.34}$$

Recalling the definition of $\eta\equiv\mu/\mu_f$, the last equation is further simplified to:

$$Re^*\left[\frac{\partial}{\partial\tau}\left(\phi\check{\mathbf{u}}_p\right)+\check{\nabla}\cdot\left(\phi\check{\mathbf{u}}_p\check{\mathbf{u}}_p\right)\right]=\check{\nabla}\cdot\left[2\eta_p\check{\mathbf{E}}_p-\frac{2}{3}\eta_p\left(\check{\nabla}\cdot\check{\mathbf{u}}_p\right)\mathbf{I}-\eta_n\check{\gamma}\mathbf{Q}\right]+\frac{9\phi l^2}{2a^2\hat{f}(\phi)}\left(\check{\mathbf{u}}_p-\check{\mathbf{u}}_f\right) \tag{B.35}$$

Finally, the dynamics of the particle momentum equation is seen to be proportional to τ/Re^*. Comparing it to the dynamics of the particle-phase continuity equation, which is proportional to τ:

$$\tau\ \times\ \frac{\tau}{Re^*}\qquad\longrightarrow\qquad\frac{vt}{l}\ \times\ \frac{\mu_f t}{\rho_p l^2} \tag{B.36}$$

Hence, if $v/l\gg\mu_f/\rho_s l^2$, the dynamics of the flow is controlled by the dispersed-phase continuity equation, being dependent on τ and, consequently, on ω. Otherwise, if $v/l\ll\mu_f/\rho_s l^2$, it is controlled by the momentum conservation equation, being proportional to τ/Re^* and independent from ω. When the dynamics is controlled by τ, the relation $\omega_1 t_1=\omega_2 t_2$ obtained from Equation B.19 for the SBM is also valid.

At the steady state:

$$Re^*\left[\check{\nabla}\cdot\left(\phi\check{\mathbf{u}}_p\check{\mathbf{u}}_p\right)\right]=\check{\nabla}\cdot\left[2\eta_p\check{\mathbf{E}}_p-\frac{2}{3}\eta_p\left(\check{\nabla}\cdot\check{\mathbf{u}}_p\right)\mathbf{I}-\mu_n\check{\gamma}\mathbf{Q}\right]+\frac{9\phi l^2}{2a^2\hat{f}(\phi)}\left(\check{\mathbf{u}}_p-\check{\mathbf{u}}_f\right). \tag{B.37}$$

The term inside the brackets on the left-hand side is:

$$\check{\nabla}\cdot\left(\phi\check{\mathbf{u}}_p\check{\mathbf{u}}_p\right)=\phi\check{\mathbf{u}}_p\cdot\check{\nabla}\check{\mathbf{u}}_p+\check{\mathbf{u}}_p\check{\nabla}\cdot\left(\phi\check{\mathbf{u}}_p\right). \tag{B.38}$$

Since $\check{\mathbf{u}}_p\cdot\check{\nabla}\check{\mathbf{u}}_p=0$ for the Couette flow and, from Equation B.26 at the steady state, $\check{\nabla}\cdot\left(\phi\check{\mathbf{u}}_p\right)=0$, the left-hand side of Equation B.37 vanishes. Thus, it reduces to:

$$0=\check{\nabla}\cdot\left[2\eta_p\check{\mathbf{E}}_p-\frac{2}{3}\eta_p\left(\check{\nabla}\cdot\check{\mathbf{u}}_p\right)\mathbf{I}-\mu_n\check{\gamma}\mathbf{Q}\right]+\frac{9\phi}{2\hat{f}(\phi)}\left(\frac{l}{a}\right)^2\left(\check{\mathbf{u}}_p-\check{\mathbf{u}}_f\right). \tag{B.39}$$

Consequently, the steady state depends only on the ratio a/l and ϕ. Since a/l is constant and the steady-state profile of ϕ is independent of ω, then, the steady-state for the dimensionless velocity $\check{\mathbf{u}}_p$ is also independent of ω.

The dimensional analysis of the continuity and momentum conservation equations for the fluid phase is analogous and leads to similar conclusions. The procedure used in the analysis of the SBM boundary conditions can be followed by replacing the suspension's velocity with the phases' velocities, leading to the same conclusion of independence from any other dimensionless parameter.